UNIVERSITY OF CALIFORNIA
RIVERSIDE

A Renewed Look at the Coseismic Surface Deformation and Fault Slip of the 1994 Northridge Earthquake Using Space Geodesy

A Thesis submitted in partial satisfaction
of the requirements for the degree of

Master of Science

in

Geological Sciences

by

Chad M. Severson

June 2012

Thesis Committee:
Dr. Gareth Funning, Chairperson
Dr. Katherine J. Kendrick
Dr. David D. Oglesby

The Thesis of Chad M. Severson is approved:

_____

_____

_____

Committee Chairperson

University of California, Riverside

ABSTRACT OF THESIS

A Renewed Look at the Coseismic Surface Deformation and Fault Slip of the 1994 Northridge Earthquake Using Space Geodesy

by

Chad M. Severson

Master of Science, Graduate Program in Geological Sciences
University of California, Riverside, June 2012
Dr. Gareth J. Funning, Chairperson

The January 17, 1994 M6.7 Northridge earthquake occurred in the densely populated suburbs northwest of Los Angeles, California, causing 33 deaths and ~$20 billion in damage. To quantify the influence, in terms of stress changes, of the Northridge event on surrounding faults, detailed knowledge of the location, orientation and amount of fault slip is important. Existing InSAR models of this earthquake typically were developed by fitting the pattern of displacements by trial and error, and were therefore somewhat subjective. In the 15 years since the original studies were published a number of new modeling tools and community data products have been developed that should enable us to produce more detailed, objective and robust results.

We measure the coseismic deformation of this earthquake using InSAR data from the ERS-1 and JERS-1 satellites, combined with GPS measurements (Hudnut et al., 1996) that together show uplift of ~42 cm. Using these data, we first employ a nonlinear inversion to determine the parameters of a best-fitting model using rectangular,

uniform slip dislocations. Our best-fitting fault solution contains two faults, a main fault with 2.3 m of slip and a secondary fault to the northwest with 0.8 m.

In detail, however, the deformation pattern of the Northridge event is more complex than can be described by rectangular dislocations. To investigate this, we solve for a detailed slip distribution for the event using a non-planar triangular element fault mesh modified from the SCEC Community Fault Model (Plesch et al., 2007). This model shows a main asperity on a protrusion on the fault surface, with peak slip of ~2.7 m. The protrusion is bounded at its western edge by a geometrical barrier, a steep down-dip parallel ramp in the fault. Secondary slip of ~0.6 m to the northwest of this feature is also present. These two slip patches together show that the geometry of the fault strongly influences the slip pattern of the event.

Table of Contents

List of figures

List of tables

Chapter 1 Introduction

Interferometric synthetic aperture radar (InSAR) provides a useful tool for mapping topography and/or measuring deformation of the Earth's surface. To determine the spatial distribution of values, an interferogram is created using 2 Synthetic aperture radar (SAR) images, generally separated in time and taken from approximately the same location. Specifically, if the earth's surface has deformed in the interval of time between the two image acquisitions, a map of this deformation may be generated. This allows the user to study almost any source of surface deformation including, but not limited to, volcanic movements, deformation caused by resource extraction or recharge, and the entirety of the earthquake cycle, in which deformation may be modeled and its source inferred at depth.

In this introduction a brief overview is given of the steps used in processing InSAR data, as well as the procedures used to calculate source models of various earthquakes. InSAR data from the October 23, 2011 Van earthquake in eastern Turkey is used for an example, which is measured with SAR images from the Environment Satellite (Envisat), as well as data from the COSMO Sky-Med satellite. The reader is referred to other InSAR review papers that provide greater insight into the details of InSAR processing (e.g. Massonnet and Feigl, 1998; Bürgmann et al., 2000; Rosen et al., 2000; Wright, 2002). Funning et al. (2005) explain the modeling process in greater depth.

1.1 Radar

Since InSAR uses radar imagery, it is important to first understand radio detection and ranging (radar). Radar involves measuring electromagnetic waves that are emitted from an antenna, backscattered from their interaction with an object, and returned to the antenna, where they are detected. The time delay of the wave from emission to return is measured and the distance, also called range, of an object can be calculated, as the speed of the electromagnetic waves is known (the speed of light).

Radar was initially used in the 1930s as a way of detecting aircraft. Since then, radar has developed numerous purposes that include, but are not limited to, military defense, weather forecasting, air-traffic control, and scientific research. Radar is effective because it is an active source, meaning the source, in this case the radar antenna, emits and receives its own energy. This is opposite of a passive source, which measures the reflected waves that have been emitted by another source. An example of a passive source is photography, which measures the reflected waves of the sun's light energy.

1.1.1 Satellite radar

Recently, radar antennas have been mounted to space-borne satellites, which are able to make continuous measurements in consistent repeating patterns. A side looking aperture radar (SLAR) antenna is placed on an orbiting satellite in a precisely determined orbit. The antenna measures in the range direction, which is perpendicular to the direction of travel (azimuth direction). The satellites are in a polar orbit, where the direction of travel is primarily in the north-south direction. In the ascending track, the satellite travels south to north, while in the descending track, the satellite moves north to south. These range measurements are at some incidence angle from the vertical, generally between 20° and 50°. Typically, the antenna looks to the right of the satellite's path, as with the European Remote Sensing Satellites (ERS-1 and ERS-2), the Japanese Earth Resources Satellite (JERS-1), and the Environmental Satellite (Enivsat), as looking directly below causes ambiguities as to which side of the antenna the reflected waves came from.

1.1.2 Synthetic aperture radar

In order for interferometry to be useable for scientific research, resolution on the order of ~20 m is needed. Resolution, L_g is dependent on the length of the antenna L_a, the wavelength of the emitted radiation, λ, and the slant range (R; i.e. the distance from the satellite to the target), and is shown by,

$$L_g \approx \frac{R\lambda}{L_a} \tag{1.1}$$

Resolution for the ERS and Envisat satellites with a wavelength of ~5.6 cm, slant range of ~850 km, and antenna length of 10 m is ~4.8 km, far greater than the desired resolution of ~20 m. To obtain this desired resolution an antenna of ~2.4 long km is required, which would be unfeasible to launch, as well as power, on a satellite. Due to this, Synthetic aperture radar (SAR) utilizes the motion of the satellite to simulate a longer antenna length (Figure 1.1). As the satellite travels, it records multiple radar echoes of a single target on the ground, which simulates an antenna length that is the distance the satellite travels while the target is within the radar beam.

1.2. SAR satellites

Data from the ERS-1, JERS-1 and Envisat satellites are used for this research. Table 1.1 and the descriptions below provide information on each of the satellites.

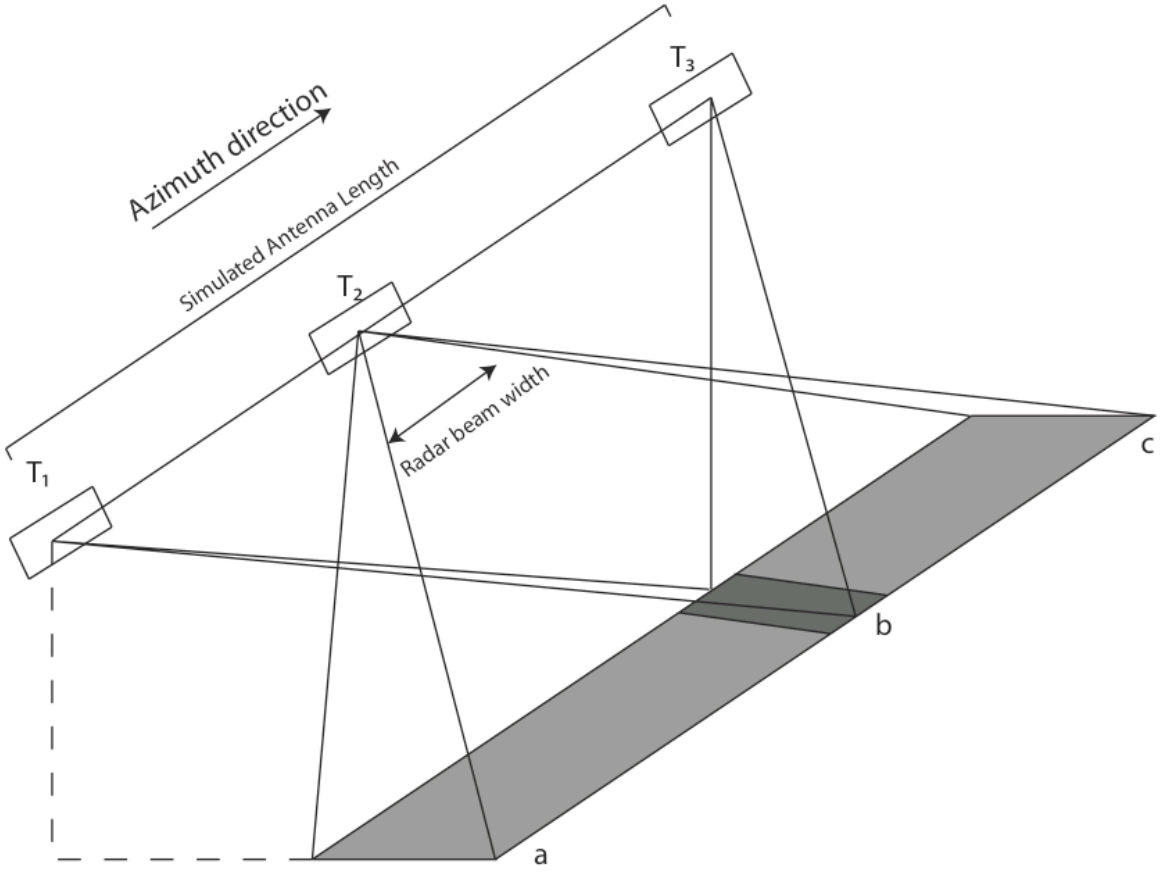

Figure 1.1. Illustration of synthetic aperture radar using multiple radar echoes of a single target (Dark region, point b). The target is illuminated from time T_1 through T_3 simulating an antenna length along the distance traveled between these times.

1.2.1 European Remote Sensing Satellite 1 (ERS-1)

The ERS-1 satellite was launched by the European Space Agency in July of 1991 in a 35-day repeat cycle, meaning it would repeat the same orbit and return to the same location every 35 days. Although it was not originally designed for interferometry, it acquired data until a gyroscope malfunction eliminated its effectiveness in March 2000. ERS-1 was put in a tandem mission with ERS-2, its sister satellite (1995-2011)

until the end of the ERS-1 mission in 2000. These two satellites flew the same path only 1 day apart and were used to map many remote regions of the Earth.

1.2.2 Japanese Earth Resources Satellite (JERS-1)

JERS-1 was launched by the Japanese Aerospace Exploration Agency in February 1992. The satellite was operational through October 1998 in a 44-day repeat cycle. JERS-1 housed a longer wavelength (23.5 cm) L-band radar, which allows for greater correlation between SAR image pairs than the shorter 5.6 cm C-band radar used by the ERS satellites. This longer wavelength is useful in areas that are heavily vegetated, as the electromagnetic waves penetrate farther, to the base of vegetation and are not reflected back by leaves and branches in the canopy, whose position vary randomly with wind and growth.

1.2.3 Envisat

The European Space Agency (ESA) put Envisat into orbit in March 2002 with a 35-day repeat cycle, as the successor to the ERS missions. Envisat contained 10 instruments including a C-band advanced synthetic aperture radar (ASAR) antenna, which provides greater capabilities in terms of coverage, range and incidence angles. Unfortunately, the ERS satellites and Envisat have slightly different wavelengths making interferometry impossible between the two satellites. Envisat

operated under normal conditions until late October 2010 when the satellite was placed into a new "drifting phase" orbit. It was in this phase that the 2011 Van earthquake was captured.

On April 12, 2012, ESA released a statement that as of April 8, it had lost contact with the Envisat satellite after multiple attempts to reconnect. Envisat was the last remaining public SAR satellite with an open data policy and had proved to be a useful scientific instrument in its longer-than-expected 10-year mission. The Cosmo-SkyMed constellation of SAR satellites, operated by the Italian Space Agency, and Radarsat from the Canadian Space Agency remain operational. These data, however, are not easily obtained for research use. ESA plans to launch the first of the Sentinel family of satellites in May 2013. These satellites will house C-band radar antennas and will take the place of Envisat. ESA sought to launch Sentinel before the decommissioning of Envisat. The recent failure of Envisat, however, has left a time gap in openly available SAR data.

	ERS-1	JERS-1	Envisat
Operating organization	ESA	JAXA	ESA
Wavelength	C-band, 5.66 cm	L-band, 23.53 cm	C-band, 5.62 cm
Launch date	July 1991	February 1992	March 2002
Mission end	March 2000	October 1998	April 2012
Incidence angle	23°	35°	Variable

Table 1.1. Information on the satellites used in this thesis.

1.3. The single look complex (SLC) image

The single look complex (SLC) image is a high-resolution image that contains information on both the amplitude and phase (Figure 1.2) of the radar echoes, stored as a grid of complex numbers. The amplitude is a measure of the backscatter intensity, where bright spots denote a strong signal return and darkness a weak signal return (Figure 1.3a). In this way, SAR images can measure the surface roughness of an area. Rough areas, such as mountains, buildings and rocky regions will backscatter radiation in all directions; most importantly, back to the satellite. Smooth areas such as lakes, calm rivers and roads, on the other hand, will reflect radiation away from the satellite, meaning the signal will not be recorded. (Figure 1.4).

The phase of the wave depends on a number of variables, most notably the distance between the ground pixel and the radar antenna. We typically do not consider the total phase of a wave that travels from the satellite to the ground and back again. Instead, we use differences in the measured phase between images to estimate changes in the distance between the satellite and the ground. The phase image (Figure 1.3b) appears as noise, having no systematic pattern, as the phase return is not consistent from pixel to pixel, which will be explained in more detail below.

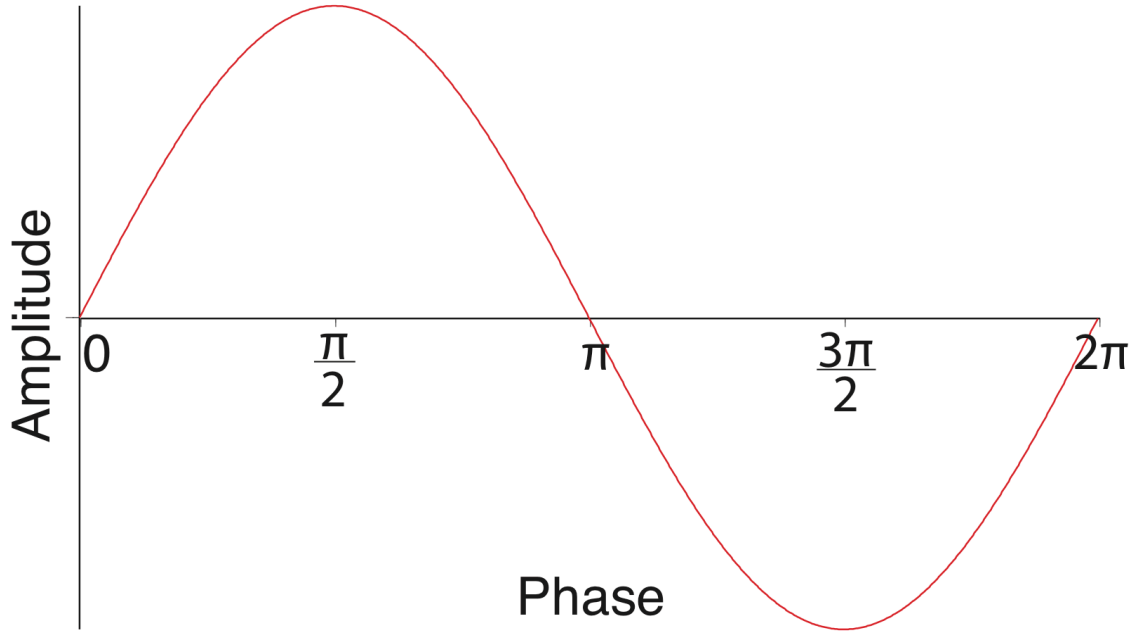

Figure 1.2. Illustration of a full phase cycle, which is equal to 2π

1.4. Interferometric synthetic aperture radar (InSAR)

An interferogram is a complex image that maps the phase difference between two or more repeating SAR images. For example, an interferogram of earthquake deformation would require one SAR image be acquired before the earthquake and a second one after the earthquake. As noted, the deformation due to the earthquake will cause a phase change between the images. One full phase cycle or 2π phase change between the images is equal to a 1 wavelength change between the two images in the two way path distance, as the radar waves travel from the satellite the ground and back to the satellite. Since we are only interested in the one-way travel

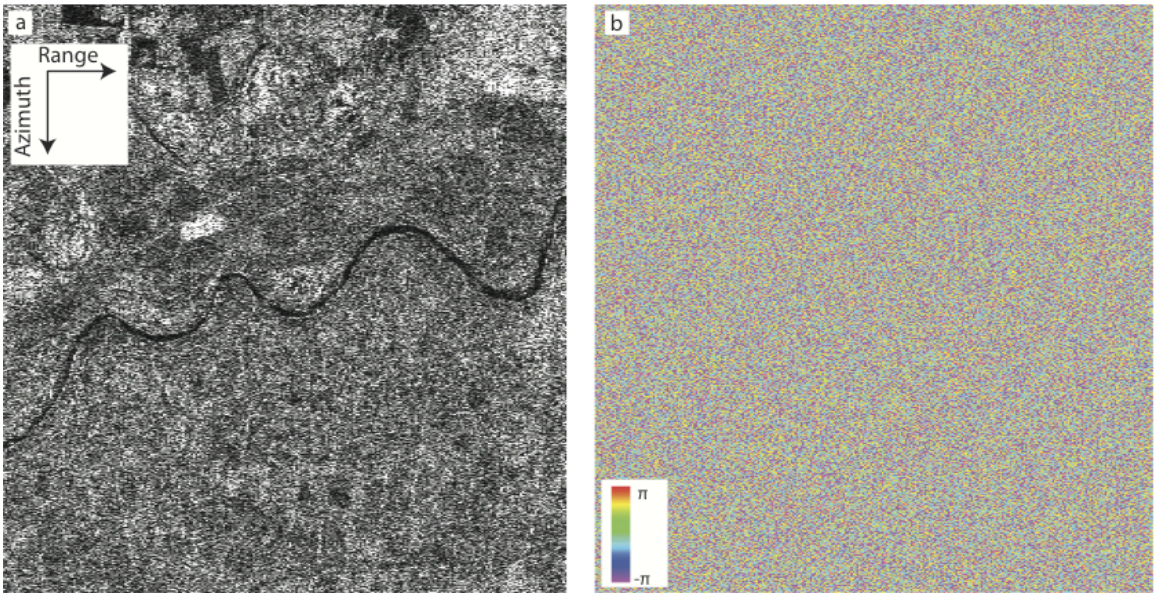

Figure 1.3. SLC image from Envisat track 121 of the Van region, Eastern Turkey. a) Amplitude image showing backscattered wave energy. White areas represent a stronger signal return to the satellite. This includes rocky areas and buildings. Dark areas represent low signal return. A calm, meandering river is shown by the black line across the middle of the photo. We can infer that this is a calm river as radiation is not reflected back to the satellite as would be with turbulent waters. b) Phase portion of the same image, which shows no systematic pattern to the pixels. It is effectively random.

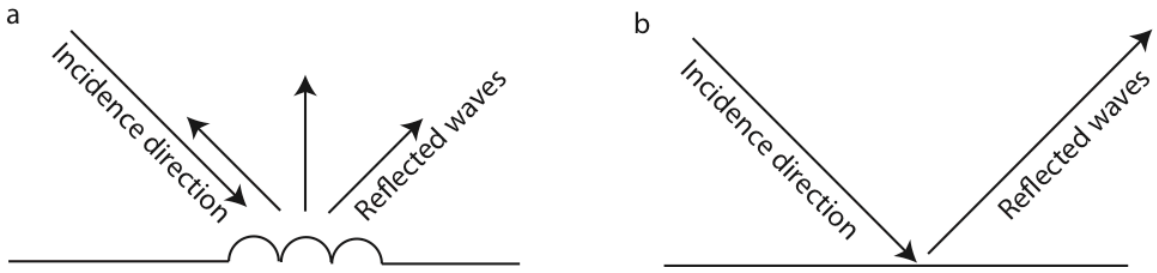

Figure 1.4. a) Electromagnetic radiation backscatters off rough areas, which give a greater signal return to the satellite. b) Smooth regions reflect radiation at the same angle as the incidence angle. Information is reflected away from the satellite and lost.

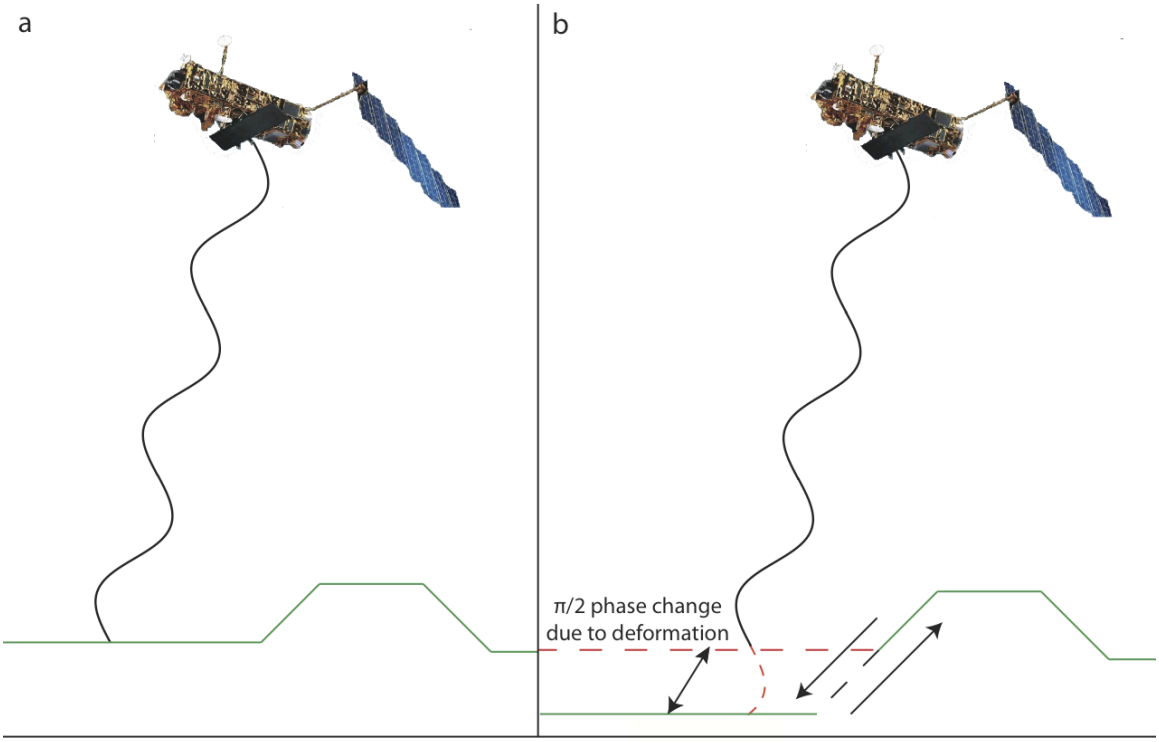

Figure 1.5. Illustration of phase change due to surface deformation. a) Satellite pass before the earthquake, b) a normal faulting earthquake creates surface subsidence. The range has increased by 1/8 wavelength, which means the distance has increased.

distance, or range change, each 2π phase change is equal to ½ the wavelength of the radar system in range change between the satellite and the ground. A 2π phase shift is typically represented in an interferogram as a full color cycle (red, yellow, green, violet), or 'fringe' (Figure 1.6), which can best be thought of as a deformation contour. As with a contour map, each contour represents a known elevation change; with InSAR, each successive fringe represents a known range change interval. For the C-band ERS and Envisat satellites, one fringe interval represents ~2.8 cm of range change, while one fringe for the longer wavelength L-band JERS-1 satellite represents ~11.8 cm of range change. These fringes may be summed, or

'unwrapped', in order to calculate the total displacement due to the event as shown in Figure 1.6.

1.4.1 Interferometric phase

As mentioned, the information in an interferogram reflects the difference in phase measured between two or more SAR images. The contributions to the change in phase, $\Delta\phi$, are

$$\Delta\phi = \Delta\phi_{path} + \Delta\phi_{atmosphere} + \Delta\phi_{pixel} \tag{1.2}$$

Where $\Delta\phi_{path}$ is the change in distance between the satellite antenna and the target, $\Delta\phi_{atmosphere}$ is the phase change due to atmospheric delay as the electromagnetic waves travel through water vapor in the troposphere, and $\Delta\phi_{pixel}$ is a phase delay resulting from the interaction of the radar waves with the contents of each pixel on the ground. Since the wavelength of the radar is much smaller than the pixel, the pixel phase initially contains hundreds of individual target scatters. The pixel contribution to the phase is the summation of radar backscatter from all of these individual targets. Due to this, the individual pixel reflections must be consistent between the two images. If the change in phase due to the pixel is not zero, it will cause a phase change that will mask the deformation signal. (see section 1.5.3).

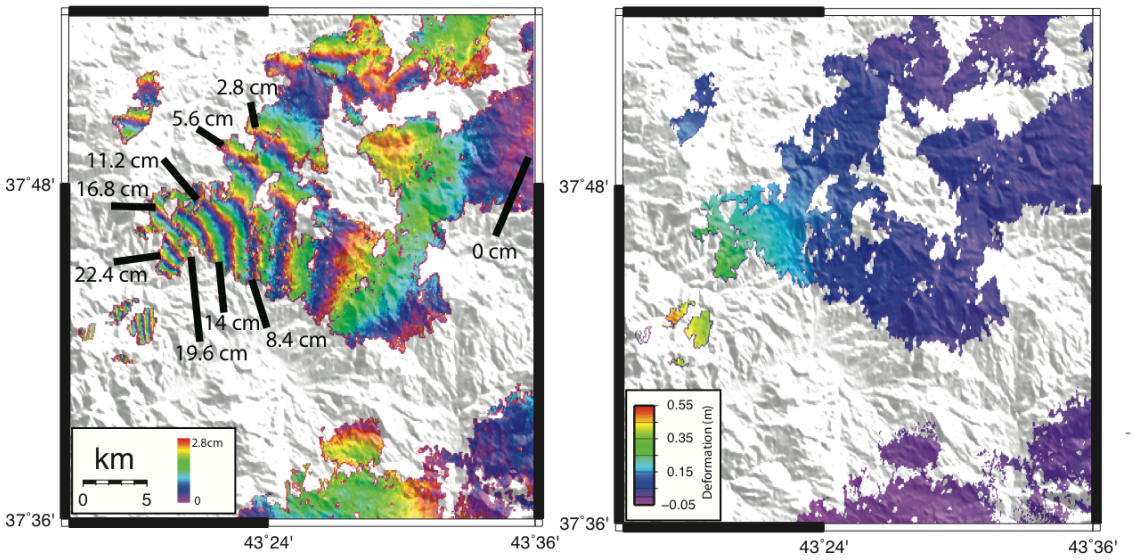

Figure 1.6. A small portion of the deformation pattern from the Van earthquake measured from Envisat track 121. a) 'Wrapped' interferogram. Each full fringe, or full color cycle, represents 2.8 cm of range decrease, or movement towards the satellite. These fringes are best thought of as deformation contours and may be summed to estimate total displacement as shown. b) 'unwrapped' or summed deformation. These two images represent the same deformation, however, (b) represents a continuous signal that is needed for modeling. White areas have been removed due to noise (see section 1.5.3). The interferogram spans the dates 11/05/2010-10/31/2011.

The difference in phase due to path length can be divided up into three contributing factors; the difference in viewing position, $\Delta\phi_{position}$, caused by the changes in the orbit of the satellite between the times of image acquisition, the effect of topography, $\Delta\phi_{topography}$, and the deformation of the surface, $\Delta\phi_{deformation}$. This results in

$$\Delta\phi_{path} = \Delta\phi_{position} + \Delta\phi_{topography} + \Delta\phi_{deformation} \tag{1.3}$$

When equations 4.1 and 4.2 are summed, the change in phase between the two

images is,

$$\Delta\phi = \Delta\phi_{position} + \Delta\phi_{topography} + \phi_{deformation} + \Delta\phi_{atmosphere} + \Delta\phi_{pixel} \quad (1.4)$$

Earthquake studies are primarily interested in the phase change due to deformation. Therefore, other phase contributions that can be corrected, such as position, and topography, are removed.

1.4.2 Phase contribution associated with positioning.

Satellite interferometry relies on two passes of the satellite in the same orbit. Repeating the exact pass is unlikely, so a correction is made to subtract for the phase contribution due to differences in orbital viewing geometry between the two images. The difference in position of the two image acquisition locations is known as the baseline separation, or simply, 'baseline' and can be broken down into two components; parallel baseline which is the separation between the satellite passes parallel to the range, or measuring direction, and perpendicular baseline which is perpendicular to the range direction. While repeating the same path is more likely for a satellite than other forms of SAR acquisition (i.e. SAR systems mounted on airplanes), the satellite's orbit may change due to solar radiation pressure and tidal forces. The satellite changes in orbit may be corrected by using onboard thrusters,

however, limitations in fuel determine how many corrections may be made. In terms of phase difference, the orbital separation of the SAR images is shown by,

$$\phi = \frac{4\pi B \sin(\gamma - \alpha)}{\lambda} \tag{1.5}$$

where B is the baseline separation, γ is the incidence angle of the satellite from the vertical, α is the angle of the baseline from the horizontal, and λ is the wavelength of the satellite.

Orbital phase corrections can be made in processing by precisely tracking the orbit of the satellite. Onboard radar altimeters and laser retroreflectors are utilized to determine the precise location of the satellite in orbit from the ground after the images are acquired. Orbital corrections are generally made during first steps of processing, as the orbital phase is generally the largest contributor to interferometric phase.

1.4.3 Phase contribution associated with topography

For each image pair with a non-zero baseline, a contribution to the phase due to the topography of the region will be included in the phase measurement. This is because of a parallax effect between the two different viewing geometries. Phase

contributions due to topography will concentrate fringes in areas with high topographic relief, similar to that of a contour map (Figure 1.7), which make this useful in digital elevation modeling. The elevation change for each fringe can be determined by calculating the height ambiguity, h_a, which is dependent on the wavelength, incidence angle, and slant range, R (i.e. the distance from the satellite antenna to the middle of the image), of the satellite, as well as the perpendicular baseline, $B_\perp$, between the image acquisitions represented by,

$$h_a = \frac{R\lambda \sin\gamma}{2B_\perp} \tag{1.6}$$

Therefore, the height ambiguity will change with each satellite and each SAR image pair used, as height ambiguity is largely dependent on the baseline of the SAR image pair. As a general rule, for the ERS and Envisat satellites, $h_a \approx 10{,}000/B_\perp$, and the JERS-1 satellite, $h_a \approx 47{,}500/B_\perp$. Large baselines result in a small height ambiguity, which means that more fringes will result from topography. For studying earthquake deformation, a short baseline is advantageous because topography contributes a smaller portion of the phase and is more easily removed. Envisat track 121, which is used for examples in this thesis, has an average perpendicular baseline of 143 m, resulting in a height ambiguity of ~70 m. This means that every 70 meters

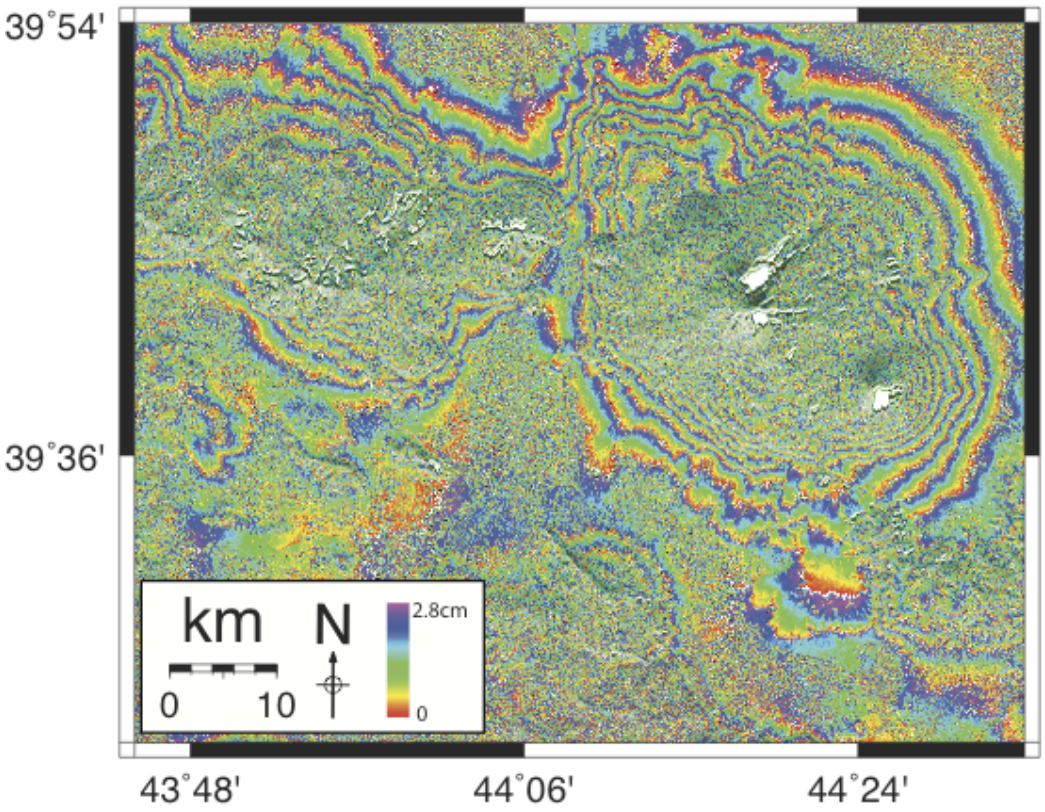

Figure 1.7. An example of phase contribution due to topography is shown at Mt. Tendürek, a shield volcano in the Van region. The phase contribution due to orbital changes has previously been removed. Each fringe represents 70 m of elevation change, which means calculations of the elevation of the peak relative to the base can be made. The white areas have been removed due to errors in the digital elevation model (see section 1.4.3).

of elevation increase or decrease yields a 2π phase change, or 1 full fringe (Figure 1.7). The differences in phase, due to topography, are corrected with a digital elevation model (DEM) which was modified from that produced by the Shuttle Radar Topography Mission (SRTM; Farr et al., 2007) by filling data gaps and holes left in processing by the

SRTM. The SRTM mapped ~80% of the Earth from 60° N latitude to 56° S latitude using radar interferometry.

1.4.4 Phase contribution due to surface deformation

With the effects of viewing angle and topography removed from the phase contribution, the remaining phase changes are a result of deformation and atmosphere. At this point, we assume that the contribution due to atmosphere is negligible (although this assumption does not always hold; see Section 1.5.1) and, therefore, the entirety of the signal at this point is assumed to be due to deformation of the surface. The phase change associated with this deformation is shown by,

$$\Delta\phi = \frac{4\pi\Delta R}{\lambda} = \left(\frac{4\pi}{\lambda}\right)\mathrm{u}.\hat{\mathrm{p}}. \tag{1.7}$$

where u is the three-dimensional displacement of the ground and $\hat{\mathrm{p}}$ is a unit vector pointing from the center of the pixel to the satellite antenna. This is a 1-dimensional line-of-site measurement (i.e. the movement is made in terms of the change in distance between the satellite and the ground target in the satellite 'line-of-sight' direction).

1.5. Limiting factors in InSAR

While InSAR provides a research tool for use in spatially dense data sampling in inaccessible and/or possibly dangerous areas, there are factors that can limit its usefulness. These include atmospheric phase delays, data coverage control and phase errors that limit correlation.

1.5.1 Phase contribution due to atmosphere

In the previous section, it is assumed that the phase contributions due to the atmosphere are negligible, however, atmospheric effects may add a significant amount of phase change to interferograms. Water vapor in the troposphere slows the emitted and reflected waves, thus introducing an additional phase delay. This delay can appear as range changes of up to 10 cm and mask smaller signals such as interseismic deformation. The effect is more pronounced in storm activity, such as thunderstorms, although observable weather is not necessary to cause a large phase change. Currently, atmospheric effects are rarely removed. It can be accomplished, however, by employing the help of Global Position System (GPS) measurements, randiosonde measurements and/or numerical weather models (e.g. Webley et al., 2002; Li et al., 2008).

1.5.2 User control over data acquisition and data coverage

The end user has little control over the data acquisition planning of the SAR satellites. In many cases there are conflicting applications, in which many users want acquisitions in different places on the same orbit. There is also insufficient power supply and incompatible modes of operation to acquire all the requested imagery. During the interval December 1993 to March 1995, ERS-1 went into in a 3-day repeat orbit, which means that the satellite was imaging few areas of the Earth with short temporal timescales. Unfortunately, the spatial coverage at this time was limited to specific satellite tracks that did not include the Northridge, California area at the time of the 1994 earthquake. The satellite did not return to its normal 35-day orbit, to image the Northridge area, until March 1995, collecting its first image acquisition after the earthquake on April 5, 1995, well over a year after the event.

1.5.3 Phase errors that cause decorrelation

Noisy interferograms lack fringes and have the appearance of a speckled image. This is a result of decorrelation, which can be in response to of such problems as a lack of surface preservation and excessive gradients.

1.5.3.1 Surface preservation

Interferometric correlation is a measurement, with values between 0 and, 1 that refers to the similarity of the pixel phase between a pixel and its neighbors in two SAR images (See section 1.4). A correlation of 1 implies that there is no pixel phase change between images, while a correlation of 0 indicates that the pixel phase has completely changed between acquisitions and will not cancel when the interferogram is formed (Figure 1.8a). Such changes in wave backscatter can be attributed to the growth of trees, seasonal variations such as snow, the plowing of fields and the presence of water. Also, in the case of earthquakes, surface ruptures, building damage and landsliding in the epicentral area may cause decorrelation. The relationship between interferogram fringes and pixel correlation can be seen in Figure 1.8. Areas that show high values of correlation correspond with areas in the interferogram where fringes are observed.

1.5.3.2 Excessive gradients

A single pixel cannot have a phase change of more than 2π over a single pixel and remain correlated. In the case of the ERS and Envisat satellites, this is 2.8 cm of range change. The L-band wavelength of the JERS-1 satellite is longer, and therefore generally has the advantage of greater coherence over the shorter wavelength satellite images. This is dependent on baseline separation as well, as the phase

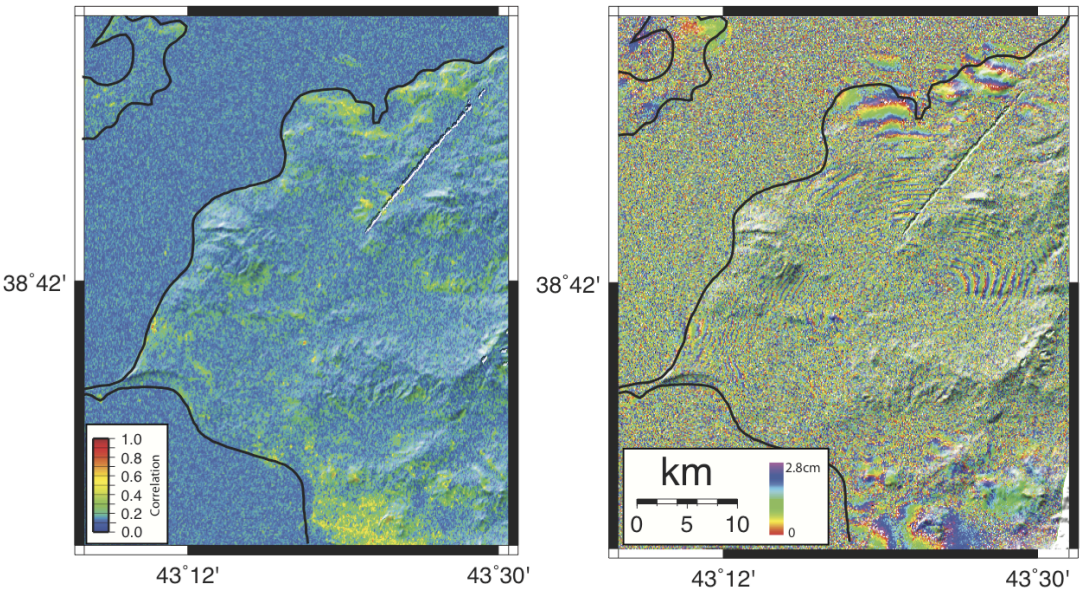

Figure 1.8. a) correlation of the SAR images and b) interferogram of the epicentral region of the Van Earthquake from Envisat track 394 spanning the dates 07/22/2011-11/19/2011. Large amounts of noise are visible in the interferogram, which correspond to low areas of pixel correlation between the SAR images. This low correlation is most likely caused by snowfall in this area. Also visible is Lake Van in the northern and eastern portions of the image, which also results in decorrelation, as the shape of water at the surface is effectively random. Areas in which the fringe pattern is visible are where the interferogram has a higher correlation. Unfortunately, this interferogram contains too much noise to be useful in modeling.

change due to orbital separation may not be greater than 2π over the size of a pixel. Furthermore, an increase in baseline will decrease the height of ambiguity, causing more fringes due to topography over a given area. For the above mentioned reasons, there is a critical baseline, B_c, above which interferometry is not possible, expressed as,

$$B_c = \frac{\lambda R}{2R_y \cos 2\gamma} \tag{1.8}$$

where R_y is the range resolution, which is the minimum separation that two points on the ground can be separated in the range direction. For the ERS-1 and Envisat satellites, $B_c \approx 1100$ m, while for the longer wavelength, JERS-1 satellite, $B_c \approx 7$ km. Interferometry is most likely not possible near these baseline lengths, which require ideal conditions – a successful interferogram would require the topography to be perfectly flat.

1.5.4 Data gaps due to layover and DEM errors

Data gaps may appear in an image due to layover, which occurs when the slope angle of the target, such as a mountain, is greater than the incidence angle of the radar. This causes the radar echoes to reflect off the top of the target before the base, which results in geometric distortion of the image (Figure 1.9), as the top of the mountain is closer to the satellite than the base. Furthermore the information on the opposite side of the mountain will be shadowed as no waves will reach this area. This may also result in missing data when calculating a DEM. Without DEM data, the phase contribution associated with topography cannot be corrected and the data in that area is lost. Such DEM errors can be seen in the white areas in Figure 1.7.

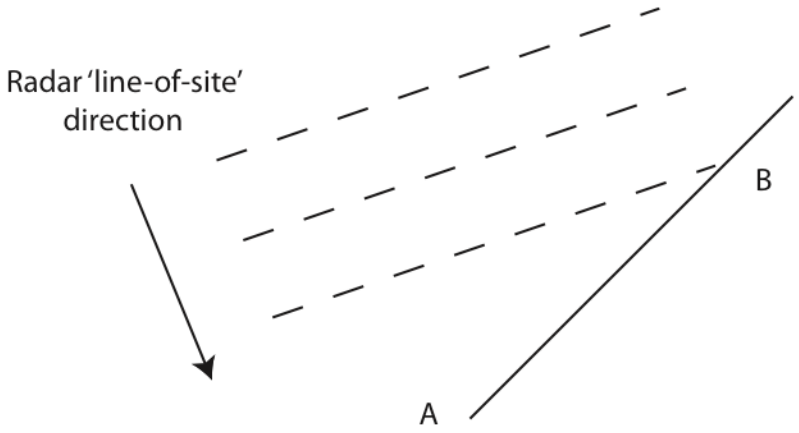

Figure 1.9. Radar layover. The dashed lines represent the radar pulses, while the solid line represents the slope of the target. The radar pulses reflect off the top of the target (B) before the bottom (A).

1.6. InSAR processing

The interferograms in this thesis are processed using the JPL/Caltech Repeat Orbit Interferometry Package (ROI_PAC; Rosen et al., 2004). A simple description of the processing is described below.

1.6.1 Processing the interferogram

In order to difference the phase of 2 SLC images, the first step is to coregister (i.e. match) the images and sample them onto the same geometry. This is achieved using the amplitude of the images, which allows for the matching of common features between the 2 images and will account for any shifts between them in space. An

initial estimate using the orbital information is made for the offset between the two images. Matching is attempted at multiple locations in which a 64X64 pixel search area from the master image (i.e. the first image acquired in time) is used to search a 128X128 pixel window in the slave image (i.e. the second image acquired in time) where the images are expected to match. The search area in the master image is cross-correlated with the slave image and the peak in cross correlation is taken as the match. The slave image is then resampled into the master image geometry. Once the images are coregistered, the master image is multiplied by the complex conjugate of the slave image to form the interferogram. The amplitude of the interferogram is the product of the amplitudes of the two SAR images, and is used only for geocoding purposes, and is explained below. The phase of the interferogram is related to the range change between the two image acquisitions.

Once the interferogram is formed, it will contain phase contributions associated with orbital viewing differences, topography, atmosphere and deformation. The phase contributions not related to surface deformation that can be corrected are subtracted from the interferogram in processing, as mentioned above.

1.6.2 Phase unwrapping and geocoding

Once the corrections to the interferogram have been made, the interferogram is unwrapped. In this step, the 2π modulo 'wrapped' phase signal (i.e. the fringes) is

summed (similar to Figure 1.6) and converted to a continuous 'unwrapped' signal. The branch-cut algorithm (Goldstein et al., 1988) implemented within ROI_PAC is used for phase unwrapping. To be sure that noisy, thus unreliable, data are not retained, the algorithm requires a noise-free path between unwrapped sections of the interferogram. A correlation threshold is specified and the algorithm unwraps data that are connected to a given starting point with a correlation value greater than or equal to the set threshold. If there is a break in correlation across the interferogram (e.g. there are steep mountains in the middle of the interferogram which cause decorrelation), the user may manually 'bridge' the two sides by specifying how many fringes separate the two sections when the fringes in the break are observable to the eye. Because the image is in radar geometry, effectively a mirror image of the surface of the Earth as seen from above, the image is geocoded and matched to the DEM in order to convert it to geographical coordinates.

1.7. Post processing

1.7.1 Quadtree decomposition

Since the number of data points that are included in an interferogram are quite large (i.e. millions of data points), a curvature based quadtree decomposition is applied to the unwrapped phase of the data in order to reduce the number of data points (to

between 700 and 1200 data points) and consequently increase the computational efficiencies in modeling (e.g. Simons et al., 2002; Funning et al., 2007; Figure 1.10). This is justifiable as InSAR data have a high degree of spatial correlation (e.g. Hanssen, 2001), therefore, a similar level of independent information can be retained with significantly fewer data points. This method densely samples the unwrapped data in the areas with the greatest curvature in the deformation pattern near the epicentral area. The far-field deformation, however, is sampled less densely, as the deformation signal does not extend to this area. Figure 1.11 shows a flow diagram of the steps used in postprocessing and subsequent modeling.

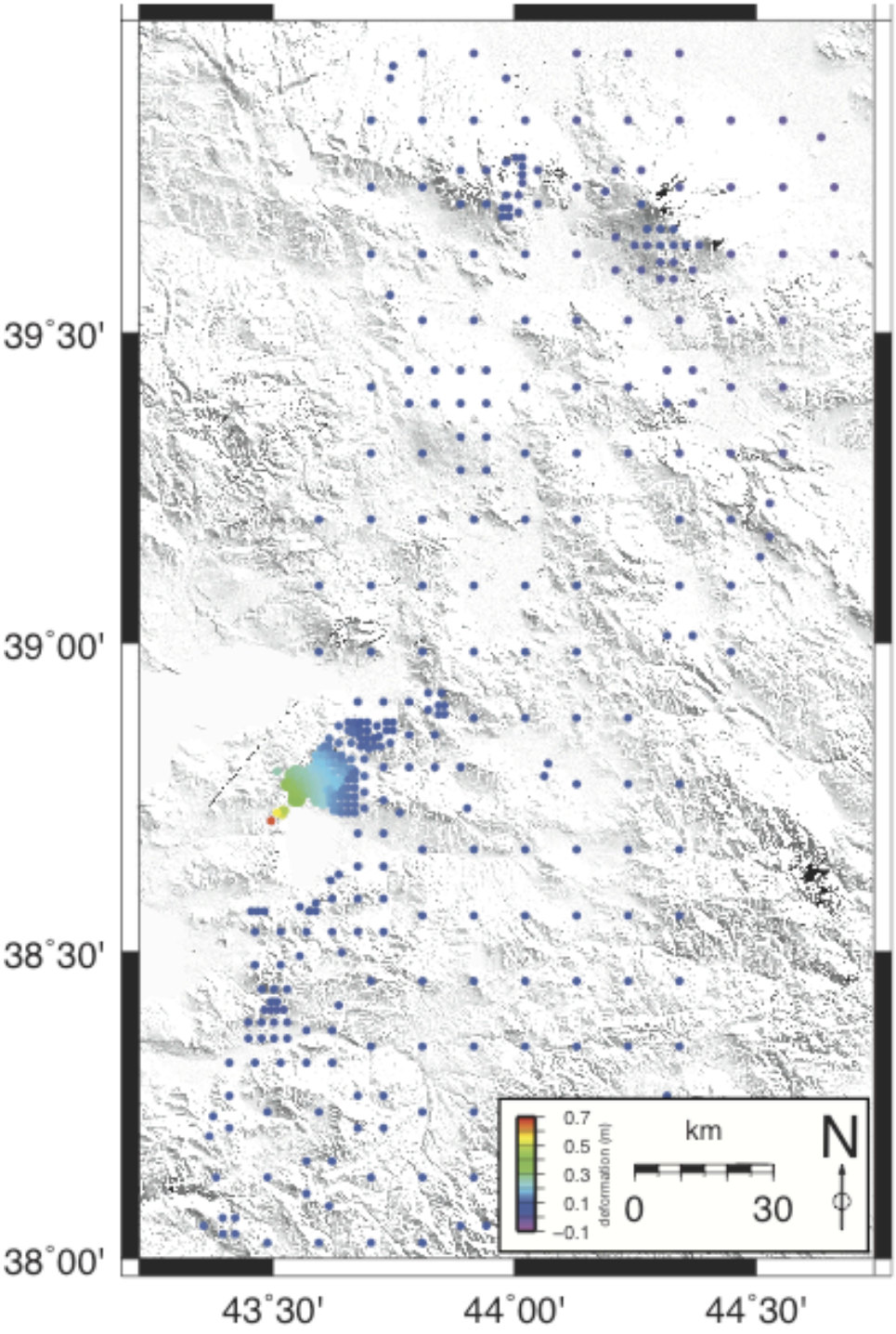

Figure 1.10. Results of a quadtree decomposition of the Envisat track 121 interferogram of the Van earthquake. The data are sampled more densely in the epicentral region of the earthquake. Some far field areas are sampled more densely as the phase change due to topography has not been completely removed due to DEM errors.

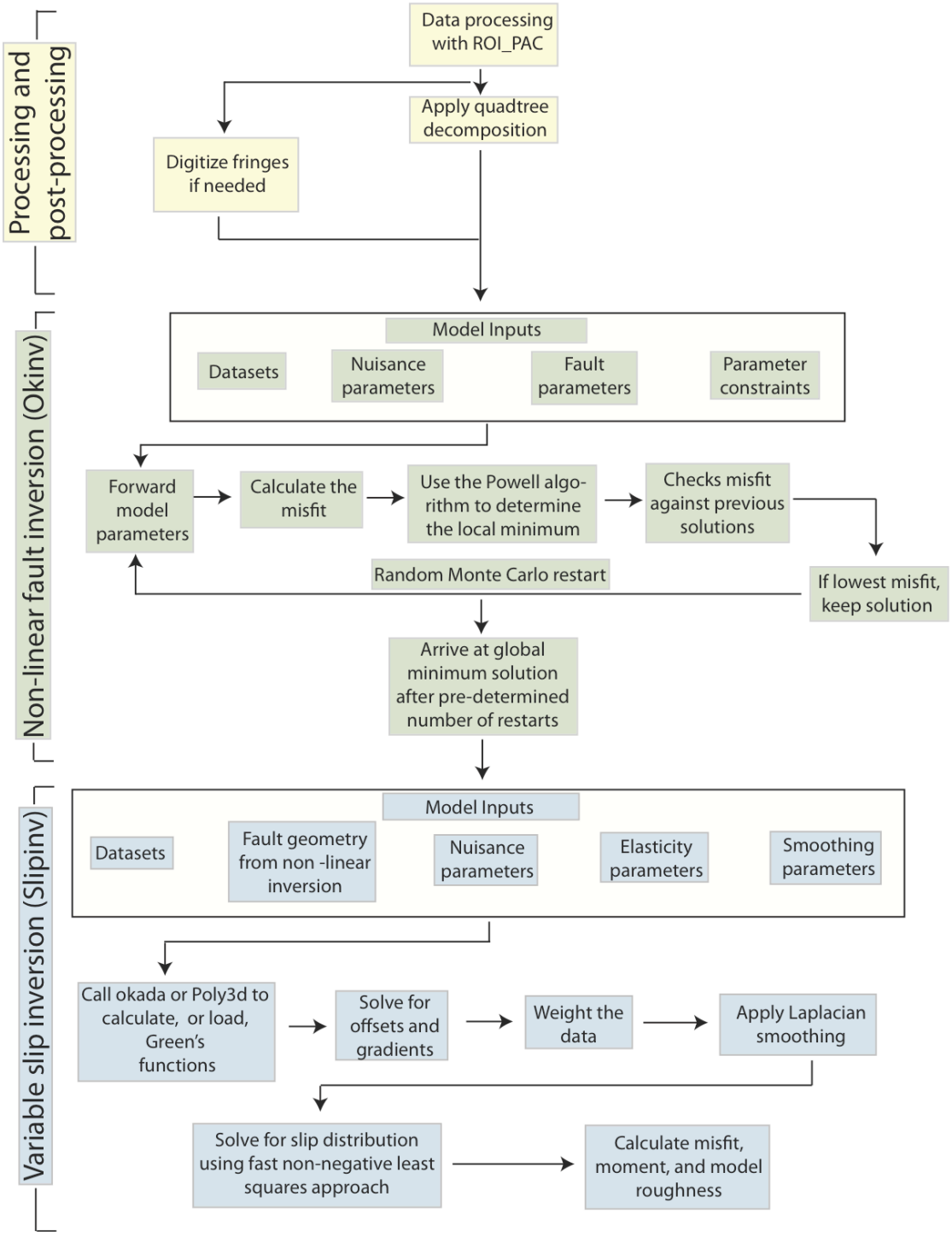

Figure 1.11. Flow of data processing and model calculation from coseismic deformation due to earthquakes. Detailed explanations are given in the text.

1.7.2 Digitizing fringes

When InSAR fringes can be identified by visual inspection, but are too decorrelated for automated unwrapping to be successful, the fringes may be digitized to generate displacement data that can be modeled. This involves loading the image into GIS software, Google Earth or any program with a geographical coordinate reference. Geographic coordinates along each fringe are then generated by tracing each successive fringe boundary with a polyline, whose waypoints can then be exported as an ASCII file. The displacement values of those data points are shifted in order to match the previously unwrapped data in order to obtain an accurate measurement of their displacement. For the Van earthquake, data points are digitized from an image of a COSMO-SkyMed interferogram, processed by Eric Fielding at JPL (Figure 1.12; http://supersites.earthobservations.org/van.php).

1.8 Coseismic source modeling

Once data processing is complete, a source model of the earthquake may be calculated. This is done in two steps; first, the fault geometry is determined using an optimized non-linear inversion method. A non-linear method is necessary, because a change in most fault parameters by some amount will not change the surface deformation pattern by a proportional amount.

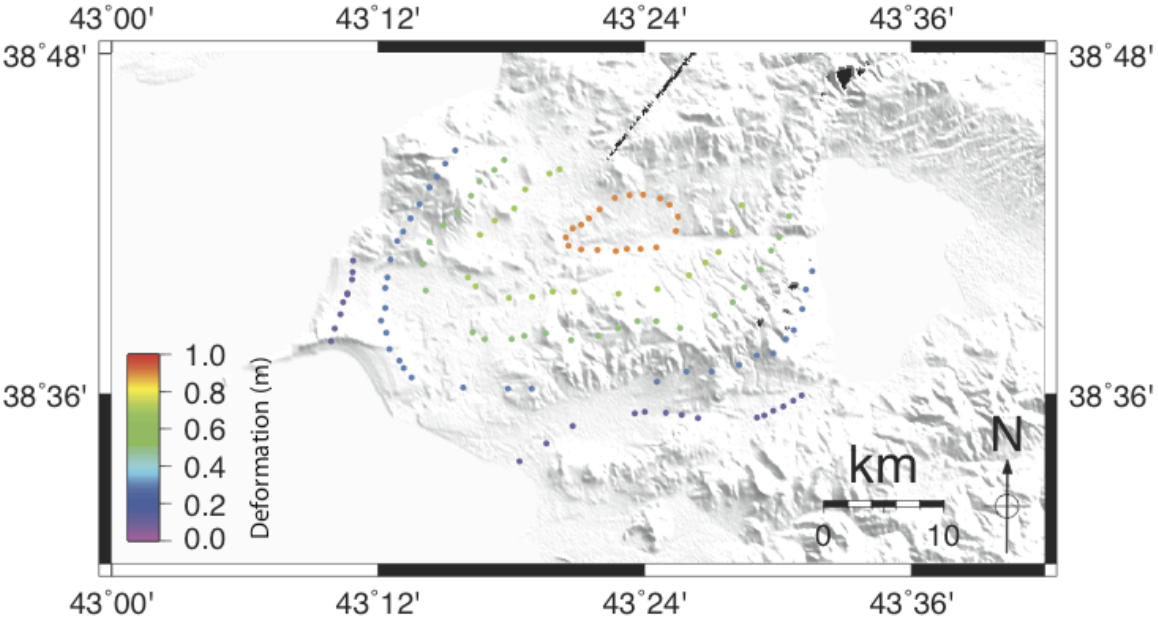

Figure 1.12. Fringes of a publicly available Cosmo-Skymed interferogram of the epicentral area of the Van earthquake are digitized to improve our data coverage in that area. We are unable to get access to the raw SAR data, and so are unable to produce our own interferogram of this area.

This fault geometry is then held fixed and a variable slip distribution can be estimated (i.e. a map of slip on the fault surface). The relationship between slip and deformation is linear, in that a change in slip (i.e. doubling the slip) will yield the same factor in surface deformation.

1.8.1 Uniform slip, rectangular dislocation modeling

In order to determine preliminary fault geometry, the *okinv* code is used (Clarke et al., 1997; Wright et al., 1999), assuming the fault can be described as a uniformly slipping, planar, rectangular dislocation in a homogenous elastic halfspace (Okada, 1985). The user specifies initial starting model parameter values (e.g. fault

orientation, dimensions, location and slip), as well as a priori bounds for those parameters and any additional 'nuisance parameters' to be solved for that account for non-earthquake effects presented in the data, such as static offsets, gradients, and rotations, in the case of GPS. At first, the initial parameter values and bounds may be determined from other solutions, such as the Global Centroid Moment Tensor (GCMT), previous studies and preliminary models. The parameter bounds can be narrowed as the program converges towards a global minimum misfit solution.

Okinv employs a downhill Powell algorithm, which runs the Okada routine multiple times and seeks to find the set(s) of model parameter values that correspond to a local minimum of a penalty function relating to the fit of the model to the data. Each time an Okada model is computed, the penalty function is calculated, and the lowest penalty function is chosen as the local minimum. Initially, 1 parameter is changed to determine the 'downhill' direction to the local minimum in misfit space, then multiple parameters are varied at orthogonal angles to this direction in order to eventually converge on the local minimum (Figure 1.13). However, this process is highly dependent on the initial values and converges only to a local minimum. Due to this, 100 Monte Carlo restarts at random initial values within the set of constrained parameters are used to aid the program in converging on a global minimum solution. This method inverts for strike, dip, rake, slip, fault length, top and bottom fault depth, as well as the x and y position of the projected trace of the

fault at the surface. The best-fitting fault solution is chosen by selecting the lowest residual root mean square (RMS), which is determined by,

$$RMS = \sum_{i}^{n} \sqrt{\frac{(obs_i - calc_i)^2}{n}} \tag{1.9}$$

where *obs* is the observed, or measured displacement of the *ith* data point, *calc* is the calculated model displacement at that data point and *n* is the total number of data points used in modeling.

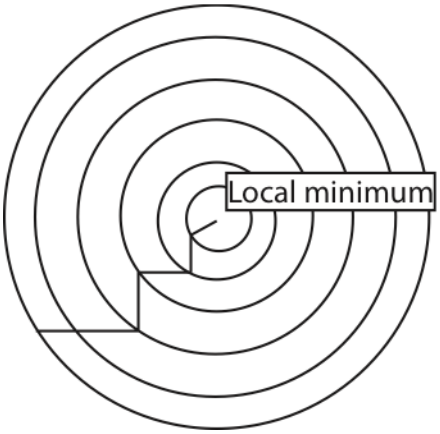

Figure 1.13. Illustration of the Powell algorithm in misfit space. One parameter is changed initially to determine the 'downhill' direction towards the local minimum. Multiple parameters are then changed orthogonal to this direction to converge on the local minimum. Each ring represents equal amounts of misfit with the local minimum at the center.

The fault geometry for our best-fitting fault model of the Van earthquake is shown in Table 1.2. The model is poorly resolved due to poor data coverage and the lack of data near the edge of the deformation pattern because of the lake surrounding the

epicenter. A large tradeoff between dip and the position of the fault projected to the surface occurs because of the lack of data. Due to this, dip is fixed at 54° which is consistent with other preliminary models (i.e. Atzori et al., 2011; Fielding et al., 2012). The dip direction is constrained by the aftershock pattern, which suggests a north-dipping fault. The deformation pattern as a result of this model is shown in Figure 1.14 and the data and residual deformation is shown in Figure 1.15.

Fault parameter	**Single fault dislocation**
Strike	259°
Dip	54°
Rake	164°
Slip	7.1 m
Length	21.3 km
Top depth	8.5 km
Bottom depth	17.7 km
Longitude of fault projection	43.29°E
Latitude of fault projection	38.59°N
Moment	5.1×10^{19} Nm
RMS	2.72 cm

Table 1.2. Fault parameters of the best-fitting model for the Van earthquake.

1.8.2 Variable slip modeling

Since the relationship between slip and surface deformation is linear, the best-fitting fault geometry is held fixed in order to invert for a variable slip distribution. The *slipinv* code (Funning, 2005) is used to invert for a preferred slip distribution on

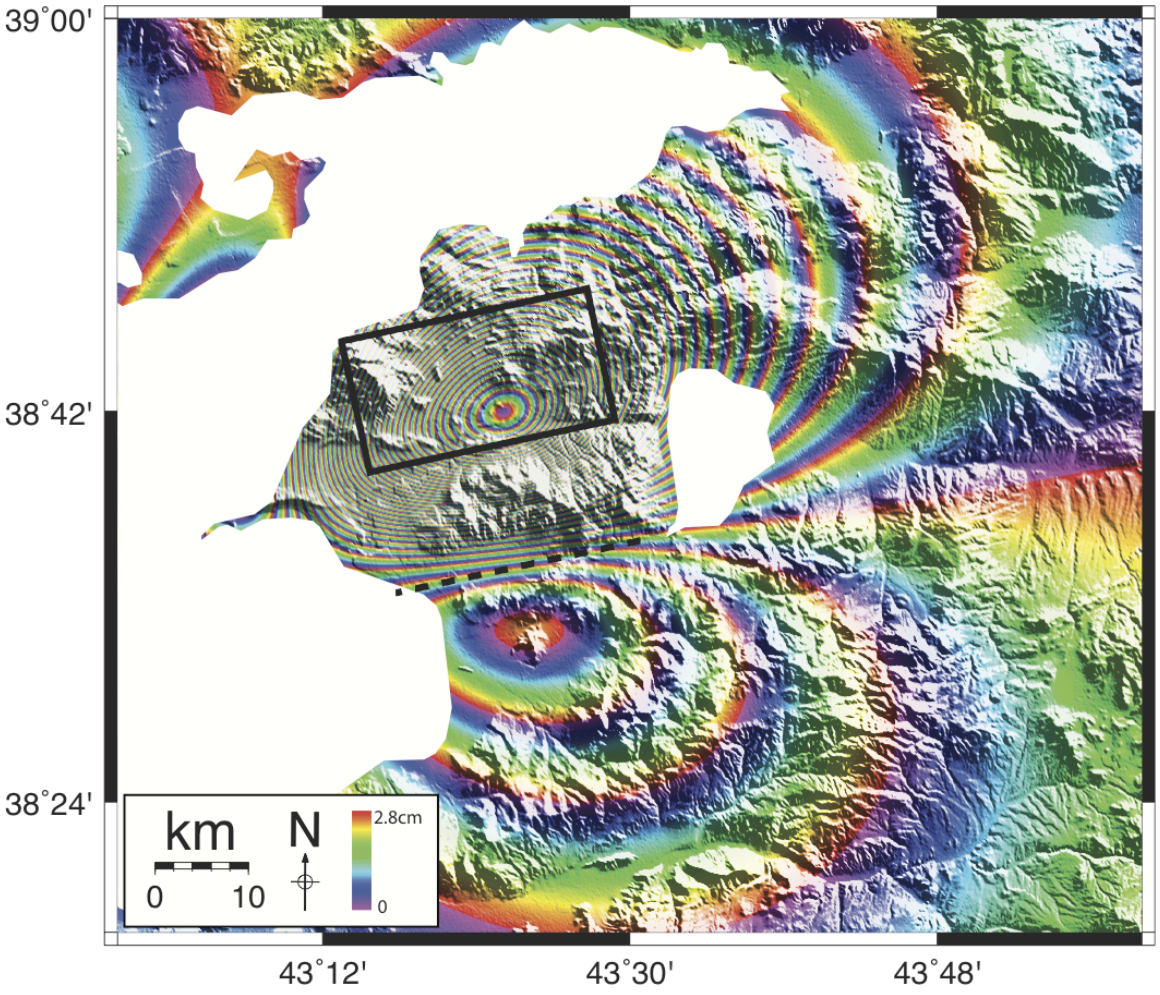

Figure 1.14. Surface deformation of the best-fitting rectangular dislocation model. Each fringe represents 2.8 cm of displacement towards the satellite. The white areas represent Lake Van to the west and the smaller Lake Ercek to the east. The black rectangle represents the fault at depth and the dashed line represents the surface trace of the fault projected to the surface.

the best-fitting fault geometry, as determined from the non-linear Okada inversion using *Okinv*. The fault is divided up into M smaller fault patches, and a forward model is calculated for each patch using the Okada routine, placing 1 m of slip on each of these fault patches, and computing the predicted displacement at each of the N data point locations. These forward modeled displacements form the columns of a

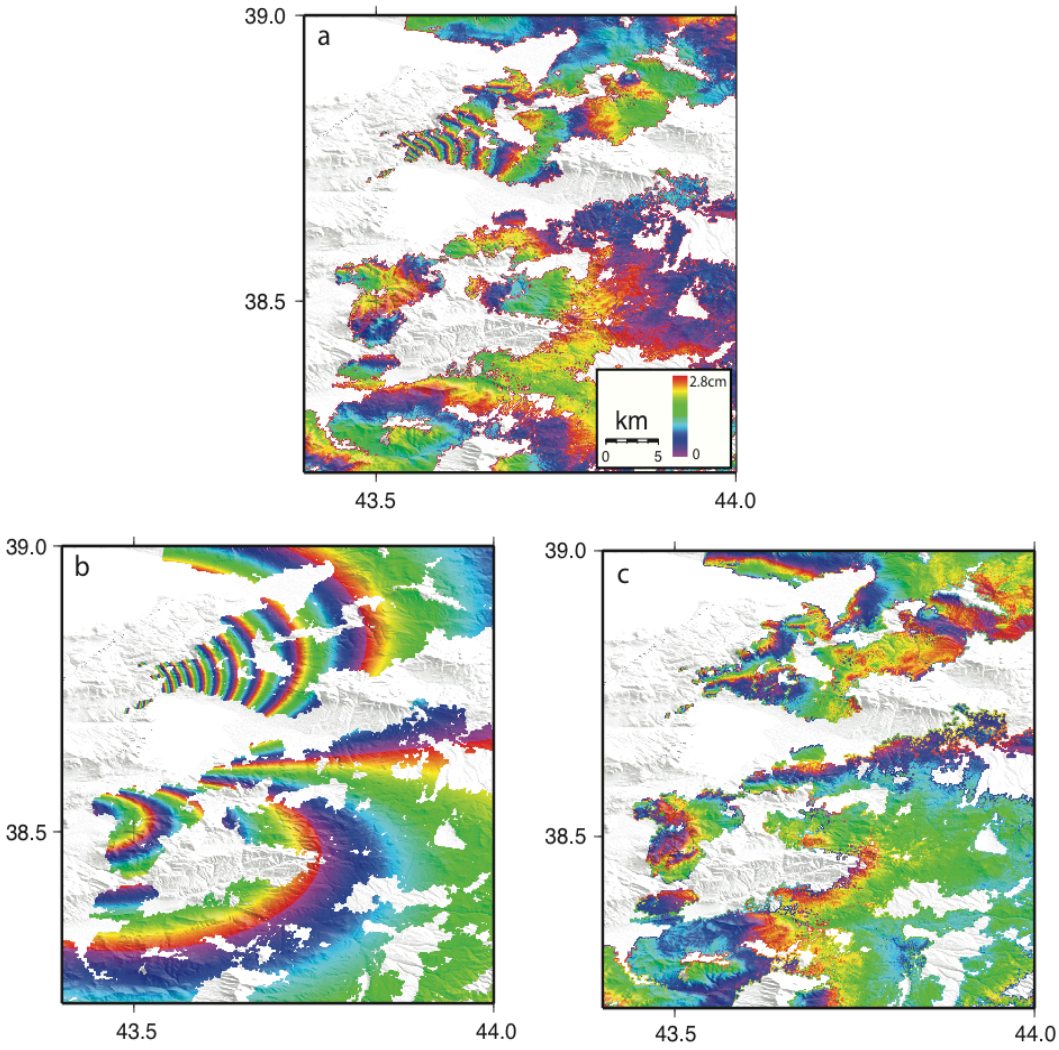

Figure 1.15 Envisat track 121 a) data, b) model and c) residuals of the Van earthquake.

N X *M* kernel matrix, (or matrix of Green's functions), **H**, which relates the surface deformation to the slip on the fault. Thus, the observed data, **d** are related to the slip on each patch, **a**, by

$$\mathbf{d} = \mathbf{H}\mathbf{a} + \mathbf{e} \tag{1.10}$$

where **e** is a vector of random errors. Slip can then be solved for through a least squares inversion shown by,

$$\mathbf{a} = \left[\mathbf{H}^{\mathrm{T}}\mathbf{H}\right]^{-1}\mathbf{H}^{\mathrm{T}}\mathbf{d} \tag{1.11}$$

There will most likely be static offsets, d_0 and gradients in both the north/south, p, and east/west, q, directions (Section 1.8.1). These can be subtracted from the data by,

$$\mathbf{d} = \mathbf{H}\mathbf{a} + \mathbf{e} - \mathrm{d}_0 - \mathrm{p}\mathbf{x} - \mathrm{q}\mathbf{y} \tag{1.12}$$

where **x** and **y** are column vectors containing the east/west and north/south direction locations of each observation point relative to a local origin, respectively. This can be combined into a single kernel matrix,

$$\mathbf{d} = \begin{pmatrix}\mathbf{H} & -\mathbf{1} & -\mathbf{x} & -\mathbf{y}\end{pmatrix}\begin{pmatrix}\mathbf{a}\\ \mathrm{d}_0\\ \mathrm{p}\\ \mathrm{q}\end{pmatrix} + \mathbf{e} \tag{1.13}$$

Additionally, when more than one dataset is used, as in the Van earthquake with Envisat (env) and the digitized Cosmo-SkyMed (CSK) data, another row is added to the matrix with these data in order to solve for each data set independently,

$$\begin{pmatrix} \mathbf{d}_{\mathbf{env}} \\ \mathbf{d}_{\mathbf{CSK}} \end{pmatrix} = \begin{pmatrix} \mathbf{H}_{\mathbf{env}} & \mathbf{-1} & \mathbf{-x}_{\mathbf{env}} & \mathbf{-y}_{\mathbf{env}} & \mathbf{0} & \mathbf{0} & \mathbf{0} \\ \mathbf{H}_{\mathbf{CSK}} & \mathbf{0} & \mathbf{0} & \mathbf{0} & \mathbf{-1} & \mathbf{-x}_{\mathbf{CSK}} & \mathbf{-y}_{\mathbf{CSK}} \end{pmatrix} \begin{pmatrix} \mathbf{a} \\ d_{env0} \\ p_{env} \\ q_{env} \\ d_{CSK0} \\ p_{CSK} \\ q_{CSK} \end{pmatrix} + \mathbf{e} \tag{1.14}$$

Furthermore, in order to avoid unphysical oscillatory slip as well as smooth the model, the data is smoothed using Laplacian smoothing, as the best-fitting model will often place large amounts of slip near patches that do not slip. This difference in slip is not physical, as it would create a strain gradient that would break the surrounding rock. The slip difference occurs because the model is unstable due to the large number of patches in the fault mesh effectively outnumbering the independent data points, leading to an underdetermined (and unstable) inverse problem. Smoothing effectively reduces the number of parameters stabilizing the inverse problem. The smoothing factor, κ, which controls the level of influence of the smoothing on the model, is chosen by selecting the best tradeoff between slip roughness and residual RMS. Laplacian smoothing is added to the inversion by adding a row to both the kernel and the displacement matrix i.e.

$$\begin{pmatrix} \mathbf{d}_{\mathbf{env}} \\ \mathbf{d}_{\mathbf{CSK}} \\ \mathbf{0} \end{pmatrix} = \begin{pmatrix} \mathbf{H}_{\mathbf{env}} & \mathbf{-1} & \mathbf{-x}_{\mathbf{env}} & \mathbf{-y}_{\mathbf{env}} & \mathbf{0} & \mathbf{0} & \mathbf{0} \\ \mathbf{H}_{\mathbf{CSK}} & \mathbf{0} & \mathbf{0} & \mathbf{0} & \mathbf{-1} & \mathbf{-x}_{\mathbf{CSK}} & \mathbf{-y}_{\mathbf{CSK}} \\ \kappa\mathbf{S} & \mathbf{0} & \mathbf{0} & \mathbf{0} & \mathbf{0} & \mathbf{0} & \mathbf{0} \end{pmatrix} \begin{pmatrix} \mathbf{a} \\ d_{env0} \\ p_{env} \\ q_{env} \\ d_{CSK0} \\ p_{CSK} \\ q_{CSK} \end{pmatrix} + \mathbf{e} \quad . \tag{1.15}$$

Here **S** is a sparse matrix containing the smoothing constraints for each patch on the fault.

The preferred slip model is shown in Figure 1.16. Slip peaks at just over 5 m with shallow slip towards the west of the fault. This model agrees well with the preliminary model calculated by Atzori et al., (2011) in regards to slip, however, the strike calculated from the preliminary model of Atzori et al. (2011) is ~20° less and moment is ~28% more than this preliminary model. My model is less similar to the preliminary model of Fielding et al. (2012), in which individual inversions of both geodetic and seismic data infer a large (~14 m) slip displacement over a small area due to the short seismic duration of the earthquake.

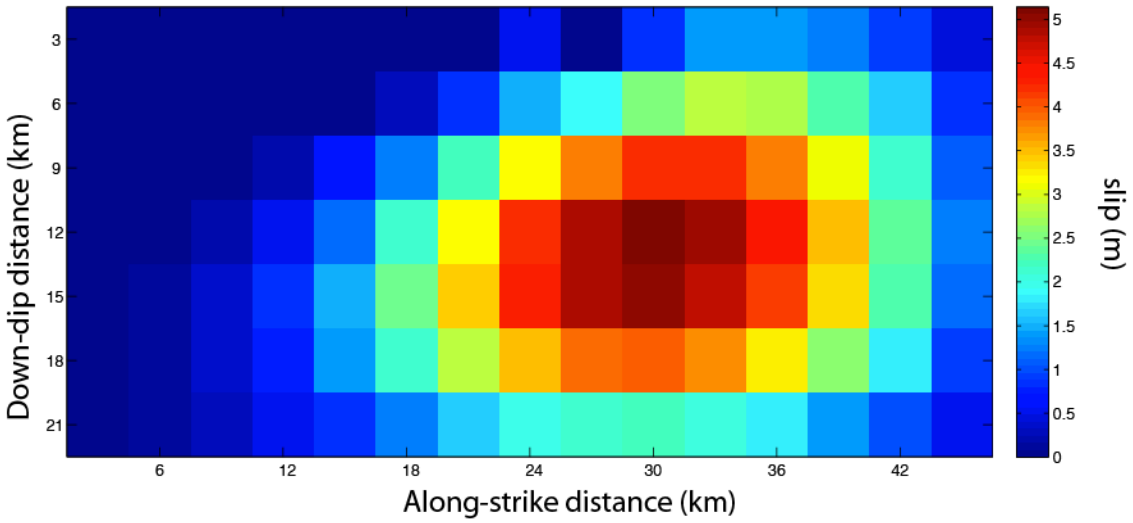

Figure 1.16. The preferred variable slip model of the Van earthquake. Each fault path is ~3km by 3km.

1.9 Reverse faulting and surface deformation

The use of InSAR allows for the measurement and subsequent modeling of earthquakes. In this section, I show how each fault parameter influences the deformation pattern whereby observations of this pattern allow us to infer the fault geometry and slip at depth. Using a single fault, one parameter is altered to show its influence on the deformation pattern. The contributions of dip, rake, slip and depth are modeled on a south-dipping fault striking east-west (90°) to show their influence to surface deformation. Only the contributions for these specific parameters are modeled as the other parameters, such as strike, location and length, merely change the location or orientation of the deformation pattern, and not the pattern itself. Being that this is a reverse fault, the majority of the deformation

occurs as uplift on the hangingwall, while smaller amounts of deformation occur as footwall subsidence. The control parameters are listed in Table 1.3 and remain unchanged unless otherwise noted. Figure 1.17 shows the representation of these parameters on a fault surface.

Fault parameter	**Value**
Strike	90°
Dip	50°
Rake	90° (pure reverse)
Slip	2 m
Length	20 km
Top fault depth	5 km
Bottom fault depth	15 km
Easting of fault center projected to the surface	30 km
Northing of fault center projected to the surface	37 km

Table 1.3. Fault parameters of the 'control' fault model. Within each test, one parameter varies from the control fault geometry in order to observe the change in surface deformation associated with that parameter.

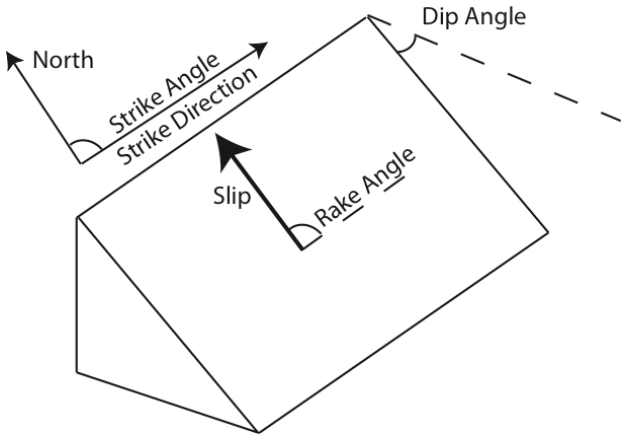

Figure 1.17 Fault geometry. The dip, rake, slip, and fault depth are altered in this chapter to show their influence on surface deformation.

Forward models of each fault solution are calculated using the *Oksar* program (Clarke et al., 1997; Wright et al., 1999) which models surface deformation assuming the fault can be represented by a uniform slipping, rectangular dislocation, buried in a homogenous elastic halfspace (Okada, 1985). Each fringe or full color cycle (red-yellow-blue-red) in the images that follow represents 5 cm of displacement towards the satellite, which in this case is to the east in a descending (north to south) direction. This is a similar viewing geometry to that of the ERS satellites. The cross-sections in each figure are taken along a north-south track through the center of the deformation pattern and are represented by a vertical dashed line in each figure.

1.9.1 Fault dip

Fault dip is altered here in order to demonstrate how it affects surface deformation. Fault dip has a significant control over the ratio of footwall-to-hangingwall deformation in an earthquake (Figure 1.18). In the case of a 30° shallow dipping fault, no significant deformation is observed on the footwall while the hangingwall shows both uplift of ~80 cm in the epicentral area, and subsidence of ~8 cm to the south of the epicentral area. Deformation occurs on both the hangingwall and footwall as strain accumulates on both sides of the fault and is released during an earthquake. With a steeper 50° dipping fault, uplift of ~70 cm is observed on the hangingwall, ~10 cm less than that observed with the more shallow dipping 30°

fault, however, subsidence of ~5 cm is observed on the footwall. The 70° steeply dipping fault shows ~55 cm of uplift, ~15 cm less than that of the control fault. The steep case also shows greater subsidence of ~20 cm on the footwall as well. This dip angle is not likely for a reverse fault as it is quite steep, however, it illustrates the influence of dip on surface deformation. It is observed that shallow dip leads to larger uplift of the hangingwall and smaller subsidence to the footwall and vice-versa

In the case of the Van earthquake, dip is poorly constrained because data at distance from the epicentral area are not available. In this case, a lake bounds much of the deformation pattern, and causes incoherence within InSAR data. As explained, the dip of the fault primarily determines the relative amounts of subsidence of the footwall and/or hangingwall at distance from the epicentral area. Without these data, the dip cannot be well constrained. In cases where the dip direction is unconstrained, additional data (i.e. the aftershock distribution) may provide useful information to determine the direction and amount of dip.

1.9.2 Fault rake

The rake angle of slip determines the along strike symmetry of the deformation pattern (Figure 1.19). When modeled, a decrease in rake angle (i.e. greater left-lateral motion) causes greater asymmetry to the deformation pattern where a lobe

extends in the direction of hangingwall motion. However, displacement in the middle of the deformation pattern does not largely change with varying rake. The digitized fringes measured from the Van earthquake (Figure 1.12) show a widening of the deformation pattern to the east, suggesting oblique slip of the hangingwall in the east direction with a rake of 164°.

1.9.3 Fault burial depth

In order to demonstrate how the burial depth of the fault affects the deformation pattern, the down-dip length is held constant, while the top and bottom depths of the fault are increased by the same amount (figure 1.20). Burial depth affects the amount of uplift as well as the north-south width of the deformation pattern, in the examples shown. Surface rupture (Figure 1.20a) forms a narrow deformation pattern of ~35 km with larger uplift values of ~1.2 m. This also forms a fault scarp, shown by the abrupt transition between the uplift of the hangingwall and subsidence of the footwall. Deep slip (Figure 1.20c) forms a broad ~45 km pattern with smaller uplift of ~45 cm measured at the surface. As shown, an increased burial depth causes the deformation pattern to widen while peak deformation gets smaller. In the same way, the deformation pattern narrows and peak deformation increases with decreased burial depth.

The effect of depth on surface deformation can be clearly seen in the Northridge earthquake deformation pattern between the eastern and western portions of the pattern (Figure 2.6) which will be explained in more detail in Chapter 2. To the east, a broad pattern is observed, representing deeper slip, while to the west a narrow pattern of deformation is observed in the JERS-1 digitized fringes, indicative of lesser shallower slip. This same pattern can also be indicative of rake; however, in this case, the amount of peak uplift is greater to the east where the pattern widens than it is in the west. If this deformation were due to rake, peak uplift would decrease as the pattern widened.

1.9.4 Fault slip

Slip is varied in 1 meter increments between 1 and 3 meters (Figure 1.21) in order to demonstrate the influence of fault slip to the deformation pattern. The amount of slip on a fault contributes to uplift of the deformation pattern, but does not largely change the width of the pattern. The larger slip value of 3 m produces an uplift of ~1.1 meters of surface displacement (Figure 1.21a), while a 1 m slip value forms ~35 cm of uplift when modeled (Figure 1.21c). It is clear in this instance that fault slip and deformation have a linear relationship. Fault slip is increased by a factor of 3 which increases peak surface deformation by the same factor.

1.9.5 Contribution of fault geometry.

As shown above, the specific deformation pattern of an earthquake is influenced by fault geometry and the magnitude of slip, which can be broken down into their contributing components. Dip can be constrained by observing the ratio of hangingwall to footwall deformation. While a steeper dipping fault will cause greater subsidence to the footwall, a shallow dipping fault will have less influence on the footwall, causing greater uplift to the hangingwall and subsidence away from the epicentral area on the hangingwall. The rake of the fault can be observed through the asymmetry of the deformation pattern, in which more oblique slip will produce a larger deformation lobe in the direction of hangingwall movement. Greater magnitudes of slip at shallower depths produce larger surficial uplifts due to reverse faulting. Depth also changes the width of the deformation pattern with shallow movements forming a narrow deformation pattern and deeper slip causing the pattern to widen.

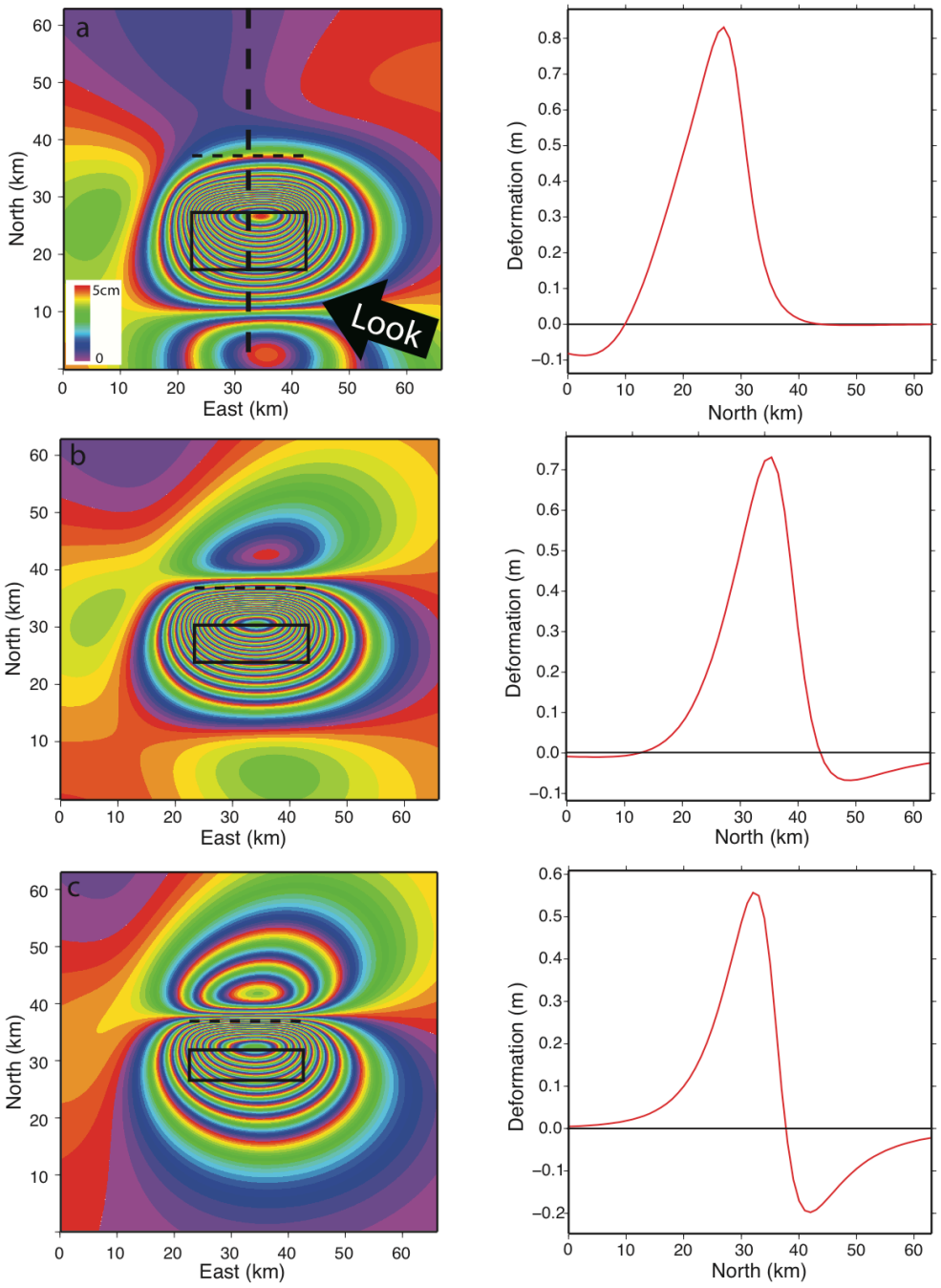

Figure 1.18 The influence of dip on surface deformation. The images on the left represent the surface deformation pattern in map view. Rectangles are the fault position in map view and the horizontal dashed line is the fault projected to the surface, where north of the line is the footwall and south is the hangingwall. The black arrow represents the measuring direction of the satellite. The right images are a north/south cross-section taken from the center of the deformation pattern denoted by the dashed line in figure 3.2a. a) Surface deformation with a 30° dip, b) 50° dip (control), and c) 70° dip. Further explanations are provided in the text.

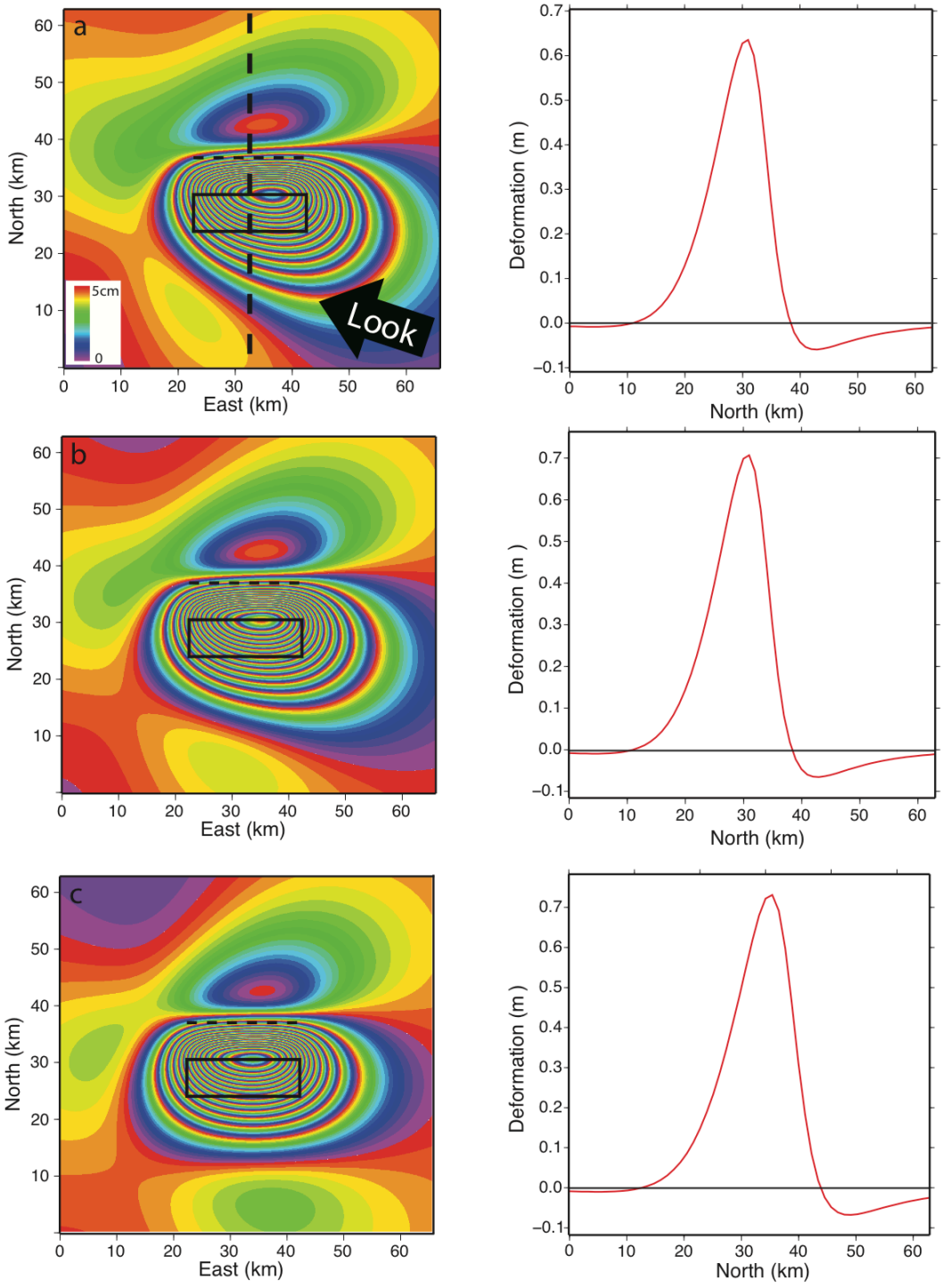

Figure 1.19 The influence of rake on surface deformation. The fault has been given left-lateral oblique slip of a) 60°, b) 75° and c) 90° (pure reverse; control). A smaller rake angle (more right-lateral oblique slip) forms a more asymmetric pattern. This pattern is mirrored about the y-axis with varying degrees of larger rake angles (right-lateral oblique slip).

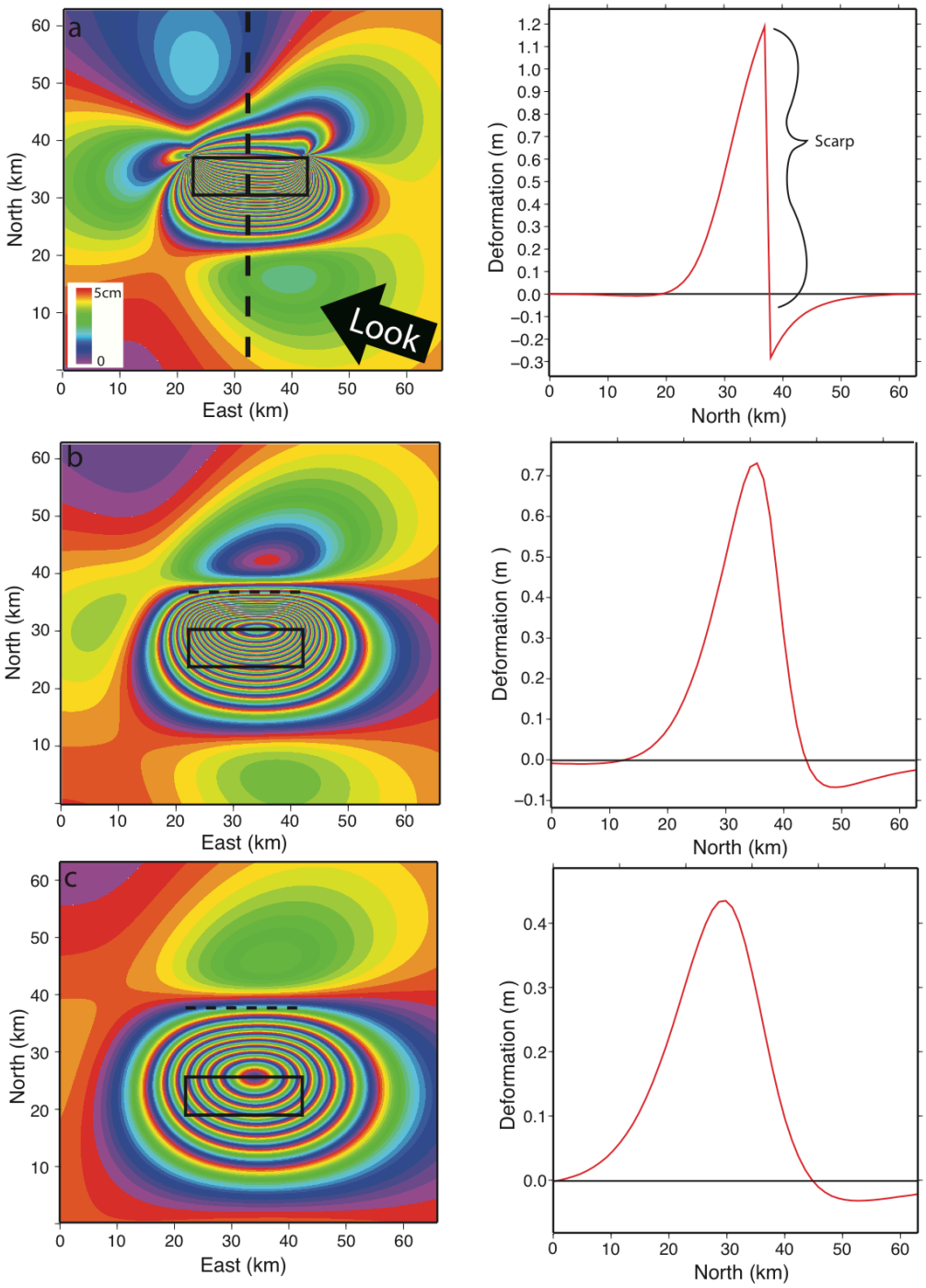

Figure 1.20 The role of depth on surface deformation. a) Surface rupturing reverse fault (0-10 km). b) 5-15 km buried fault depth (control). c) 10-20 km buried fault depth. Depth affects the width and height of the deformation pattern. The deeper slip pattern is wide with less uplift, while shallow slip forms larger uplift over a narrow area. A fault scarp forms when the fault ruptures through to the surface.

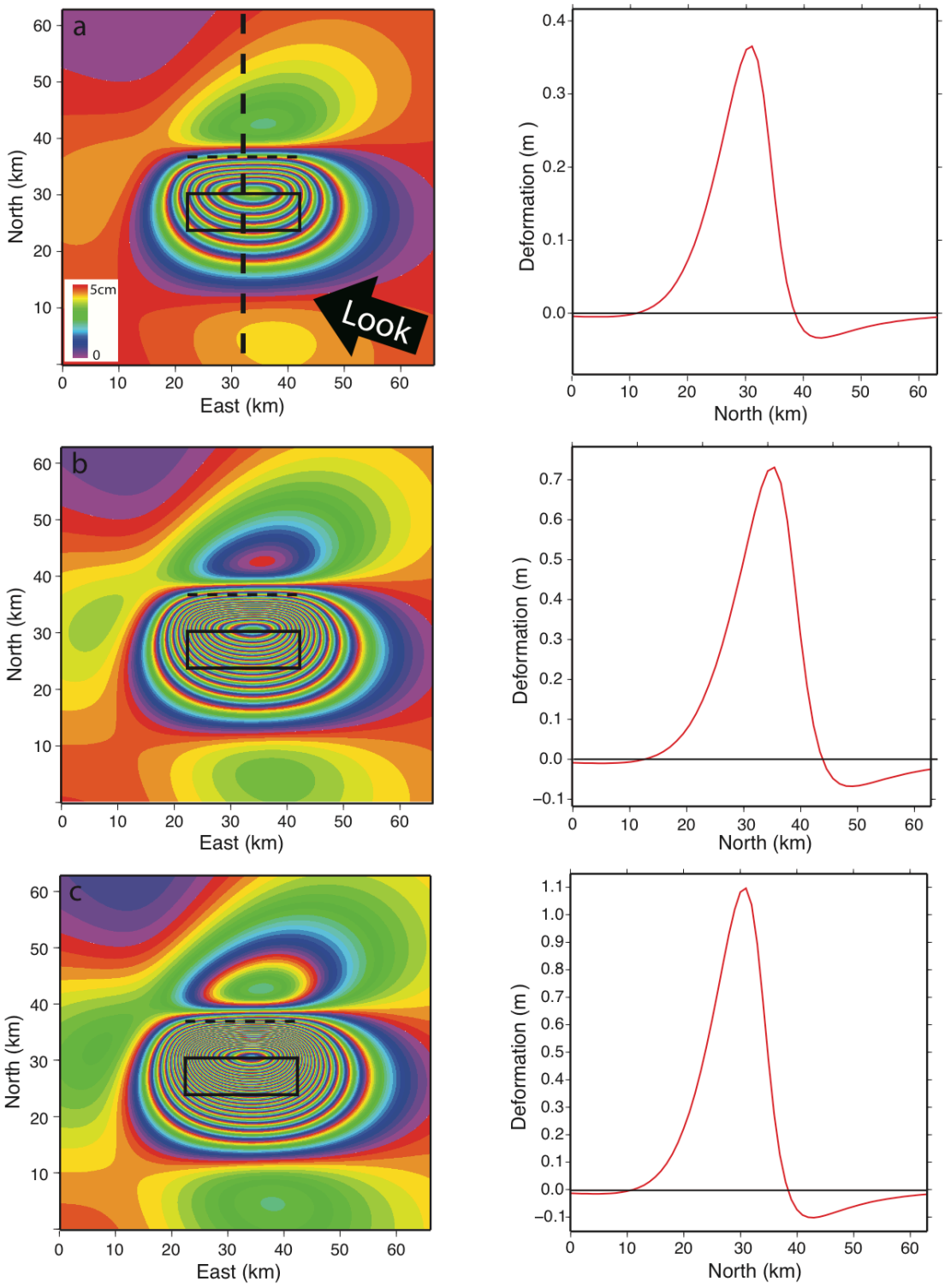

Figure 1.21 The effect of slip on surface deformation with a) 1 meter b) 2 meters (control) c) 3 meters. By scaling slip, the pattern in map view as well as the profile will not change shape, however, the uplift values will increase or decrease with an increase or decrease in slip.

1.9.6 Summary

These examples provide a simple glimpse into the interaction between fault geometry and deformation. Real world examples, however, are more complicated than a simple one fault parameter change. For example, slip amount and buried fault depth, as well as rake and a varying slip depth can yield similar results and be difficult to distinguish. Also, if far field deformation is not available, dip is difficult to determine, which means dip may have large tradeoffs between slip and depth. Knowledge of the interaction between each fault parameter and the surface deformation it causes can help to determine preliminary models.

Chapter 2 The Northridge Earthquake

2.1 Introduction

On January 17, 1994 at 4:30 a.m. local time (PST) a M_w ~6.7 earthquake struck the suburbs northwest of Los Angeles, California (Figure 2.1). Centered on the city of Northridge in the San Fernando Valley, the event caused 33 deaths, and left ~20,000 homeless, while causing ~$20 billion in damages, making this the most costly earthquake since the 1906 San Francisco earthquake (Scientists of the USGS and SCEC, 1994).

The Northridge event differed from other earthquakes of this magnitude in that it generated the largest ground motions ever recorded in an urban environment up to that point, yet left no evidence of a surface rupture (Scientists of the USGS and SCEC, 1994). Peak ground accelerations of up to 1.8g were recorded (Trifunac, et al, 1994; Hauksson et al., 1995; Spudich et al., 1996), ~50% larger than anticipated for an earthquake of this magnitude (Scientists of the USGS and SCEC, 1994; Wald et al., 1996; Somerville et al., 1996). The intense shaking resulted in shallow tensile surface cracking and broken gas and water lines, which caused simultaneous fires and flooding (Hecker et al., 1995; Rymer et al., 1995). While shaking intensities were high, they are explicable in terms of amplification of seismic waves from the large

sediment filled basins in the Los Angeles region (Graves, 1995; Somerville et al., 1996).

In the aftermath of the earthquake, the identification of the Northridge thrust (also known as the Northridge fault), gave rise to a new set of tools for identifying blind thrusts (e.g. geomorphic analysis; Jackson et al., 1996; Vannoli et al., 2004), which have led to the identification of other blind thrusts in the Los Angeles area. It has been suggested that moderate to large earthquakes (i.e. M_w 6.5-7.5) on the blind thrust faults in this region pose significantly greater risk than larger earthquakes on the more distant San Andreas fault, due to the high population density and large shaking intensities expected in this area (Dolan et al., 1995). Due to this, the Northridge event provides an important case study in which to maximize our understanding of earthquakes in this area so we can better prepare for future earthquakes, which are anticipated to occur approximately every 40 years (Scientists of the USGS and SCEC, 1994).

2.1.1 Tectonic setting

The San Fernando Valley is located at the western edge of the Transverse Ranges, which are a range of 2000–3000 m peaks associated with the 'Big Bend', a restraining left bend on the San Andreas fault. As such, the region is undergoing regional contraction, which promotes thrust faulting in which ~10 mm/yr of

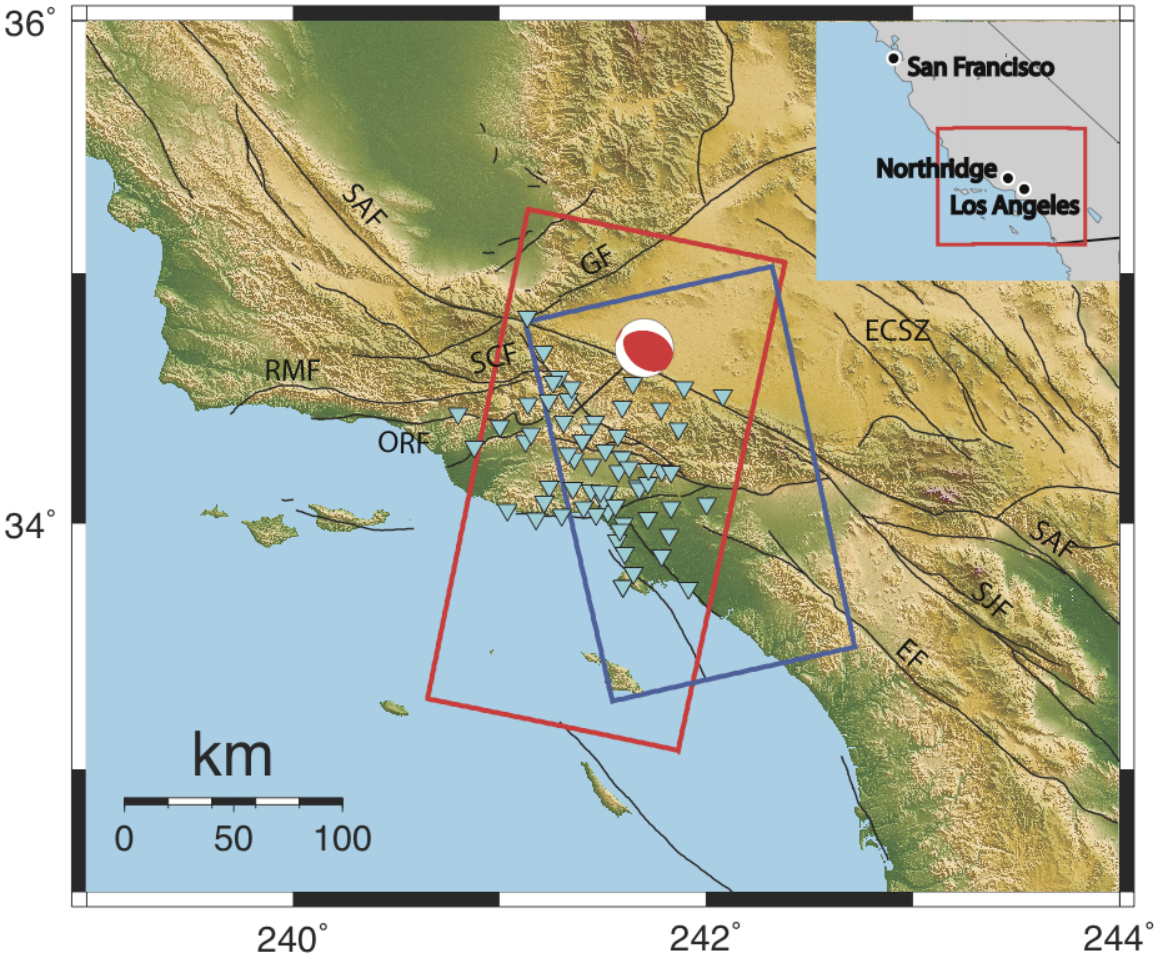

Figure 2.1 Map centered on Northridge, California, showing the surrounding area. The focal mechanism shows the Global CMT solution, inverted blue triangles represent the GPS stations used in this study, while the red and blue boxes represent the ERS-1 and JERS-1 data coverage, respectively. The black lines represent known major fault surface traces of the San Andreas (SAF), San Jacinto (SJF), Elsinore (EF), Garlock (GF), Red Mountain (RMF), San Cayetano (SCF) and Oak Ridge faults (ORF) as well as the Eastern California shear zone (ECSZ).

shortening are accommodated, according to geologic and geodetic evidence (Scientists of the USGS and SCEC, 1994; Huftile and Yeats, 1995; Huftile and Yeats, 1996; Hagar, 1999, Argus et al., 2005).

This region is highly prone to earthquakes as shown by the 1971 San Fernando earthquake, which ruptured the northward dipping Santa Susana fault causing 65 deaths, 2000 injuries and damages of ~$505 million (Stover and Coffman, 1994) just 23 years prior to the Northridge event.

The 1994 Northridge earthquake is inferred to have occurred on the Northridge thrust, a south dipping blind thrust fault that lies 5-8 km below the surface (Scientists of the USGS and SCEC, 1994; Hauksson et al., 1995; Carena and Suppe, 2002), with a slip rate of 1-1.7 mm/yr (Huftile and Yeats, 1996; Davis & Namson, 1994; Dolan et al., 1995; Marshall et al., 2008). Shortly after the earthquake, field teams were sent into the Northridge area to survey the damage and deformation due to the earthquake. These teams of scientists did not observe evidence of surface rupture, although, surface deformations in the way of shallow surface cracking, liquefaction and landsliding were observed (Hecker et al., 1995; Rymer et al., 1995; Stewart et al., 1996; Holzer et al., 1999).

Since the Northridge thrust does not rupture the surface, it had not previously been recognized. Shortly after the event, it was observed that both the hangingwall and footwall of the Santa Susana fault are uplifting. If this had been observed before the event, it might have lead to the discovery of the Northridge thrust, as it termintes against the Santa Susana fault. (Yeats and Huftile, 1995; Mori et al., 1995; Huftile and Yeats, 1996). The Northridge thrust terminating against the Santa Susana fault

is evidenced by the Santa Susana fault surfacing on a hillside, implying uplift of the footwall (Huftile and Yeats, 1996). Currently, blind thrusts are identifiable by means of geologic evidence such as folding (e.g. Stein and Yeats 1989; Shaw and Suppe 1994; Shaw and Suppe 1996), and incised, deflected or abandoned stream channels (Jackson et al., 1996; Vanolli et al., 2004).

2.1.2 Source models and observations of fault geometry.

Previous source models based upon fitting coseismic measurements of GPS (Hudnut et al., 1996; Shen et al., 1996; Wald et al., 1996) , InSAR (Massonnet et al., 1996), leveling (Hudnut et al., 1996; Wald et al., 1996) and seismological data (Wald et al., 1996; Nielsen and Olson, 2000) are described in Table 2.1. The models are relatively consistent in regard to strike and dip orientation, with all models inferring a south-dipping blind thrust fault, buried ~5-8 km below the surface. There are, however, differences in the amount of inferred slip between the different models, due to differences in the amount of observed deformation and shaking implied by different datasets. InSAR coseismic studies (e.g. Massonnet et al., 1996; Murakami et al., 1996), found discrepancies between the GPS derived model of Hudnut et al. (1996) and the measured InSAR displacements, where the GPS data predict surficial displacements of up to ~20cm larger than the InSAR data suggest. These are explained by a lack of GPS data in the epicentral area (Murakami et al., 1996). Additionally, Wald et al. (1996) found a disagreement between measured geodetic

and seismic data and concluded that the geodetic data could be contaminated by permanent displacement due to aftershocks, local or non-tectonic movements of monuments due to intense shaking, or from subsidence caused by oil, gas and water extraction. These measurements may also contain postseismic deformation due to afterslip or viscoelastic flow. This appears plausible as the campaign GPS measurements were completed within weeks of the earthquake (Hudnut et al., 1996), and not directly after, meaning they will most likely contain a postseismic signal. Futhermore, Argus et al. (2005) observed seasonal surface deformation changes in the Los Angeles region due to water management in local aquifers and oil extraction, with amplitudes of ~3 mm/yr and ~5 mm/yr respectively, which may have affected the measurements.

In the weeks and months following the Northridge earthquake, Hauksson et al. (1995) relocated aftershocks from the earthquake and were able to identify the simple geometry of the Northridge thrust. They note that the fault steepens from east to west and that there is a dense clustering of aftershocks towards the top of the thrust fault that coincides with surficial faults. They also suggest that the majority of aftershocks from the Northridge event have a thrusting focal mechanism, indicating that the stress release from the mainshock was not complete. Carena and Suppe (2002) also relocated aftershocks and utilized geologic data in which they were able to identify a more precise 3D geometry of the Northridge

Study	Data source	Description	Main fault model parameters
Hudnut et al., 1996	GPS	Single planar fault with variable and uniform slip models	Strike:110° Dip: 41° Peak slip:2.5m M_0=1.05 x 10^{19} Nm
Massonnet et al., 1996	JERS and ERS InSAR data	3 fault rectangular planar dislocation uniform slip model from InSAR data. Main fault modified from Hudnut et al. (1996). 2 extra faults represent aftershock deformation.	Strike: 110° Dip: 42° Width: 13.5 Length: 10.9 Peak slip: 2.0m M_0=0.942 x 10^{19} Nm
Shen et al., 1996b	GPS	Planar fault with variable slip. Used a second north dipping thrust fault to model deformation.	Strike: 122° Dip: 38° Peak slip: 2.2 m M_0=1.34 x 10^{19} Nm
Wald et al., 1996	Strong motion, teleseismic, GPS and leveling	Single planar fault with variable slip. The majority of slip accumulates northwest of the hypocenter.	Strike: 122° Dip: 40° Peak slip: ~3m M_0=1.3 x 10^{19} Nm
Nielsen and Olson, 2000	Strong motion seismology	Dynamic model of the Northridge earthquake. The model is in agreement with Wald et al. (1996)	Used the fault geometry of Wald et al. (1996) M_0=1.4 x 10^{19} Nm

Table 2.1 An overview of the previous coseismic slip models for the Northridge earthquake produced in various studies.

Thrust. An irregularly shaped wavy/'corrugated' fault plane with the peaks and troughs oriented parallel to the dip direction is inferred. The fault shows a protrusion at the end of a west-east trending along-strike ramp which peaks in the middle of the fault, along strike at ~13 km depth. This protrusion is adjacent to a steep ramp to the west. The Community Fault Model (CFM; Plesch et al., 2007; Figure 2.2), which we use in this study as a fixed fault reference, primarily uses the study of Carena and Suppe (2002) for the model of the Northridge thrust.

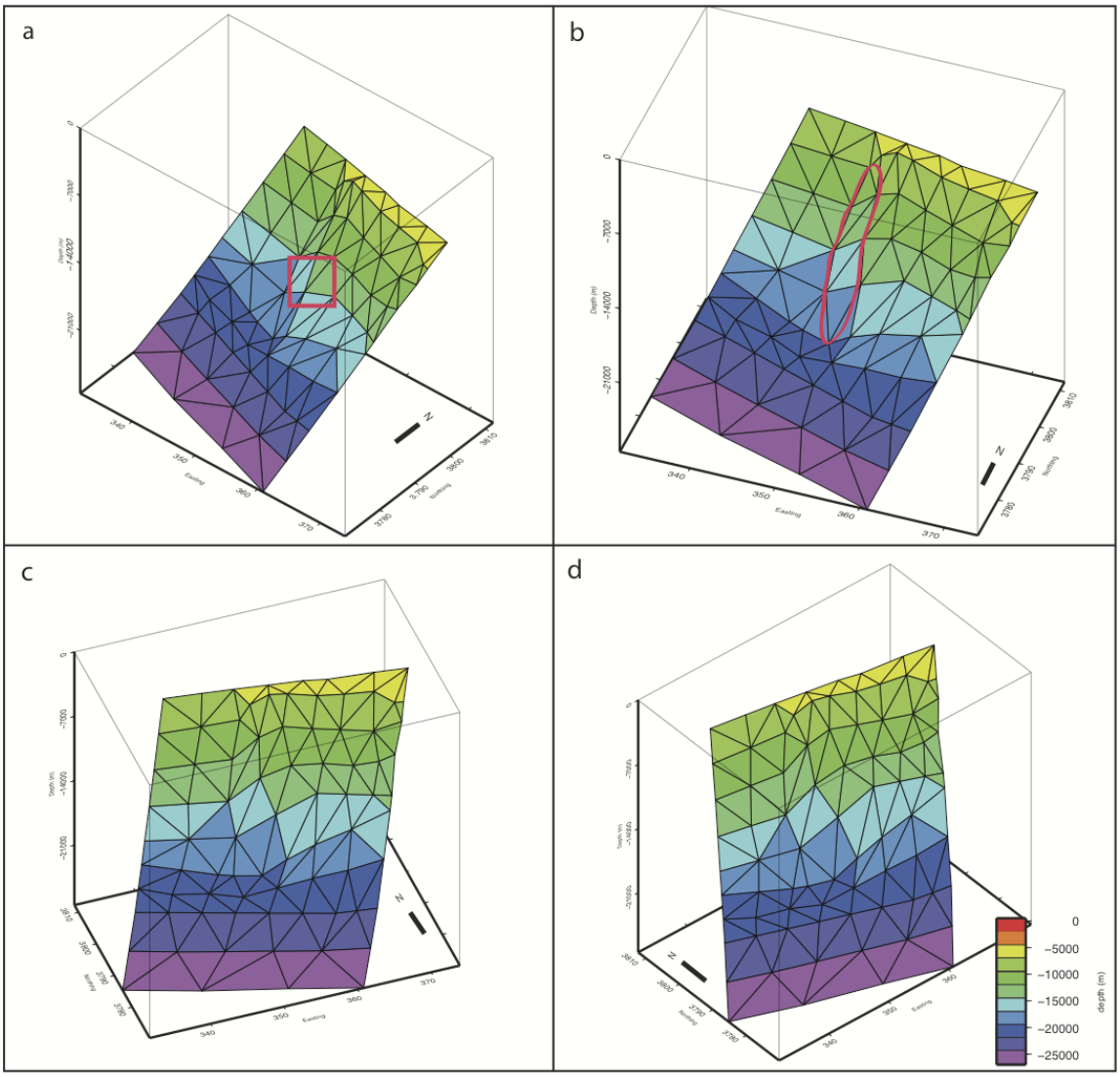

Figure 2.2 Our modified version of the Northridge CFM shaded by depth. We honor the overall raw CFM geometry, but have remeshed the surface to contain a more consistent and numerically-stable element size. The look directions are a) N40°W, red box denotes the protrusion on the fault, b) N20°W, red shape outlines the steep ramp west of the protrusion that connects to a planar extension to the west c) N20°E, d) N40°E. Axes in this study are in UTM km zone 11.

While the Northridge earthquake has been extensively studied, we now have the opportunity to synthesize much of the available information produced from studies of this earthquake, specifically the advances to community products produced by the Southern California Earthquake Center (e.g. Community Fault Model, Plesch et al., 2007; Community Velocity Model, Kohler et al., 2003) and improved geodetic inversion techniques. These advances will enable us to produce more accurate and robust results. Furthermore, many of the previous coseismic models utilized planar rectangular faults upon which to model slip (Shen et al., 1996; Hudnut et al., 1996; Wald et al., 1996), some of which modeled a uniform slip distribution (Massonnet et al., 1996; Murakami et al., 1996). Many of these studies have suggested that a complex fault geometry be used in order to better resolve the slip of the earthquake (Hauksson et al., 1995; Hudnut et al., 1996; Massonnet et al., 1996). Similarly, it has been previously shown that modeling on a geologically constrained non-planar fault can improve the fit to geodetic data (Maerten et al., 2005).

In this study, coseismic deformation for the Northridge earthquake is captured, for the first time, using the full array of available InSAR and GPS data (Hudnut et al., 1996; Figure 2.1), which will enable the calculation of a model that provides a fit to both the InSAR and GPS data. In order to infer slip on a realistic fault geometry, we use a modified version of the Southern California Earthquake Center (SCEC) Community Fault Model (Plesch, 2007; Figure 2.2), which will enable us to gain a better understanding of the interaction between fault geometry, slip distribution

and surface deformation. Furthermore, in order to accurately make future forecasts based upon static stress changes, an accurate slip model on accurate fault geometry is required. Using this updated model, the stress changes on neighboring faults due to the earthquake can be estimated. An example of the static stress change on the San Andreas fault due to the Northridge earthquake is shown in Appendix B. This is used to test the hypothesis by Savage and Svarc (2010) that static stress changes from the Northridge earthquake triggered right lateral slip at depth on the San Andreas fault.

2.2. Data

2.2.1 InSAR

We process two complementary pairs of SAR images spanning the Northridge earthquake – one pair from a descending orbital track from the European Space Agency (ESA) European Remote Sensing (ERS-1; Figure 2.3a) satellite and another from an ascending orbital track of the Japanese Aerospace Exploration Agency (JAXA) Japanese Earth Resources Satellite (JERS-1; Figure 2.3b). The details of the two image pairs are shown in Table 2.2. The data were processed into differential interferograms using the JPL/Caltech ROI_PAC software (Rosen et al., 2004). We remove the effects of topography by using an 80-meter resolution DEM from the NASA Shuttle Radar Topography Mission (Farr et al., 2007). The data are

unwrapped using the branch-cut method (Goldstein et al., 1988) implemented within ROI_PAC.

The ERS-1 and JERS-1 interferograms both show peak displacement of ~42 cm towards the satellite in the area of peak deformation. Since we have obtained data from both ascending and descending tracks, and each data set shows a significant range decrease in the epicentral region of the earthquake, we can infer that the direction of surface displacement due to the earthquake has a large uplift component. Both interferograms decorrelate in the San Gabriel mountains to the west of the peak deformation signal, which is most likely due to the dense vegetation and steep slopes that are found in this mountainous area. This is a known limitation of InSAR, especially for shorter wavelengths, such as the 5.6 cm C-band radar of ERS-1, for which incident radar wavefronts are sensitive to objects that are 10 mm or larger across, such as leaves, branches, bushes and the trunks of trees (Fielding, et al., 2005). The longer, L-band wavelength used by JERS-1 is correspondingly less sensitive to vegetation and slopes in general, however, the ~1400m baseline of the image pair that we use here is the probable reason for decorrelation in the JERS-1 interferogram.

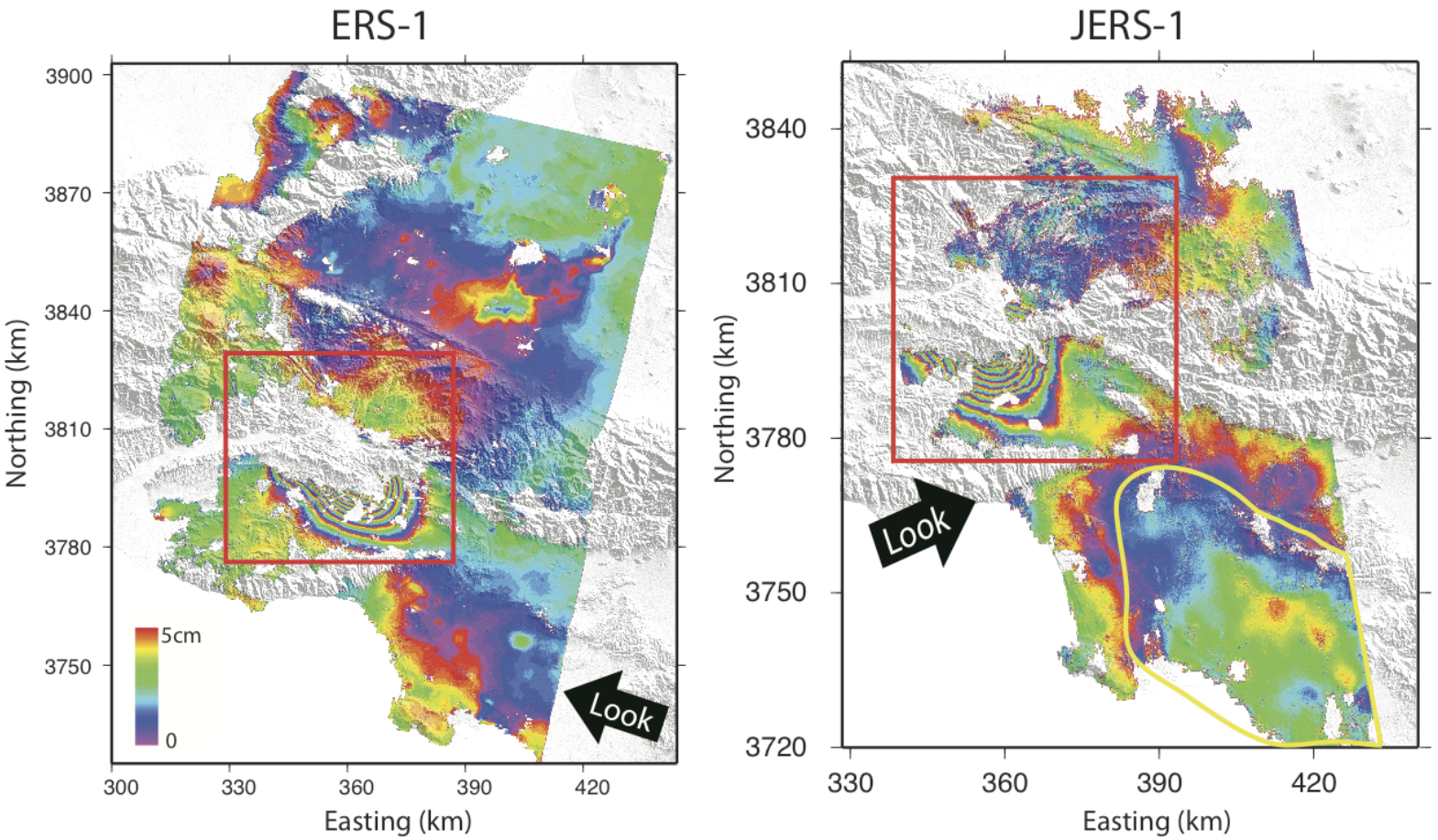

Figure 2.3 InSAR data used in this study. White areas represent areas that were not unwrapped. The red boxes indicate the areas shown in detail in modeling. Displacements are in the line of site direction where positive movements are towards the satellite. One fringe (a full sequence of violet through red) represents 5 cm of displacement. a) ERS-1 descending interferogram. b) JERS-1 ascending interferogram. Deformation from the Santa Ana Aquifer (southeast portion of the image; yellow polygon) is removed from out dataset due to anthropogenic motions, which have been shown to add amplitudes of up to 3mm/yr (Argus et al., 2005).

Satellite	ESA ERS1	JAXA JERS1
Track	442	535
Frames	2907-2925	243-244
Time span	2.08 years	1.02 years
Image 1 date	1993-11-08	1993-04-08
Image 2 date	1995-12-05	1994-07-14
Perpendicular baseline	40 m	1386 m
Incidence angle	23°, right-looking	35°, right-looking
Wavelength	5.6 cm (C-band)	23.5 cm (L-band)
Flight direction	Descending S14°W	Ascending N12°W

Table 2.2. Details of the SAR image pairs used in this study.

2.2.2 GPS data

We use the published GPS displacements of Hudnut et al. (1996) as additional constraints on the surface deformation (Figure 2.4). It is useful to have these additional, precise horizontal displacement measurements because InSAR is relatively insensitive to along track (north-south) horizontal motions. Since the Northridge thrust is a south-dipping fault, we would expect that the event produced shortening in the north-south direction, which can be observed from the GPS data. (We did not include the vertical component of the GPS data, as the precision in vertical direction is significantly lower than in the horizontal components, and because our InSAR data are sensitive to vertical displacements.) These GPS data show peak horizontal displacements of ~16 cm and 20 cm in the north and east directions, respectively. The data for the 66 sites were collected primarily in field campaign studies between October 1992 and February 1994 (Hudnut et al., 1996),

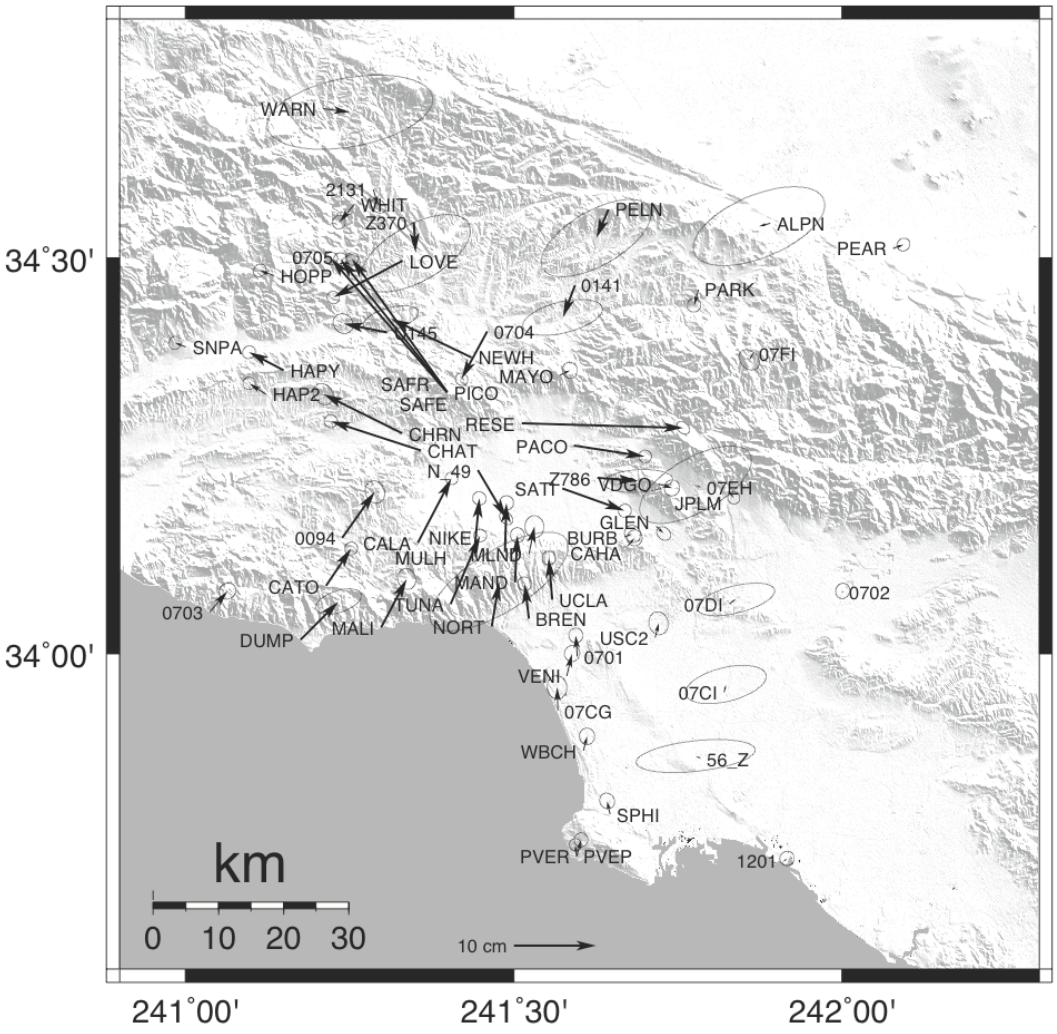

Figure 2.4 GPS data used in this study. Error ellipses represent 1 sigma uncertainties. Hudnut et al. (1996) provide tables and explanations of the data in greater detail.

as well as from continuous GPS observations from the Southern California Permanent GPS Geodetic Array (PGGA; Bock, 1993) and the Global Tracking Network managed by the International GPS Service for Geodynamics (IGS; Beutler and Brockmann, 1993). The data were obtained and processed by multiple organizations including UCLA, USGS, MIT, and JPL. Hudnut et al. (1996) compiled all

the available data and comment that some of the monuments may have shifted from strong ground motions during the earthquake due to their placement in soft sediments. Furthermore, some of these monuments had very few measurements taken from before and after the earthquake making the removal of interseismic deformation as well as the probability of relying on errors a concern in their accuracy.

2.3. Modeling the Northridge earthquake

2.3.1 Data post processing

As a first post-processing/pre-modeling step, we apply a curvature-based quadtree decomposition (e.g. Simons et al., 2002; Funning et al., 2007) to our unwrapped InSAR data in order to decrease the amount of data points and consequently increase the efficiency of our computations (Figure 2.5). This can be justified due to the high degree of spatial correlation of InSAR data (e.g. Hanssen, 2001). We can retain a similar level of independent information with significantly fewer data points. The effect of this sampling scheme is that the epicentral area, where most of the details of the surface deformation pattern are manifest, is sampled densely, while far field deformation is sampled less densely as few details of the earthquake are recorded there. This subsampling technique lowers the number of InSAR data points to be modeled from ~9 million to ~2500.

A visual examination of the JERS-1 interferogram shows that there are fringes detectable to the eye that are not unwrapped automatically during processing. These are digitized manually using GIS software – points along each half-fringe are manually picked, and the deformation values subsequently adjusted to agree with adjacent unwrapped data points – and included in our modeling (Figure 2.6). The digitized fringes show secondary uplift of ~40 cm measured towards the western area of deformation.

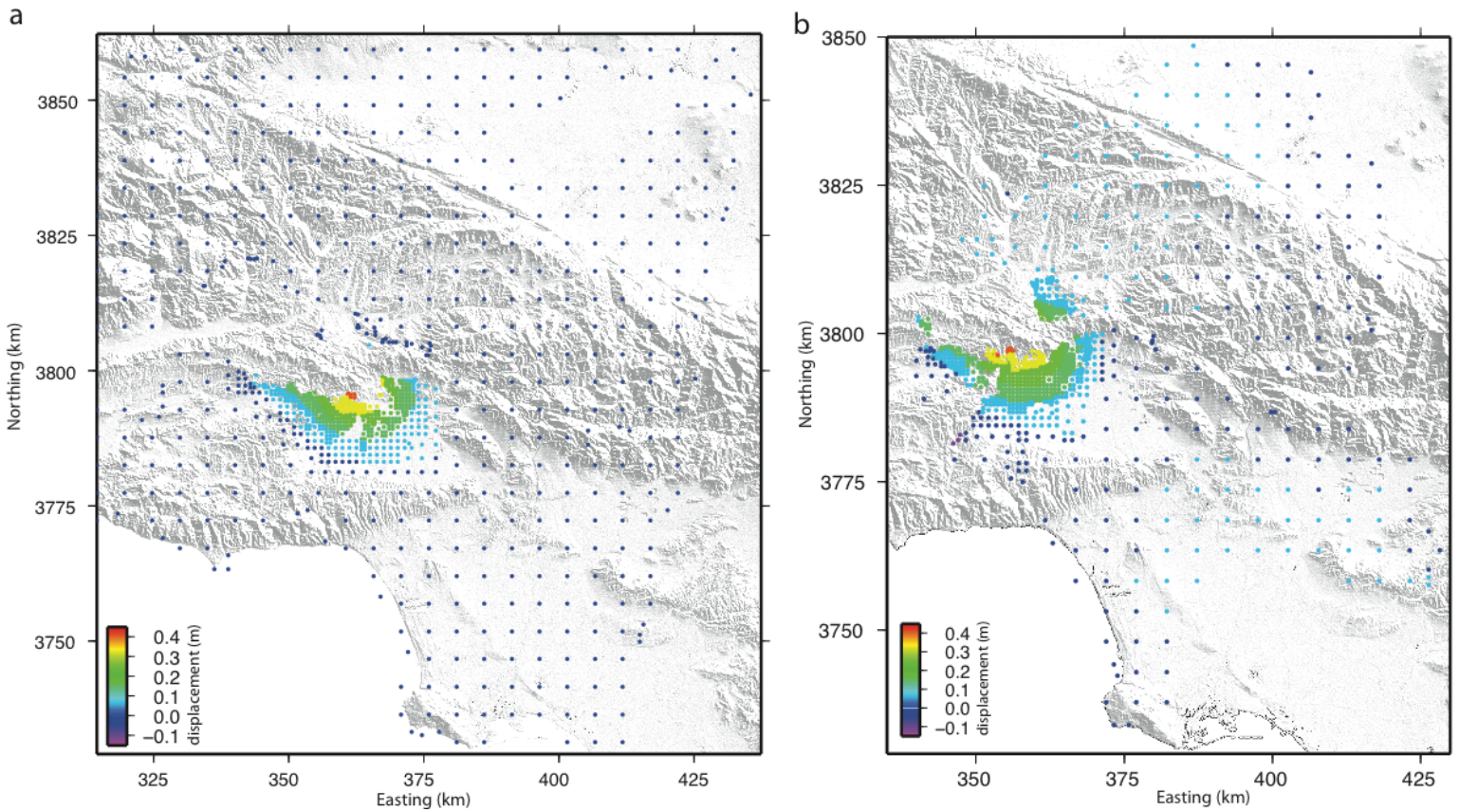

Figure 2.5 Quadtree decomposition of a) ERS-1 data b) JERS-data.

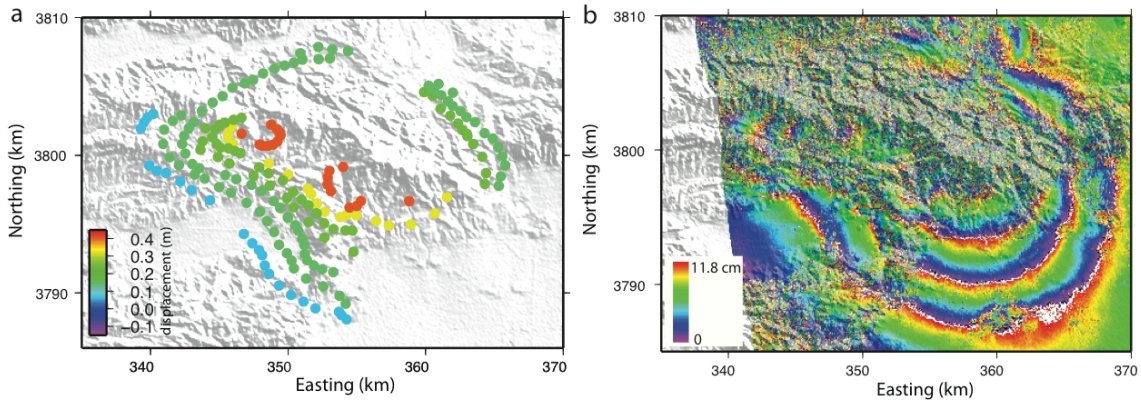

Figure 2.6 Fringes that are detectable by eye, but are not automatically unwrapped are digitized to include more data from the western region of the deformation pattern. a) Digitized data points. b) JERS-1 wrapped interferogram

2.3.2 The Community Fault Model

We model the distribution of slip on the Northridge thrust, in detail, using a modified version of its representation within the CFM as the fixed fault geometry. The CFM represents consensus fault geometries for the faults in southern California, determined using multiple data sources, including aftershock locations (e.g. Carena and Suppe, 2002; Shearer et al., 2005), geologic mapping (e.g. Yeats, 2004) and geophysical surveying (e.g. Bennett et al., 1996). The model of the Northridge thrust in the CFM was determined primarily by analyzing ~6,000 relocated aftershock hypocenters (Carena & Suppe, 2002). The Carena & Suppe (2002) contribution to the CFM extends to the western edge of the steep ramp on the fault (Figure 2b). To the west of this steep ramp, a planar extension based on the source model of the

Probabilistic Seismic Hazard Assessment for the State of California (PSHA; Peterson et al., 1996) is added to the fault by Plesch et al., (2007).

While the Northridge CFM contains over 4,800 elements, our simplified version of the CFM Northridge thrust has been subsampled and remeshed in order to make computations more efficient and obtain a more uniform element size. Our modified model consists of 132 planar triangular elements that are tessellated into a non-planar surface (Marshall et al., 2008). We can justify this reduction of model complexity given the likely degradation of the resolving power of our data with depth (e.g. Harris and Segall, 1987), and the computational penalty associated with estimation of large numbers of model parameters.

2.3.3 Single fault rectangular dislocation inversion

We first invert for a fault solution to determine a simple fault geometry for the Northridge event (Figure 2.7) assuming the fault can be represented as a rectangular dislocation in an elastic half space with uniform slip (e.g. Okada, 1985). We start by inverting for a single fault solution non-linearly using the okinv code (Clarke et al., 1997; Wright et al., 1999), which estimates the global minimum misfit solution of such a rectangular dislocation using a downhill Powell algorithm with 100 Monte Carlo restarts. We solve for 9 fault parameters – strike, dip, slip, rake, fault length, top fault depth, bottom fault depth and x and y location of the center of

the fault projected up-dip to the surface. Approximate, bounded values of these parameters are set a priori by interpreting observations of the deformation pattern and the results of previous authors. The parameter bounds are set wide at first and narrowed as the inversion converges on a global minimum misfit solution. We additionally solve for nuisance parameters for each dataset including translations (for both InSAR and GPS) and gradients (InSAR) in both the x and y direction. The resulting model produces a fault patch with slip of 2.2 m of slip, a moment of M_0=1.17 x 10^{19}Nm ($M_w \approx 6.65$) with a weighted residual sum of squares (WRSS) of 5.07 m^2, defined as

$$WRSS = \sum_{i}^{n} w_i (obs_i - calc_i)^2 \tag{2.1}$$

where *w* is the weight of the *i*th data point *obs* is the observed *i*th data point with ramps and offsets subtracted from the data points and *calc* is the predicted displacement of the *i*th data point.

The best-fitting fault parameters are shown in Table 2.3 and are within the range of previous source solutions (Table 2.1). The single fault inversion leaves residual deformation of ~8-10 cm to the western area of deformation as seen from the ERS-1 and GPS residuals (Figure 2.7b and d). Similar residual deformation was observed in previous studies of the Northridge earthquake when only a single planar dislocation

was modeled (Massonnet et al., 1996; Shen et al., 1996; Donnellan and Lyzenga, 1998). This residual deformation suggests that another fault may have ruptured in the earthquake, or that the fault is a non-planar structure. To account for this, we repeat our modeling, adding another fault is added to the west of the main fault. identified here.

Fault parameter	**Single fault dislocation**
Strike	114.5° ± 1.9°
Dip	39.6° ± .9°
Rake	86.2° ± 1.8°
Slip	2.2 m ± .07 m
Length	16.1 km ± .2 km
Top depth	7.8 km ± .3 km
Bottom depth	16.0 km ± .1 km
X position of fault projection (UTM zone 11)	364.111 km ± .5 km
Y position of fault projection (UTM zone 11)	3808.698 km ± .3 km

Table 2.3 Fault parameters of our single fault rectangular dislocation inversion with 1 sigma uncertainties. Uncertainties in our model parameters are estimated using a bootstrap test where 100 perturbed data sets are produced and each is inverted in okinv (See supplemental materials section S2 for details).

2.3.4 Two fault rectangular dislocation inversion

Our two-fault model is solved for in a similar same way to our single fault model. We use an iterative approach, however, solving for each fault individually while keeping the other fixed in order to avoid large tradeoffs between the two faults, which prevented convergence to the global minimum and thus results in a higher misfit to the data. (Figure 2.8; Table 2.4). Our best fitting model has two south-dipping faults;

a main fault, which has a 4 km shorter length than the fault in our single fault model, with 2.3 m of slip, and a smaller secondary fault to the west and updip of the main fault with 0.79 m of slip. The model produces a combined moment of M_0=1.29 x 10^{19} Nm (M_w=6.68) with a WRSS of 3.36 m^2; a 33% reduction in WRSS over the single fault model. We also tested models where the bounds were chosen such that the secondary fault dipped to the north, consistent with backthrusting as suggested by other authors (Shen et al., 1996; Massonnet et al., 1996). We found that these models had a significantly poorer fit to the data, with a WRSS of 4.63 m^2 in the best-fitting model. In every model, residual deformation to the western edge of the deformation zone persists. Our best-fitting model, however, reduces the residual deformation in the west to ~5 cm in the ERS-1 residual, as well as dramatically reducing the misfit in the GPS data to within the uncertainties. (Figure 2.8b and d). Our best-fitting two-fault model is not as well resolved as the one fault model, evidenced by the larger uncertainties, most notably in the slip of the secondary fault.

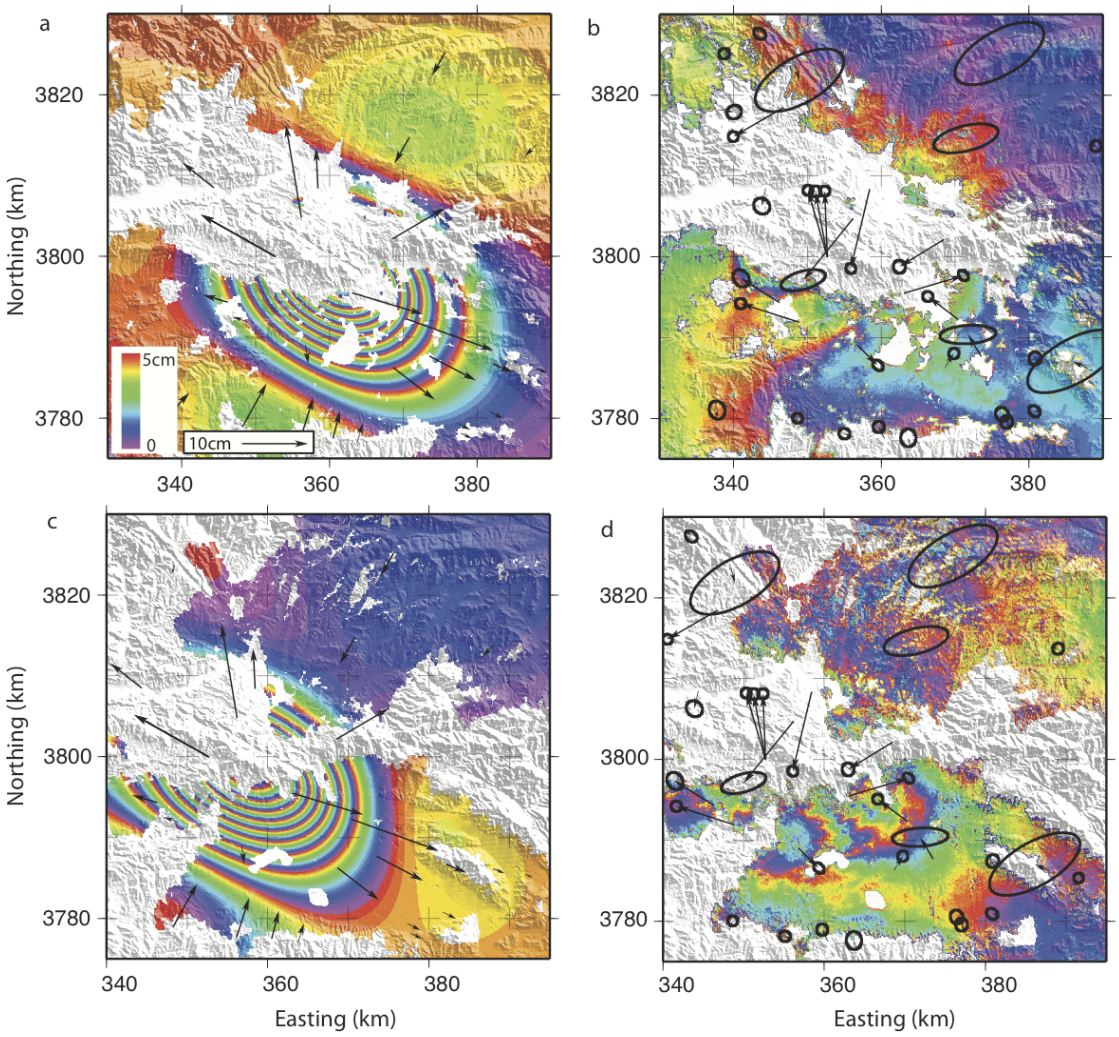

Figure 2.7 Results of our best-fitting single fault dislocation. One fringe is equal to 5cm of deformation in the InSAR images. GPS vectors are overlaid onto the InSAR images with 1 sigma uncertainties on the residual plots. a) Model as seen from the ERS-1 viewing geometry b) ERS-1 residuals. c) Model as seen from the JERS-1 viewing geometry. d) JERS-1 residuals.

Fault Parameter	Main fault	Secondary fault
Strike	105.1° ± 3.8°	132.4° ± 5.5°
Dip	40.7° ± 1.5°	47.0° ± 3.7°
Rake	80.5° ± 2.3°	132.0° ± 7.3°
Slip	2.32 m ± 1.5 m	0.79 m ± 2.0 m
Length	11.9 km ± 1.1 km	10.8 km ± 0.7 km
Top depth	7.3 km ± 0.6 km	1.7 km ± 1.7 km
Bottom depth	16.2 km ± 0.2 km	6.2 km ± 1.7 km
X position of fault projection (UTM zone 11)	362.457 km ± 1.1 km	352.450 km ± 0.7 km
Y position of fault projection (UTM zone 11)	3808.589 km ± 0.6 km	3802.416 km ± 2.0 km

Table 2.4 Fault parameters for our best-fitting two-fault rectangular dislocation model with 1 sigma uncertainties, which are determined from a bootstrap test explained in section S2.

2.3.5 Variable slip inversion with the CFM.

In the uniform slip models, the fault could change orientation and location freely. We now use the CFM as a fixed fault reference to observe whether or not this non-planar fault can model the deformation pattern. Since for a fixed fault geometry the relationship between fault slip (in both the strike-slip and dip-slip components) and surface displacement is linear, we use our simplified version of the Northridge CFM to model for a variable slip and rake distribution on the Northridge fault. We use the poly3d code (Thomas, 1993), which calculates displacements, strains and stresses in an elastic half-space or whole-space by using planar polygons, which when placed together, may form non-planar surfaces. In this case, we use poly3d to calculate Green's functions (e.g. Bürgmann et al., 2005) to be used with the slipinv code

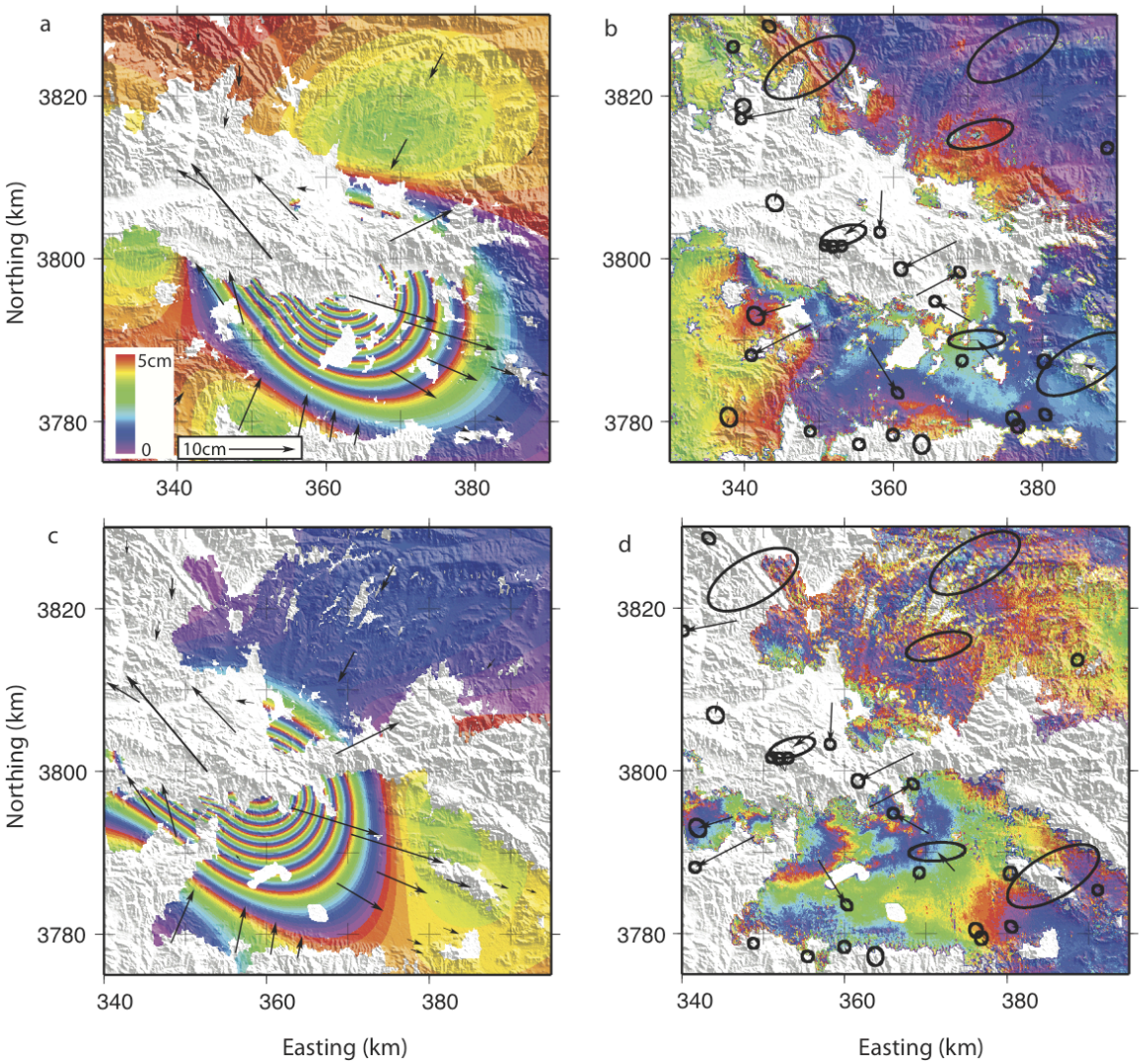

Figure 2.8 Results of our best-fitting 2 fault dislocation model. One fringe is equal to 5cm of deformation in the InSAR images. GPS vectors are overlaid onto the InSAR plots with 1 sigma uncertainties on the residual plots. a) Model as seen from the ERS-1 viewing geometry b) ERS-1 residuals. c) Model as seen from the JERS-1 viewing geometry. d) JERS-1 residuals.

(Funning et al., 2005; for model details see section S4) to invert for the distribution of slip. We apply several constraints to our model: (i) a positivity constraint to prevent retrograde slip, implemented by inverting using the Fast Non-Negative Least Squares algorithm (Bro and De Jong, 1997); (ii) Laplacian smoothing, used to

prevent unphysical oscillatory slip, with the weight applied to smoothing in the inversion chosen by selecting the optimal tradeoff between slip roughness and WRSS (e.g. Du et al., 1992; Jonsson et al., 2002; Figure A4a); (iii) a rake constraint, implemented through our choice of basis functions for slip, the range of permitted rakes for each patch being constrained between 45° and 135° (i.e. 45° either side of pure reverse slip; Figure A4b). Additionally, we weight the data by the inverse of their covariances: InSAR covariances are estimated using the autocorrelation of an undeformed portion of each interferogram (e.g. Wright et al., 2003); for the GPS data we use the variances in both horizontal components, plus the covariance between them as estimated during data processing (Hudnut et al., 1996).

The results show a main asperity with slip peaking at ~2.5 m with a rake of ~82° at a depth of ~14 km in the central portion of the fault. The largest portion of slip (42% of the total moment) occurs on the peak of the protrusion within the Northridge CFM, with ~0.8 m of slip (14% of the total moment) present to the northwest with slip down to ~11 km. We calculate little slip towards the top of the fault as this is a blind thrust fault and the surface projection of the fault must have zero slip by definition. This model has a moment release of M_0=1.47 ×10^{19} Nm (M_w 6.75; Figure 2.9a) which is higher than previous models, suggesting we are modeling some postseismic motions that are likely contained within the data. Residual deformation to the western edge of the deformation pattern in the ERS-1 data is nearly eliminated with less than 2.5cm of residual deformation (Figure 2.9c).

However, the GPS data contain residuals of ~8 cm in the area where the InSAR data decorrelate (Figure 2.9 c and e). As mentioned above, it has been noted that there are disagreements between the InSAR and GPS data for this event (eg. Massonnet et al., 1996; Murakami et al., 1996), however, the GPS displacements in this model fit nearly as well as a GPS-only derived model (Figure A5). We find, as in previous studies, that the GPS data predict surface displacements larger than are observed in the InSAR data. This model has a better overall fit to the data, as indicated by a WRSS of 2.02m^2. Individual dataset model contributions and uncertainty and resolution calculations are shown in Appendix A.

2.4. Discussion

2.4.1 Postseismic deformation

Since much of our data was captured long after the event (i.e. the post earthquake SAR images were acquired 6 months to ~2 years after the earthquake), there will most likely be a postseismic signal within our data. Furthermore, it has been suggested that the postseismic process from the Northridge event was completed within 100 days (Savage and Svarc, 2010), which means the entirety of the postseismic processes could be contained within our InSAR data. Donnellan and Lyzenga (1998) used GPS to measure postseismic movements from the earthquake and concluded the postseismic process was dominated by shallow afterslip with

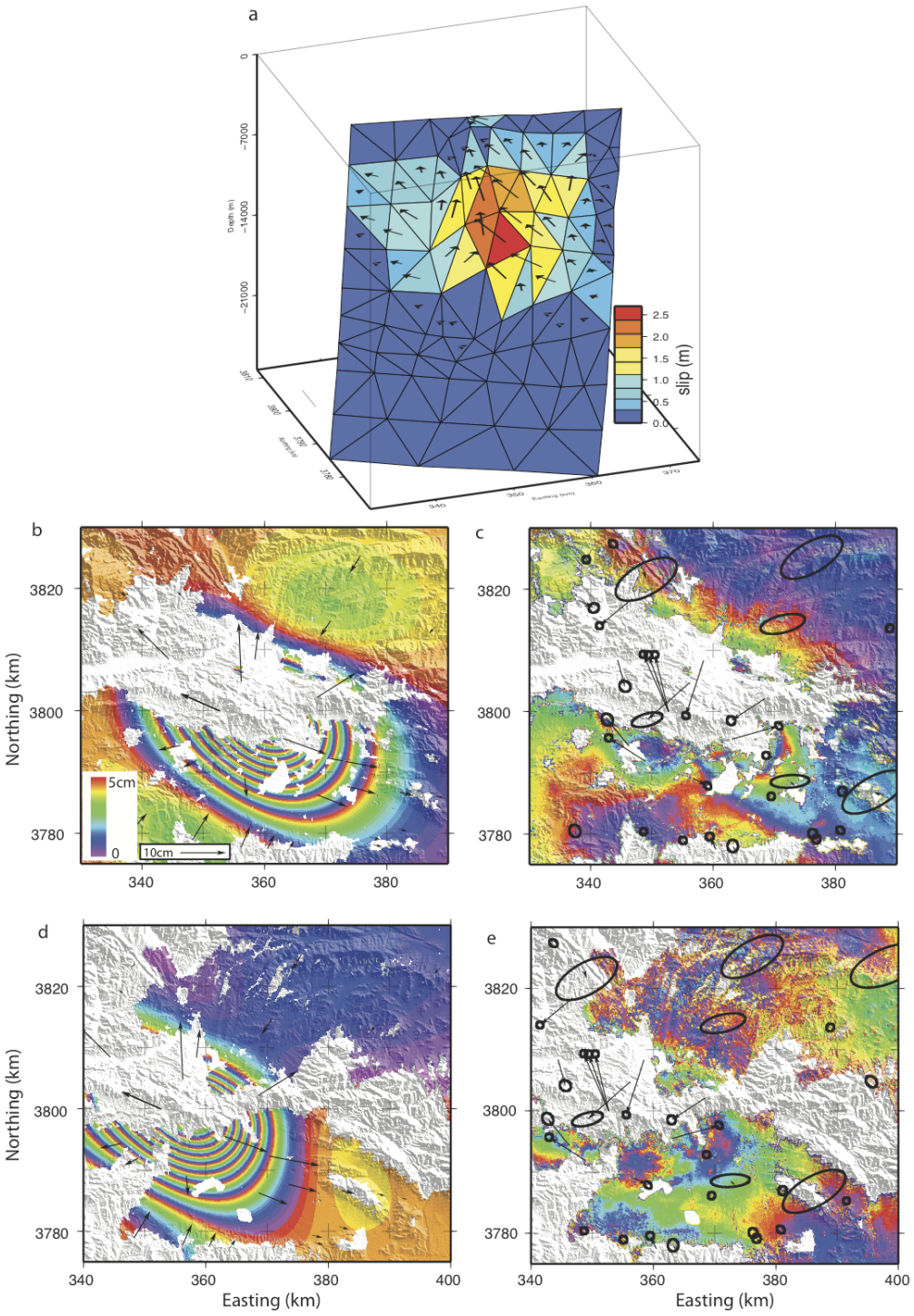

Figure 2.9 Results of our variable slip CFM model. a) Slip model. Slip peaks at the protrusion on the Northridge thrust. b) Model as seen from the ERS-1 viewing geometry c) ERS-1 residuals. d) Model as seen from the JERS-1 viewing geometry. e) JERS-1 residuals.

peak uplift of ~12 cm. They modeled postseismic deformation using two faults, one on the main fault indicating fault afterslip and another shallow fault to the west, similar to, but larger than, the secondary fault in our two-fault model. They conclude that broad shallow deformation occurred to the west. They find that the uplift in the western area of deformation is narrower and higher than the afterslip model suggests.

It appears that postseismic deformation manifests itself in our InSAR data to the west and southeast of the deformation pattern, which can be seen by the residual deformation of our preferred slip solution (Figure 2.9c and e). Our model shows some of the deformation to the west as observed by Donnellan and Lyzenga (1998), and it appears likely that the secondary fault in our two-fault dislocation model is attempting to reproduce this shallow deformation. This movement is not likely due to aftershock deformation, which has been previously suggested (Massonnet et al., 1996), as Donnellan and Lyzenga (1998) found that aftershocks could represent only ~10% of postseismic motions based upon their cumulative moments. Furthermore the large aftershocks ($M_L > 5$; Hauksson et al., 1995) near the western edge of deformation are quite deep (i.e. 12-15 km), meaning they most likely would not produce a significant suface deformation signal. While some of the deformation in this area is most likely postseismic deformation, the ~40 cm signal appears to be too large to be attributed solely to postseismic motions. Instead, the large narrow displacements in the western region, leaves reason to believe that the deformation

in this area can be explained by movements associated with a combination of both coseismic, and shallow postseismic deformation.

2.4.2 Verification of the Community Fault Model

Our best-fitting rectangular dislocation model is shown against the best-fitting solution with the CFM (Figure 2.10). Our CFM model places slip on a main asperity on the peak of the protrusion on the Northridge fault, with secondary slip to the northwest. Our two-fault dislocation model follows this same general slip pattern; however, the region of secondary slip is shallower and south in the two-fault dislocation model, though our secondary fault in this model is not as precise. This, as well as observations of a narrow deformation pattern in the west (JERS-1 fringes; Figure 2.6) suggest slip at a shallower depth towards the west than the slip in our CFM model. Slip is prevented from moving updip in our CFM model, as placing slip updip causes the modeled deformation to be localized north of the observed signal. Furthermore, the slip patch in the two-fault uniform slip model is ~3 km south of the CFM meaning, this slip most likely occurs on a different fault.

The majority of slip occurs on the portion of the fault determined by the aftershock relocation and fault geometry study of Carena and Suppe (2002), which appears to fit the data well. As noted, the western planar extension is based on the source geometry used in the PSHA for the Northridge fault (Peterson et al., 1996), in which

the planarity of the fault shows a lack of detailed model constraints for the CFM (A. Plesch, 2012; personal communication). In order to better fit the data, the planar western extension of the CFM should not be as far north as it is in the CFM. If the western extension were moved south, slip would be allowed to move farther updip, which would better fit the deformation pattern. The deformation to the west, however, could be slip on a separate fault, although this requires further testing.

The depth positioning of our two models is also inconsistent, with the best-fitting rectangular dislocation model placing the faults ~2 km above the Northridge CFM (Figure 2.10b). This discrepancy can be seen in the surface deformation residuals of our preferred model to the north of the deformation pattern (Figure 2.9c) with ~3 cm of residual deformation present. There are several possible explanations for this difference: (i) the Northridge CFM could be slightly misplaced; (ii) the velocity structure of the region could be skewed causing the relocated aftershocks of Carena and Suppe (2002) to be misplaced; (iii) postseismic displacements could cause the best-fitting dislocation to be modeled at a shallower depth than should be expected (Donnellan and Lyzenga, 1998); (iv) inverting for slip assuming a homogenous elastic medium instead of using a layered elastic model where strength decreases towards the surface causes shallower slip. It is most likely that the discrepancy in depth is related to (iv) as it has been suggested that models determined assuming a homogeneous elastic halfspace may model slip at a shallower depth than those using layered earth models (Feigl, 2002; Hearn and Bürgmann, 2005; Weston et al.,

2012). Other previous coseismic geodetic slip models placed the fault above the aftershock distribution as well (Hudnut et al., 1996 Shen et al., 1996) and explained the discrepancy by criticizing the assumption of uniform elasticity. To test this, we use a two layer elastic structure determined from the Community Velocity Model (Kohler et al., 2003) to calculate a variable slip distribution on a planar fault using the geometry from our single-fault rectangular dislocation model (Figure A11). Slip moves downdip for the layered elastic case relative to the uniform elastic model, but the difference is less than 1 km.

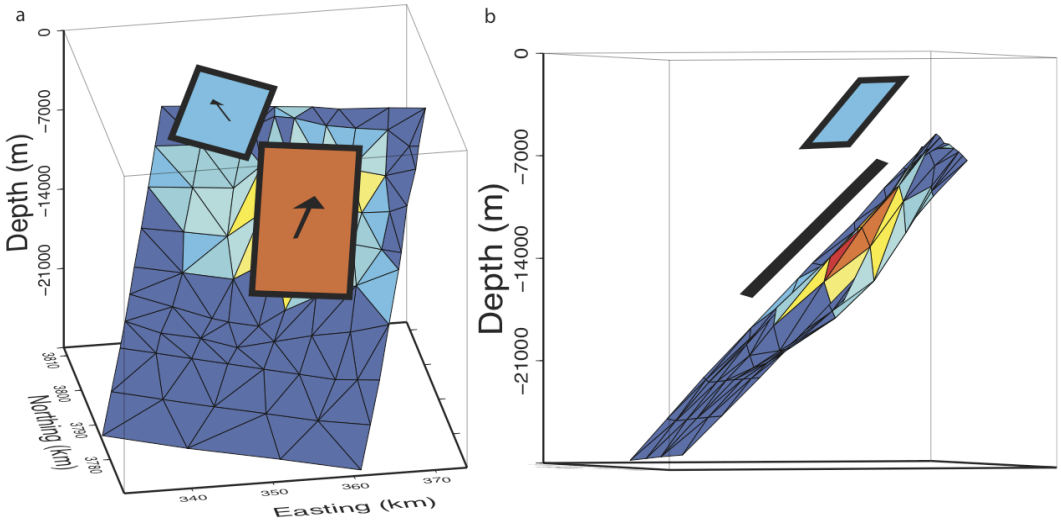

Figure 2.10. The best-fitting rectangular dislocation plotted against the Northridge CFM. a) Both models show a main asperity with secondary shallower slip to the west. The two-fault dislocation model places slip at a shallower depth than the CFM. b) A side view of our best-fitting rectangular dislocation plotted on the CFM. Slip on the main asperity is ~2km shallower than the CFM which is most likely due to the assumption of uniform elasticity in our model.

2.4.3 The effect of fault geometry on slip and rake

The Northridge CFM geometry contains several complexities (Figure 2.2), notably a large along-strike ramp sloping from east to west towards the middle of the fault on which there is a large protrusion, east of a steep ramp. It has been proposed that irregularities in fault geometry may significantly alter slip across a fault surface by acting as asperities or barriers (Resor and Meer 2009; Marshall and Morris, 2012). The slip pattern of our preferred model supports this, as it shows slip on a main asperity at the peak of the protrusion on the fault with slip decreasing towards the bottom of the steep ramp to the west (For more details see Figure A10).

Our results also show an alternation in rake across the strike direction of the fault, alternating ~10° of pure thrust (Figure 2.9; Figure A10). Marshall and Morris (2012) showed that these alternating bands are indicative of oblique loading on corrugated or wavy dip-slip faults. While the sense of slip in our preferred model is primarily thrust, this rake alternation suggests that the direction of loading stresses may not necessarily be parallel to the up-dip direction. Instead, this alludes to the possibility that loading may have an oblique orientation; however, the non-planar topology of the fault prevents the fault from slipping obliquely as a whole.

2.5. Conclusions

Using multiple forms of geodetic data, we model the coseismic slip of the 1994 Northridge earthquake using rectangular dislocations and a modified version of the SCEC Northridge CFM as a fixed fault reference. Our single fault rectangular dislocation model is well resolved and fits within the range of solutions determined by previous studies. Our two-fault model provides a better fit, although its model parameter estimates are not as precise. The two-fault model as well as the variable slip CFM model, place the majority of slip on a main asperity with secondary slip to the west; however, the two-fault dislocation model places slip at a shallower depth than the CFM reaches, and in a different location. This discrepancy can be attributed to a combination of coseismic and postseismic motions towards the west of the deformation pattern and to poor constraints of the western portion of the CFM as it is a planar extension to the fault contribution by Carena and Suppe (2002).

Chapter 3 Synthesis

3.1 Source modeling

This thesis has focused on the source modeling of earthquakes using various geodetic measurements. Modeling the source parameters and slip of earthquakes is important because it leads to an understanding of the earthquake process and how slip occurs on faults in various situations. Also, by modeling the slip pattern of an earthquake, calculations may be made to model the stress changes on other faults in the area surrounding the earthquake. Such measurement will allow scientists to better forecast the possibility of future earthquakes due to an earthquake event in the immediate area. Appendix B shows such an example on the San Andreas fault. Static stress changes on the San Andreas fault due to the Northridge earthquake are calculated by Dr. Scott Marshall and Julia Irizarry of Appalachian State University. This model is then used to test the hypothesis of Savage and Svarc (2010) that the Northridge earthquake triggered deep right lateral slip on the San Andreas fault.

3.2 Future directions for the Northridge earthquake

3.2.1 GPS data

The quality of the GPS data used in the Northridge study is suspect as the measurements were taken, and the data processed, in the early days of using GPS for scientific research. Some of the sites have only one measurement before the earthquake, meaning the data may be contaminated with errors if the site was inaccurately measured initially. Some of the GPS monuments may have also shifted in the soft sediments and strong shaking of the earthquake. Furthermore, interseismic deformation has not been removed, and non-tectonic signals such as aquifer extraction or recharge could not be fully removed.

Due to poor quality of some of the GPS data, a cause could be made for removing some sites. This needs to be done systematically to be sure that the data are removed for scientific reasons and not necessarily because a certain data point did not fit the model. By using a detailed list of the substrate beneath each site, the number of measurements accomplished as well as the date of each measurement, a procedure for removing poor quality GPS measurements may be developed.

3.2.2 The Community Fault Model

As noted, the Community Fault Model is poorly constrained to the west (A. Plesch, 2012; personal communication) with a planar extension making up the western portion of the fault. Future work for this model may involve changing the geometry of the western planar extension in order to suggest a better-fitting fault geometry. A fault segment can also be added to the CFM similar to the secondary fault in the two-fault model to model the shallow postseismic deformation.

3.3 The future of InSAR

3.3.1 SAR imaging platforms

With the recent failure of Envisat, the immediate future for InSAR appears bleak, as the TerraSAR-X Cosmo-SkyMed and Radarsat satellites are the only SAR satellites in operation. The organizations operating these satellites, however, are restrictive in their data policies, which make their data expensive and difficult to obtain. Furthermore, these are X-band satellites which means they have ~3 cm wavelength radar antennas. X-band provides higher resolution and measurement precision, however decorrelation is a large issue with the smaller wavelength satellites as explained above (Section 1.2). Commercial satellites such as Radarsat are operating as well, although the data are costly to obtain. The anticipated May 2013 launch of

the first Sentinel-1 SAR satellite, operated by ESA, will provide continuously acquired and freely-available data for observations of the Earth's surface. These satellites are being launched under the Global Monitoring for Environment and Security (GMES) program, which is a European initiative proposed in 1998, dedicated to services that will aid in land, ocean and atmospheric monitoring as well as emergency response and security. The Sentinel family of satellites (a second satellite is planned for launch in 2015) will form the backbone of InSAR-based research in the short-to-medium term.

NASA/JPL have also proposed the launch of a satellite with L-Band SAR capabilities, which is advantageous for earthquake studies, as L-band SAR pairs decorrelate less in vegetated mountainous regions than does the shorter wavelength C-band radar pairs. The Deformation, Ecosystem Structure and Dynamics of Ice (DESDynI) mission objectives are to image the Earth in order to anticipate the likelihood or earthquakes, landslides and volcanic eruptions. The anticipated launch of DESDynI is scheduled for 2021, however, since project approval has been delayed multiple times, this launch date remains doubtful.

Uninhabited Aerial Vehicle Synthetic Aperture Radar (UAVSAR) also presents new advances to the study of surface deformation using InSAR (Rosen et al., 2006). Using this technique, a SAR antenna is mounted on an unmanned aircraft and flown over the target. This allows SAR data to be acquired on short notice, which makes

UAVSAR a useful tool to provide data to emergency personel shortly after a disaster. As long as there exists archived SAR images of an earthquake prone region before an earthquake strikes, the UAV may be deployed shortly after the event to assess surface deformation quickly. By the time the UAV lands, an image of the deformation pattern can already have been processed, which will notify emergency responders as to where the greatest amount of damages are likely to have occurred. While useful for rapid response, UAVSAR is constrained by the location of airstrips for long flights. Furthermore, the position control of an aircraft is more difficult than that of a satellite as wind currents may change the course of the airplane, however, this may be corrected in processing. Currently, NASA operates what is called UAVSAR, however it is on a manned Gulfstream III jet. Future improvements to the system will most likely place a SAR antenna on a drone aircraft.

If enough SAR data can be acquired globally and at short temporal timescales, scientists will be able to map strain accumulations across the Earth. With enough continuous data it has been suggested that short to medium-term earthquake forecasts may be plausible with the use of InSAR (Wright, 2002) as we can infer stress changes from strain accumulation. Areas in which strain is accumulating are more likely to have increasing stresses, which increase the likelihood of an earthquake.

3.3.2 InSAR modeling

Recently, tests have been conducted in automating the earthquake modeling process using neural networks (Stramondo et al., 2011), in which a computer is trained to recognize patterns similar to the human brain. These networks are trained using multiple synthetic interferograms, many similar to those shown above, which are useful as they give a simpler view of the relationship between fault geometry and deformation. Furthermore, the parameters are known and represent a unique, known solution. Two exercises are performed with this technique: the first identifies the mechanism of the earthquake, while the second inverts for fault geometry. Tests classifying synthetic interferograms similar to the examples above, prove to be successful, although real interferograms are much more difficult to compute in that they contain decorrelation and noise. Stramondo et al. (2011) were, however, able to model earthquakes within the range of previously estimated solutions. Future testing will include the addition of GPS and variable slip models, which will enable an automated modeling solution similar to the Global Centroid Moment Tensor. These networks may also be trained to look into the SAR data archives to model preseismic strain accumulations for short term forecasting.

References

Argus, D. F., M Heflin, G. Peltzer, F. Crampe,. (2005). Interseismic strain accumulation and anthropogenic motion in metropolitan Los Angeles, *Journal of Geophysical Research* **110.**

Atzori, S., C. Tolomei, S. Salvi, S. Zoffoli. (2011). Co-seismic ground displacement and preliminary source models for the 10/23/2011, Mw 7.2, Van earthquake, Eastern Turkey. http://www.supersites.org.

Bennett, R.A., W.R. Rodi, E. Reilinger. (1996). Global positioning system constraints on fault slip rates in Southern California and northern Baja, Mexico, *Journal of Geophysical Research* **101,** 21943-21960.

Beutler, G. and E. Brockmann (Editors) (1993). Proc. of the 1993 IGS Workshop, International Association of Geodesy, Druckerei der Universitat Bern.

Bock, Y., J. Zhang, P. Fang, J. Genrich, K. Stark, S. Wdowinski (1993). One year of daily satellite orbit and polar motion estimation for near real-time crustal deformation monitoring, in Developments in Astrometry and Their Impact on Astrophysics and Geodynamics, Kluwer Academic Publishers, Hingham, Massachusetts, 279-284.

Bro, R., S.D. Jong. (1997). A fast non-negativity-constrained least squares algorithm, *Journal of Chemometrics* **11,** 393-401.

Bürgmann, R. G. Kogan, G. Steblov, G. Hilley, V. Levin, E. Apel. (2005). Interseismic coupling and asperity distribution along the Kamchatka subduction zone, *Journal of Geophysical Research* **110,** B07405.

Bürgmann R., P. Rosen, E. Fielding. (2000). Synthetic Aperture Radar Interferometry to Measure Earth's Surface Topography and It's Deformation, *Annual Review Earth Planet Science* **28,** 169-209.

Carena, S., Suppe, J. (2002). Three-dimensional imaging of active structures using earthquake aftershocks: The Northridge thrust, California, *Journal of Structural Geology* **,** 887-904.

Clarke, P., D. Paradissis, P. Briole, P.C. England, B.E. Parsons, H. Billiris, G. Veis, J.C. Ruegg. (1997). Geodetic investigation of the 13 May 1995 Kozani-Grevena (Greece) earthquake, *Geophysical Research Letters* **24,** 707-710.

Davis, T. L., J.S.Namson. (1994). A balanced cross-section of the 1994 Northridge earthquake, southern California, *Letters to Nature* **372,** 167-169.

Dolan, J., K. Sieh, T Rockwell, R. Yeats, J. Shaw, J. Suppe, G. Huftile, E. Gath. (1995). Prospects for larger or more frequent earthquakes in the Los Angeles metropolitan region, *Science* **267,** 199-205.

Donnellan, A., G. Lyzenga. (1998). GPS observations of fault afterslip and upper crustal deformation following the Northridge earthquake, *Journal of Geophysical Research* **103,** 21,285-21,297.

Du, Y., A. Aydin, P. Segall. (1992). Comparison of various inversion techniques as applied to the determination of a geophysical deformation model for the 1983 Borah Peak earthquake, *Bulletin of the Seismological Society of America* **82,** 1840-1866.

Farr, Tom, P. Rosen, E. Caro, R. Crippen, R. Duren, S. Hensley, M. Kobrick, M. Paller, E. Rodriguez, L. Roth, D. Seal, S. Shaffer, J. Shimada, J. Umland, M. Werner, M. Oskin, D. Burbank, D. Alsdorf. (2007). The shuttle radar topography mission, *Reviews of Geophysics* **45,** .

Feigl, K.L., (2002). Estimating earthquake source parameters from geodetic measurements. International Handbook of Earthquake and Engineering Seismology 81A, 1–14.

Fialko, Y., D. Sandwell, D. Agnew, M. Simons, P. M. Shearer, and B. Minster (2002), Deformation on nearby faults induced by the 1999 Hector Mine earthquake, *Science*, *297*.

Fielding, E., M. Talebian, P. Rosen, H. Nazari, J. Jackson, M. Ghorashi. (2005). Surface ruptures and building damage of the 2003 Bam, Iran, earthquake mapped by satellite synthetic aperture radar interferometric correlation, *Journal of Geophysical Research* **110,** B03302.

Fielding, E., J. Polet, P.R. Lundgren, .H. Yun, M. Motagh, S.E. Owen, M. Simons. (2012). Finite fault slip evolution model for the 23 october 2011 Mw 7.1 Van, Turkey earthquake from geodetic and seismic waveform analysis. Seismological Society of America annual conference.

Funning, G., B. Parsons, T. Wright. (2005). Surface displacements and source parameters of the 2003 Bam (Iran) earthquake from Envisat advanced synthetic aperture radar imagery, *Journal of Geophysical Research* **110,** B09406.

Funning, G., B. Parsons, T. Wright. (2007). Fault slip in the 1997 Manyi, Tibet earthquake from linear elastic modelling of InSAR displacements, *Geophysical Journal International* **169,** 988-1008.

Goldstein, R.M., H.A. Zebker C.L. Werner. (1988). Satellite radar interferometry: Two-dimensional phase unwrapping, *Radio Science* **23,** 713-720.

Graves, R. W. (1995). Preliminary analysis of long-period basin response in the Los Angeles region from the 1994 Northridge earthquake, *Geophysical Research Letters* **22,** 101-104.

Hager, B., G. Lyzenga, A. Donnellan, D. Dong. (1999). Reconciling rapid strain accumulation with deep seismogenic fault planes in the Ventura basin, California, *Journal of Geophysical Research* **104,** 25207-25219.

Hanssen, R. (2001) *Radar interferometry: Data interpretation and error analysis,* Springer, New York.

Harris, Ruth, P. Segall. (1987). Detection of a locked zone at depth on the Parkfield, California, segment of the San Andreas Fault, *Journal of Geophysical Research* **92,** 7945-7962.

Hauksson, E., L. Jones, K. Hutton. (1995). The 1994 Northridge earthquake sequence in California: Seismological and tectonic aspects, *Journal of Geophysical Research* **100,** 12335-12355.

Hearn, E.H., R. Bürgmann. (2005). The effect of elastic layering on inversion of GPS data for coseismic slip and resulting stress changes: strike-slip earthquakes, *Bulletin of the Seismological Society of America* **95,** 1637-1653.

Hecker, S., D.J. Ponti, C.D. Garvin J.C. Hamilton. (1995). Characteristics of the origin of ground deformation produced in Granda Hills and Mission Hills during the January 17, 1994 Northridge earthquake, *Northridge, California earthquake, January 17, 1994* California Division of Mines Geological Special Publication**,** 111-131.

Holzer, T., M. Bennett, D. Ponti, J. Tinsley. (1999). Liquefaction and soil failure during 1994 Northridge earthquake, *Journal of Geotechnical and Geoenvironmental Engineering* **,** 438-452.

Hudnut K.W., Z. Shen, S. McClusky, R. King, T. Herring, B. Hager, Y. Feng, P. Fang, A. Donnellan, Y. Bock. (1996). Co-seismic displacements of the 1994 Northridge, California, earthquake, *Bulletin of the Seismological Society of America* **86,** S19-S36.

Huftile, G., R. Yeats. (1995). Convergence rates across a displacement transfer zone in the western Transverse Ranges, Ventura Basin, California, *Journal of Geophysical Research* **100,** 2043-2067.

Huftile, G., R. Yeats. (1996). Convergence rates across the Placerita (Northridge Mw=6.7 aftershock zone) and Hopper Canyon segments of the western Transverse Ranges deformation belt, *Bulletin of the Seismological Society of America* **86,** S3-S18.

Jackson, J. R. Norris, J. Youngson. (1996). The structural evolution of active fault and fold systems in central Otago, New Zealand: evidence revealed by drainage patterns, *Journal of Structural Geology* **18,** 217-234.

Jónsson, S., H. Zebker, P. Segall, F. Amelung. (2002). Fault slip distribution of the 1999 Mw 7.1 Hector Mine, California, earthquake, estimated from satellite radar and GPS measurements, *Bulletin of the Seismological Society of America* **92,** 1377-1389.

King, G. C. P., R. S. Stein, and J. Lin (1994), Static Stress Changes and the Triggering of Earthquakes, *Bulletin of the Seismological Society of America*, *84*(3), 935-953.

Kohler M.D., H. Magistrale, R.W. Clayton. (2003). Mantle heterogeneities and the SCEC three-dimensional seismic velocity model version 3, *Bulletin of the Seismological Society of America* **93,** 757-774.

Li, Z., E.J. Fielding, P. Cross, R. Preusker. (2008). Advanced InSAR atmospheric correction: MERIS/MODIS combination and stacked water vapour models, *International Journal of Remote Sensing* **30,** 3343-3363.

Lin, G., P. Shearer, and E. Hauksson (2007), Applying a three-dimensional velocity model, waveform cross correlation, and cluster analysis to located southern California seismicity from 1981 to 2005, *Journal of Geophysical Research*, *112*(B12309).

Lockner, D. A., C. Morrow, D. Moore, and S. Hickman (2011), Low strength of deep San Andreas fault gouge from SAFOD core, *Nature*, *472*, 82-85.

Maerten, F., P. Resor, D. Pollard, L. Maerten. (2005). Inverting for slip on three-dimensional fault surfaces using angular dislocations, *Bulletin of the Seismological Society of America* **95,** 1654-1665.

Marshall, S., A.C. Morris. (2012). Mechanics, slip behavior, and seismic potential of corrugated dip-slip faults, *Journal of Geophysical Research* **117,** B03403.

Marshall, S., M. Cooke, S. Owen. (2008). Effects of nonplanar fault topology and mechanical interaction on fault-slip distributions in the Ventura basin, California, *Bulletin of the Seismological Society of America* **98,** 1113-1127.

Massonnet, D., K. Feigl, H. Vadon, M. Rossi. (1996). Coseismic deformation field of the M=6.7 Northridge, California earthquake of January 17,1994 recorded by two radar satellites using interferometry, *Geophysical Research Letters* **23,** 969-972.

Massonnet, D., K. Feigl. (1998). Radar interferometry and its application to changes in the Earth's surface, *Reviews of Geophysics* **36,** 441-500.

Murakami, M., M. Tobita, S. Fujiwara, T. Saito, H. Masaharu. (1996). Coseismic crustal deformations of 1994 Northridge, California, earthquake detected by interferometric JERS 1 synthetic aperture radar, *Journal of Geophysical Research* **101,** 8605-8614.

Nielsen, S, K. Olsen. (2000). Constraints on stress and friction from dynamic rupture models of the 1994 Northridge, California, earthquake, *Pure and Applied Geophysics* **157,** 2029-2046.

Okada, Y. (1985). Surface deformation due to shear and tensile faults in a half-space, *Bulletin of the Seismological Society of America* **75,** 1135-1154.

Petersen, M.D., W.A. bryant, C. Cramer, T. Cao, M. Reichle, A. Frankel, J. Lienkaemper, P. McCrory, D. Schwartz. (1996). Probabilistic Seismic Hazard Assessment for the State of California, *California Geological Survey - Regional Geologic Mapping Program.*

Plesch, A., J. Shaw, C. Benson, W. Bryant, S. Carena, M. Cook, J. Dolan, G. Fuis, E. Gath, L. Grant, E. Hauksson, T. Jordan, M. Kamerling, M. Legg, S. Lindvall, H. Magistrale, C. Nicholson, N. Niemi, M. Oskin, S. Perry, G. Planansky, T. Rockwell, P. Shearer, C. Sorlien, M. Süss, J. Suppe, J. Treiman, R. Yeats. (2007). Community fault model (CFM) for southern California, *Bulletin of the Seismological Society of America* **97,** 1793-1802.

Resor, P., V. Meer. (2009). Slip heterogeneity on a corrugated fault, *Earth and Planetary Science Letters* **228,** 483-491.

Rosen, P.A., S. Hensley, I. Roughin, L.K. Fuk, S.N. Madsen, E. Rodriguez, R. Goldstein. (2000). Synthetic Aperture Radar Interferometry, *Proceedings of the IEEE* **88,** 333-382.

Rosen, P. A., S. Hensley, and G. Peltzer (2004), Updated Repeat Orbit Interferometry Package released, Eos Trans. AGU, 85(5).

Rosen, P.A., S. Hensley, K. Wheeler, G. Sadowy, T. Miller, S. Shaffer, R. Muellerschoen, C. Jones, H. Zebker, S. Madsen. (2006). UAVSAR: A New NASA Airborne SAR System for Science and Technology Research, *IEEE Conference Publications* **,** 22-29.

Rymer, M, T. Fumal, D. Schwartz, T. Powers, F. Cinti. (1995). Distribution and recurrence of surface fractures in Potrero Canyon associated with the 1994 Northridge, California earthquake, *Northridge, California earthquake, January 17, 1994* California Division of Mines Geological Special Publication**,** 133-146.

Savage, J.C., J. Svarc. (2010). Postseismic relaxation following the 1994 Mw 6.7 Northridge earthquake, southern California, *Journal of Geophysical Research* **115.**

Scientists of the U.S. Geological Survey and the Southern California Earthquake Center. (1994). The Magnitude 6.7 Northridge, California, Earthquake of 17 January 1994, *Science* **5184,** 389-397.

Shaw, J.H. J. Suppe. (1994). Active faulting and growth folding in the eastern Santa Barbara Channel, California, *Geological Society of America Bulletin* **106,** 607-626.

Shaw, J.H. J. Suppe. (1996). earthquake hazards of active blind-thrust faults under the central Los Angeles basin, California, *Journal of Geophysical Research* **101,** 8623-8642.

Shearer, P., E. Hauksson, G. Lin. (2005). Southern California hypocenter relocation with waveform cross correlation, part 2: Results using source-specific station terms and cluster analysis, *Bulletin of the Seismological Society of America* **95,** 904-915.

Shen, Z., D. Jackson, B. Ge. (1996) Crustal deformation across and beyond the Los Angeles basin form geodetic measurements. *Journal of Geophysical Research* **101,** 27957-27980.

Simons, M., Y. Fialko, L. Rivera. (2002). Coseismic deformation from the 1999 Mw 7.1 Hector Mine, California, earthquake as inferred from InSAR and GPS Observations, *Bulletin of the Seismological Society of America* **92,** 1390-1402.

Somerville, P., C. Saikia, D. Walt, R. Graves. (1996). Implications of the Northridge earthquake for strong ground motions from thrust faults, *Bulletin of the Seismological Society of America* **86,** S115-S125.

Spudich, P., M Hellweg, W.H.K Lee. (1996). Aftershocks of the 1994 Northridge, California, Earthquake: Implications for mainshock motions, *Bulletin of the Seismological Society of America* **86,** S193-S208.

Stein, R., R.S. Yeats. (1989). Hidden Earthquakes, *Science America* **260,** 48-57.

Stewart, J., R. Seed, J. Bray. (1996). Incidents of Ground Failure from the 1994 Northridge Earthquake, *Bulletin of the Seismological Society of America* **86,** S300-S318.

Stover, C., J. Coffman. (1994). Seismicity of the United States, 1568-1989, *U.S. Department of the Interior***.**

Stramondo, S., F. Del Frate, M. Picchiani, G. Schiavon. (2011). Seismic Source Quantitative Parameters Retrieval From InSAR Data and Neural Networks, *IEEE Conference Publications* **49,** 96-104.

Thomas, A. L. (1993). POLY3D: A three-dimensional, polygonal element, displacement discontinuity boundary element computer program with applications to fractures, faults, and cavities in the Earth's crust, Master's Thesis Stanford University, 52 pp.

Trifunac, M.D., M.I. Todorovska, S.S. Ivanovic. (1994). A note on distribution of uncorrected peak ground accelerations during the Northridge, California, earthquake of 17 January 1994, *Soil Dynamics and Earthquake Engineering* **,** 187-196.

Vannoli, P., R. Basili, G. Valensise. (2004). New geomorphic evidence for anticlinal growth driven by blind-thrist faulting along the northern Marche coastal belt (central Italy), *Journal of Seismology* **8,** 297-312.

Wald, D., T. Heaton, K. Hudnut. (1996). The slip history of the 1994 Northridge, California, earthquake determined from strong-motion, teleseismic, GPS and leveling data, *Bulletin of the Seismological Society of America* **86,** S49-S70.

Webley P.W., R.M. Bingley, A.H. Dodson, G. Wadge, S.J. Waugh, I.N. James. (2002). Atmospheric water vapour correction to InSAR surface motion measurements on mountains: results from a dense GPS network on Mount Etna, *Physics and Chenistry of the Earth* **27,** 363-370.

Weston, J., A. Ferreira, G. Funning. (2012). Systematic comparisons of earthquake cource models determined using InSAR and seismic data, *Tectonophysics* **532-535,** 61-81.

Wright, T.J., B.E. Parsons, J.A. Jackson, M. Haynes, E.J. Fielding, P.C. England, P.J. Clarke. (1999). Source parameters of the 1 October 1995 Dinar (Turkey) earthquake from SAR interferometry and seismic bodywave modelling, *Earth and Planetary Science Letters* **172,** 23-37.

Wright, T.J.. (2002). Remote monitoring of the earthquake cycle using satellite radar interferometry, *The Royal Society* **10.1098,** 2873-2888.

Wright, T.J., Z. Lu, C. Wicks. (2003). Source model for the Mw 6.7, 23 October 2002, Nenana Mountain Earthquake (Alaska) from InSAR, *Geophysical Research Letters* **30,** 1975.

Yeats, R., G. Huftile. (1995). The Oak Ridge fault system and the 1994 Northridge earthquake, *Letters to Nature* **373,** 418-420.

Yeats, R.S.. (2004). Tectonics of the San Gabriel basin and surroundings, Southern California, *Geological Society of America Bulletin* **116,** 1158-1182.

Appendix A: Northridge supplemental materials

A1. Single fault inversion uncertainties

Uncertainties in our model parameters are estimated using a bootstrap test where 100 perturbed data sets are produced and each is inverted in *Okinv*. We produce realizations of random realistic correlated noise for this purpose by using the 1D covariance versus distance relationship estimated from the autocorrelation of an undeformed portion of each interferogram (e.g. Wright et al., 2003).
The parameter values of each inversion can be plotted as a histogram or plotted against other parameters in order to assess tradeoffs between these parameters. A well-resolved parameter will show a large peak in the histogram as well as a tight clustering in the tradeoff plots, which means the inversion has converged on approximately the same result each time the inversion is run.

Our one- fault model appears precise, as the tradeoffs in most parameters form tight clustering and the histograms show sharp peaks (Figure A1). There are tradeoffs between the east-west positioning of the fault and both strike and rake, however, these tradeoffs are quite small. This means that there is some uncertainty in the relationship between these parameters. As the fault is positioned farther east, the strike increases and the fault extends to shallower depths.

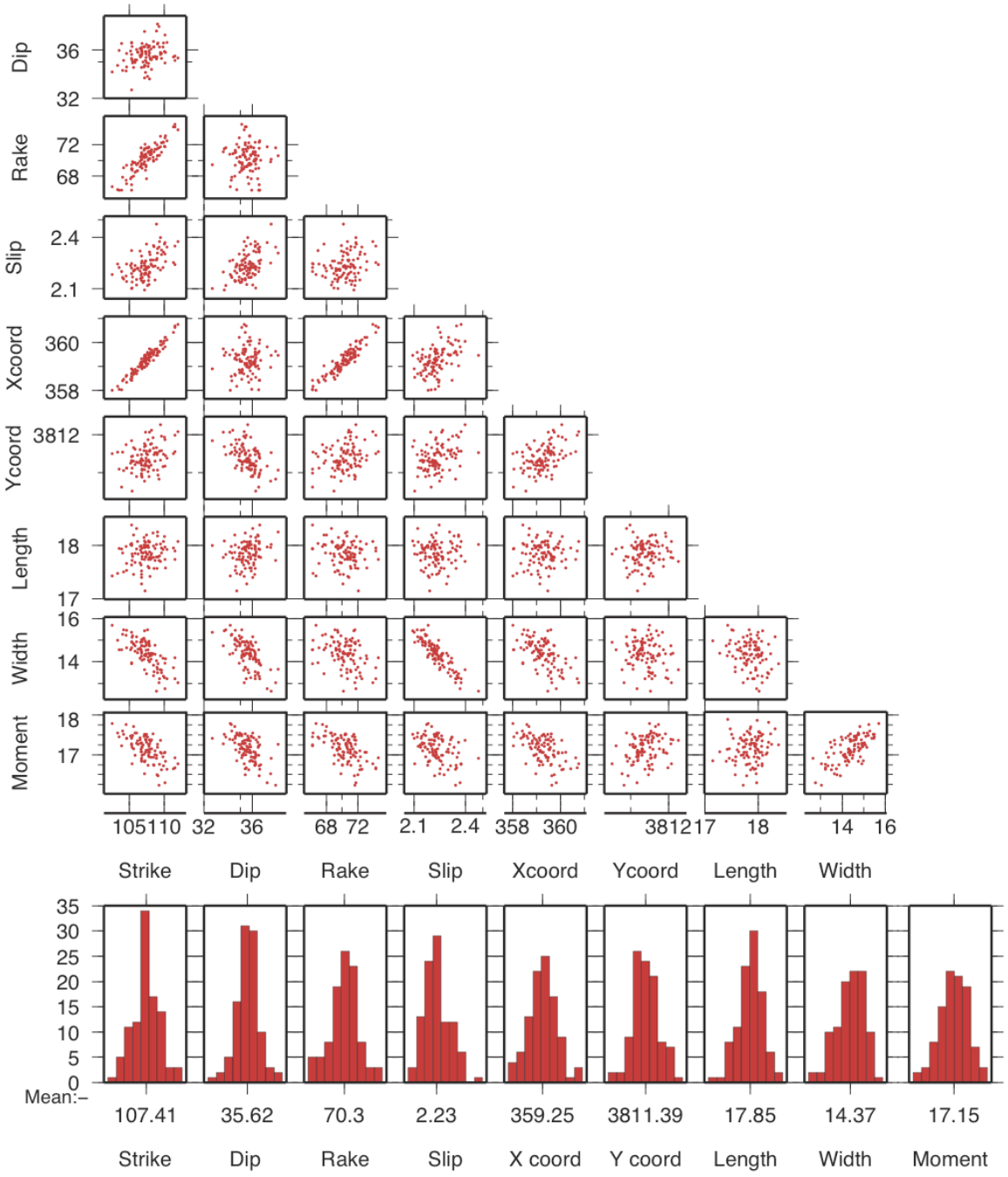

Figure A1 Plots show tradeoffs between model parameters as a result of the inversion, histograms show uncertainties in model parameters. Xcoord and YCoord are the Easting and Northing of the fault center projected to the surface in UTM km zone 11.

A2. Two-fault inversion uncertainties

For our two-fault inversion we hold one fault fixed and allow all parameters of the other fault to vary in order to avoid large tradeoffs between the two faults. The two-fault model is less well resolved than the one fault model. The secondary fault, in particular, is not well resolved, most likely due to a lack of data in the western region of the fault (Figure A2).

A3. Variable slip model inversion

Using the Northridge CFM as a fixed fault geometry allows us to invert for a variable slip and rake distribution for a fault slip solution. Our inversion is represented by

$$\mathbf{a} = \left[\mathbf{H}^{\mathrm{T}}\mathbf{E}^{-1}\mathbf{H}\right]^{-1}\mathbf{H}^{\mathrm{T}}\mathbf{E}^{-1}\mathbf{b} \qquad \text{(A1)}$$

Where **a** is the slip in meters of a given fault, **H** is the Green's function relating

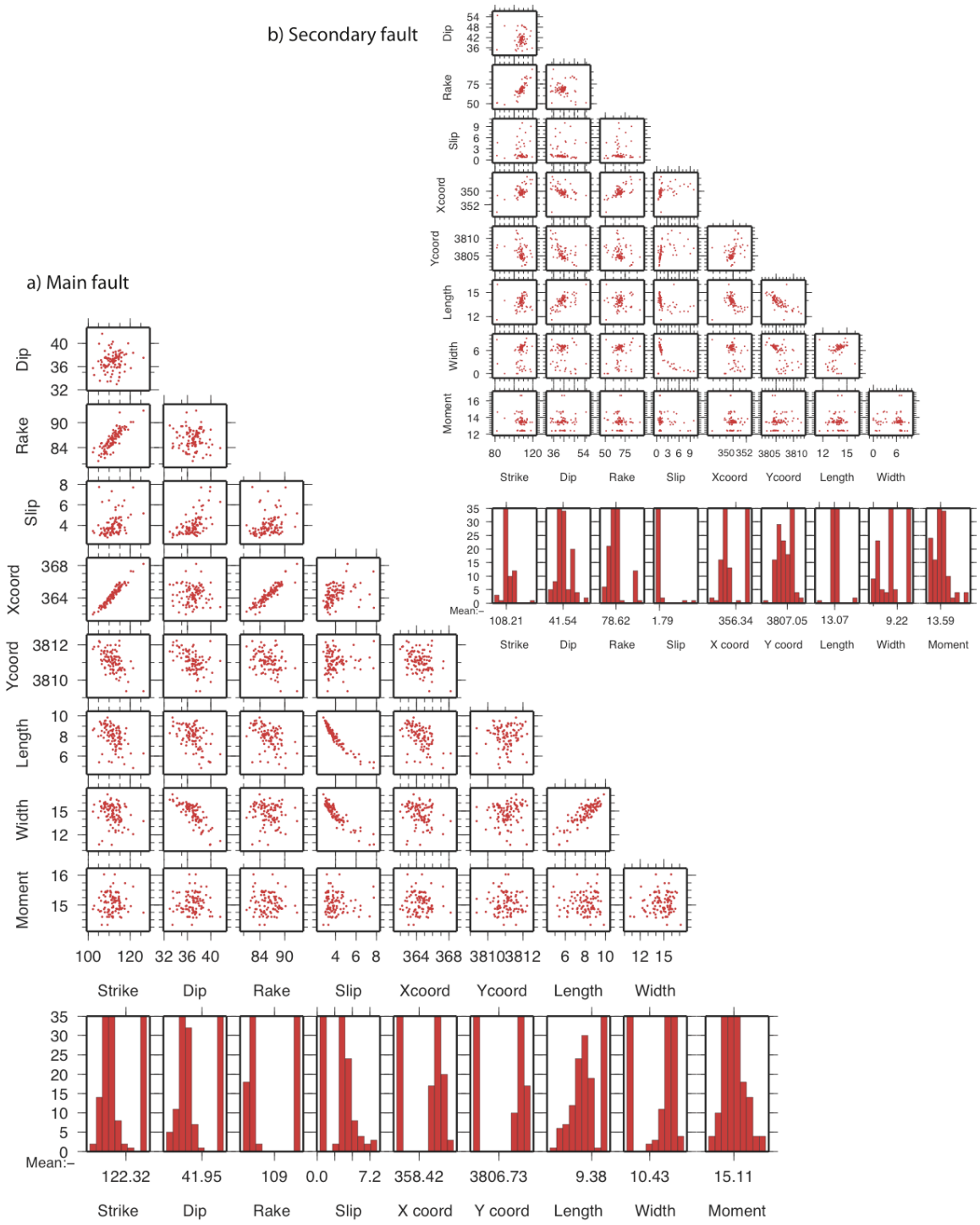

Figure A2 a) Uncertainties of the main fault in the two-fault inversion. b) Uncertainties of the secondary fault in the two-fault inversion.

displacement to slip on the fault, and E is the covariance matrix determined by calculating the autocorrelation of an undeformed section of each interferogram for InSAR and the uncertainties for the GPS data, which is used for weighting,

represented by

$$\mathbf{E} = \begin{bmatrix} \mathbf{E_{ERS}} & \mathbf{0} & \mathbf{0} \\ \mathbf{0} & \mathbf{E_{JERS}} & \mathbf{0} \\ \mathbf{0} & \mathbf{0} & \mathbf{E_{GPS}} \end{bmatrix}. \tag{A2}$$

b is surface deformation observations with ramps and offsets removed shown by

$$\begin{pmatrix} b_{ers} \\ b_{jers} \\ b_{gps\_east} \\ b_{gps\_north} \\ 0 \end{pmatrix} = \begin{pmatrix} H_{ers\_left} & H_{ers\_right} & -1 & -x_{ers} & -y_{ers} & 0 & 0 & 0 & 0 & 0 \\ H_{jers\_left} & H_{jers\_right} & 0 & 0 & 0 & -1 & -x_{jers} & -y_{jers} & 0 & 0 \\ H_{gps\_east\_left} & H_{gps\_east\_right} & 0 & 0 & 0 & 0 & 0 & 0 & -1 & 0 \\ H_{gps\_north\_left} & H_{gps\_north\_right} & 0 & 0 & 0 & 0 & 0 & 0 & 0 & -1 \\ \kappa S_{left} & \kappa S_{right} & 0 & 0 & 0 & 0 & 0 & 0 & 0 & 0 \end{pmatrix} \begin{pmatrix} a_{left} \\ a_{right} \\ d_{ers0} \\ p_{ers} \\ q_{ers} \\ d_{jers0} \\ p_{jers} \\ q_{jers} \\ d_{gps\_east0} \\ d_{gps\_north0} \end{pmatrix} + e \tag{A3}$$

where d_0 is a translation in the dataset, x and y are the datapoints in the east-west and north south directions, respectively. p and q are gradients in the east-west and north-south directions, respectively. We solve for slip in two directions, each 45° each side of pure reverse slip denoted by left and right (Figure A3). κ is the smoothing factor chosen by selecting the optimal tradeoff between model roughness and WRSS and e is a vector of random errors (Figure A3).

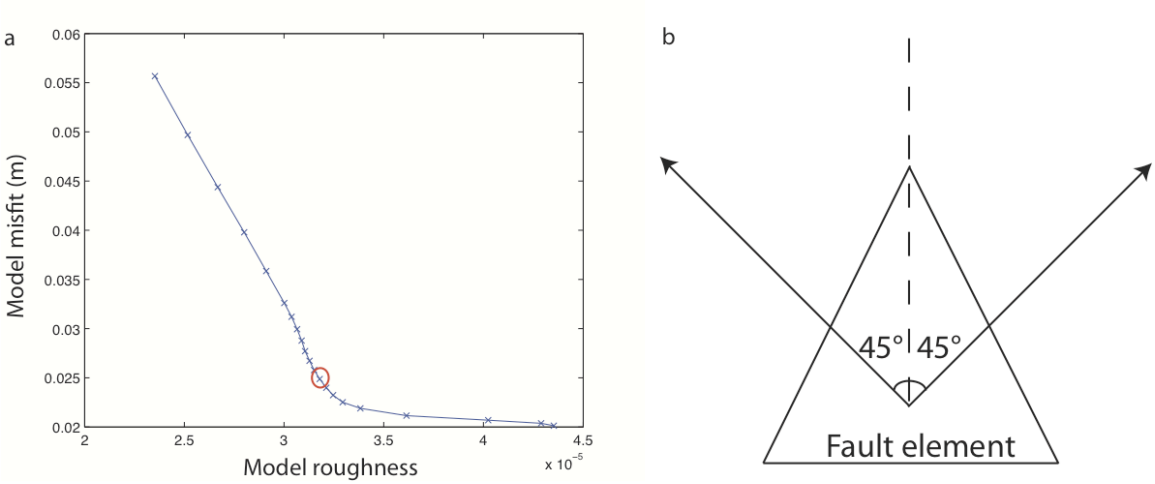

Figure A3 a) The smoothing value is determined by selecting the optimal tradeoff between model roughness and model misfit The range of rakes permitted in our inversion range between 45° (between 45° and 135°) of pure reverse slip. The pure reverse slip direction is denoted by the dashed line.

A4. Individual model contributions

Each dataset is inverted individually in order to show its contributing factors to the overall preferred model. The models for the GPS (Figure A4), ERS-1 (Figure A5) and JERS-1 (Figure A6) data are shown below. The models derived from InSAR data appear to agree with each other, except in the west of the fault. The JERS-1 data allows for slip farther updip than the ERS-1, which is most likely due to the additional data coverage from the digitized fringes. Furthermore, the rake in the JERS-1 data to the west is also close to pure thrust movement while the ERS-1 model shows a more oblique slip direction. This is also most likely due to the additional data as the JERS-1 digitized fringes show 40 cm of uplift to the west, which is not present in the ERS-1 data due to decorrelation. The GPS model places the main asperity in the same location as the InSAR models, however, rake is in a different

direction. Also, slip to the west is farther updip than the InSAR models. This is most likely due to the lower spatial sampling of data. The GPS model places deformation north of what the InSAR data suggest in the western area of the deformation pattern.

A5. Linear inversion uncertainties and resolution

A5.1. Checkerboard test

In order to determine the resolving power of our model, we employ a checkerboard test whereby sections of the Northridge fault are given slip values of either 1m or 0m resembling a checkerboard (figure A7a). Our checkerboard patches vary slightly in area, but are, on average, ~6.5km^2. A forward model is calculated to determine the effect of these slip displacements on the surface at the locations of our data points and those displacements are then used as data in an inversion for slip. For patches of the fault that are not well resolved, the initial slip values will be greatly changed in the inversion. The results show that our model is well resolved by our data until ~20km depth where the values begin to blend together (Figure A7b). This is explicable, as our model does not place slip at this depth. Furthermore, it has been suggested by geodetic (Hudnut et al., 1996) and seismic (Wald et al., 1996) inversions as well as aftershock data (Hauksson et al., 1995) that all slip occurred above this depth.

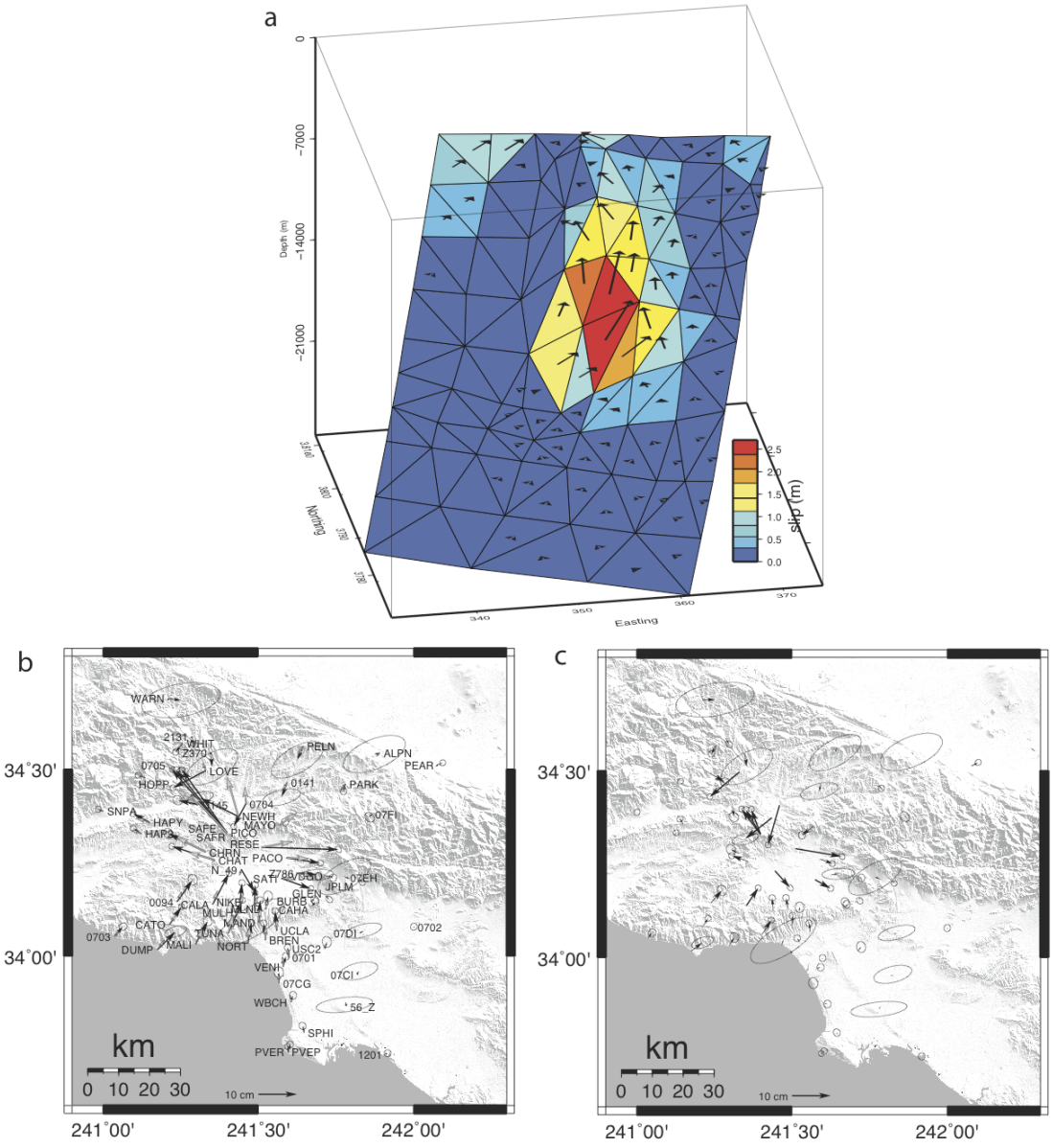

Figure A4 Results of the GPS data inversion. a) GPS data and model. Black vectors represent the data with 1-sigma error ellipses. Gray vectors represent the model calculations. b) GPS residuals with 1-sigma error ellipses.

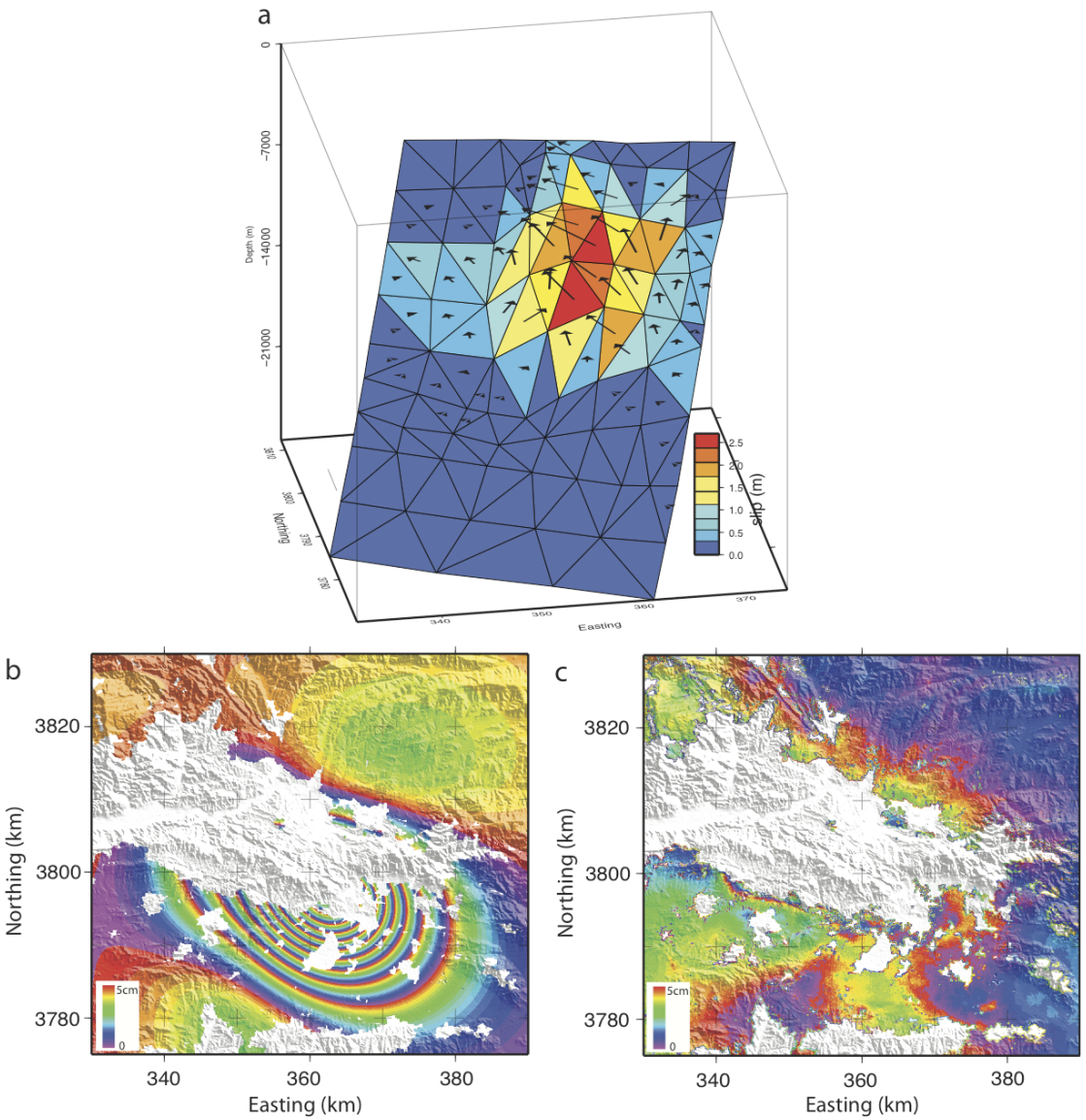

Figure A5 Results of the ERS-1 data inversion. a) slip distribution b) ERS-1 model c) ERS-1 residual

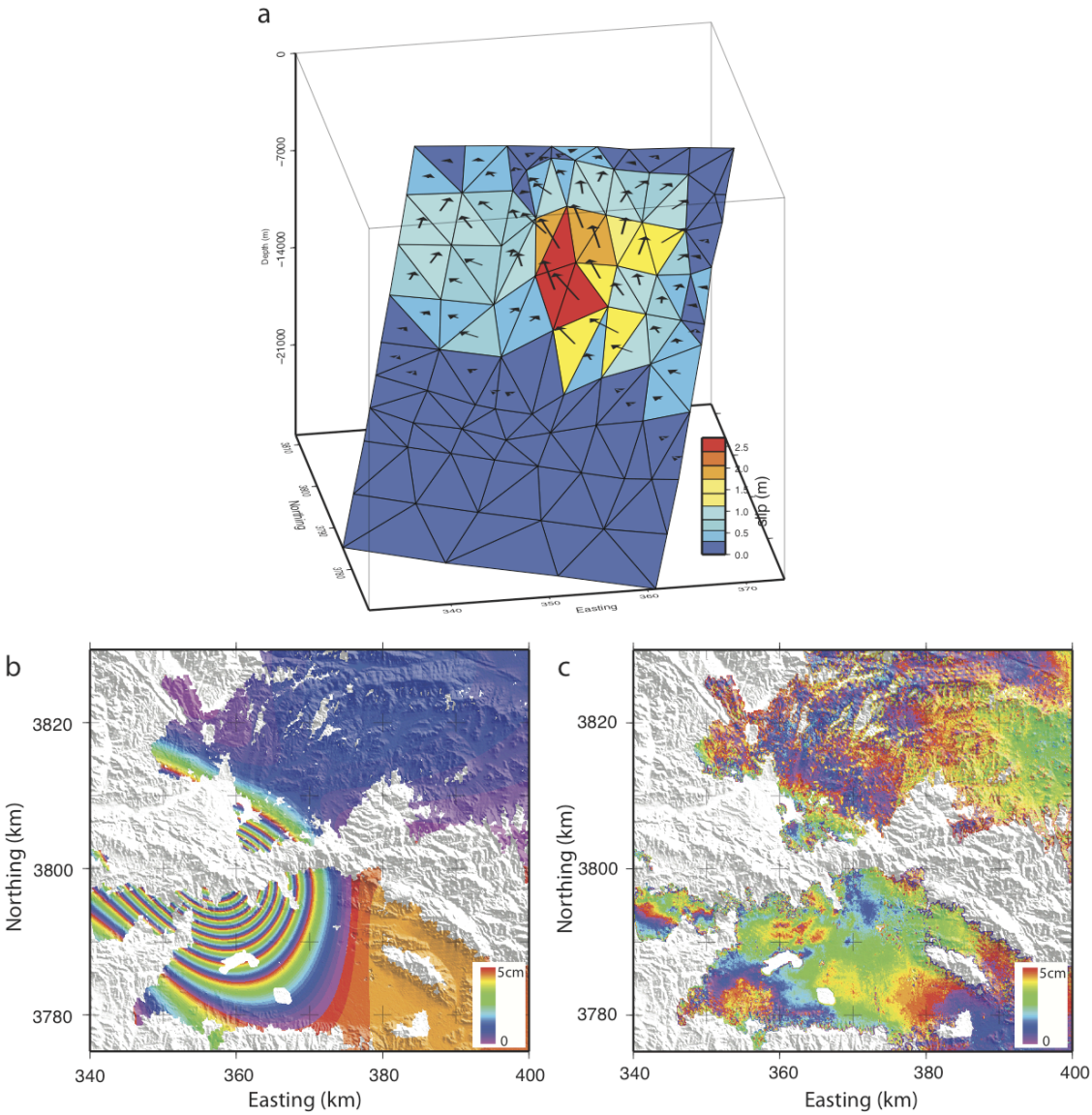

Figure A6 Results of the JERS-1 data inversion. a) slip distribution b) JERS-1 model c) JERS-1 residual

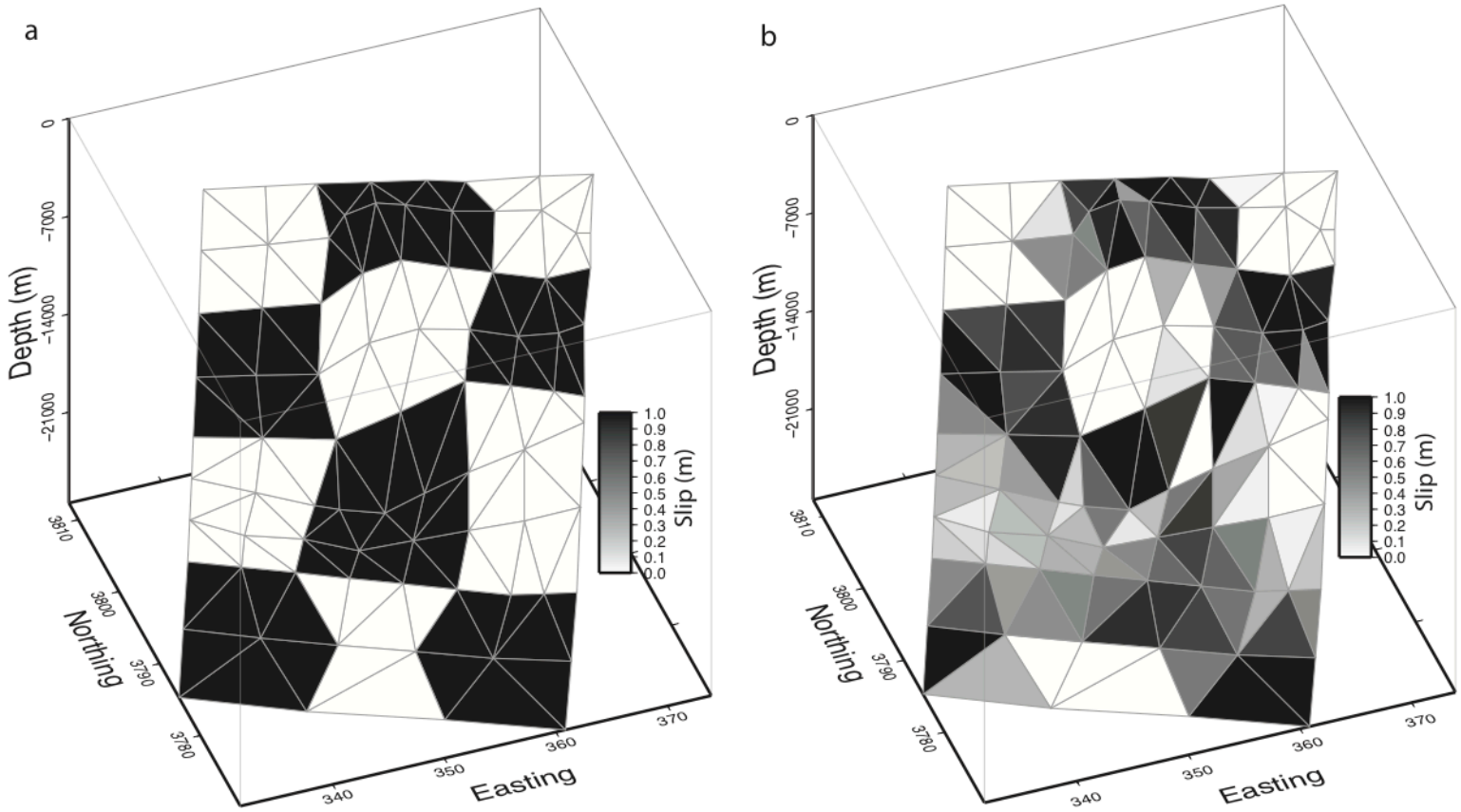

Figure A7 a) Our "checkerboard" pattern on the Northridge thrust. b) Results of the checkerboard test. Our model appears to be well resolved until ~20km depth.

A5.2. Linear inversion bootstrap test

Since we use the Northridge CFM as a fixed fault reference, we can measure the uncertainties in slip on the fault when the data are perturbed with noise. The 1-sigma standard deviation in slip from the slipinv bootstrap test peaks at 6cm for the deep portion of the fault that which not well resolved (Figure A8). Furthermore, we model no slip in this section of the fault. Areas of peak slip in our variable slip model do not vary significantly with added noise, as the area of peak slip in our model has a ~2.5cm standard deviation in slip, 1% of the slip amount predicted by our model. These tests show that our model appears to have the resolution and robustness required for a reliable solution.

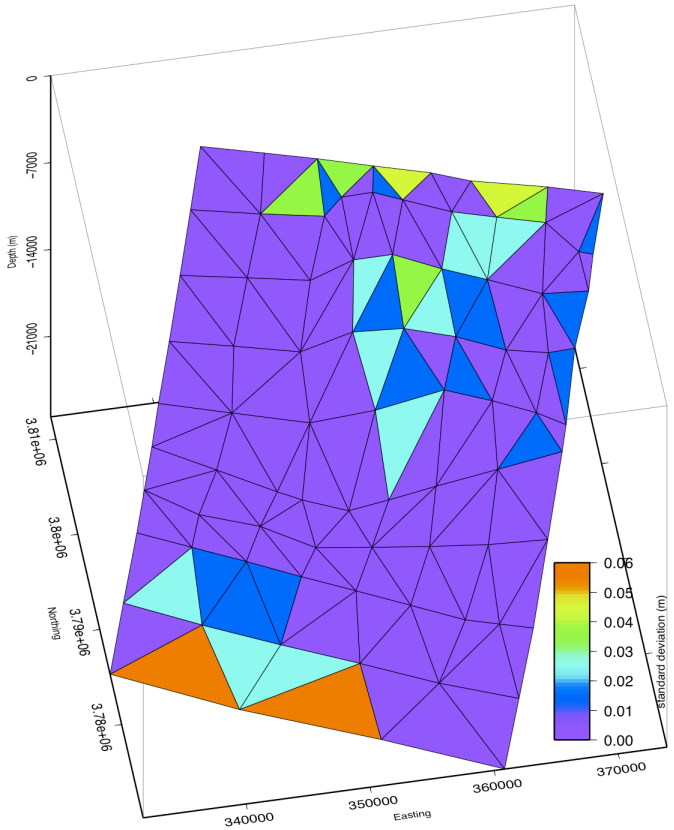

Figure A8 Standard deviation in slip as a result of our bootstrap test. The largest deviation in slip occurs at the bottom of the fault below 20km depth. The area of peak slip appears to be precisely determined in that it has only a ~1cm standard deviation in slip

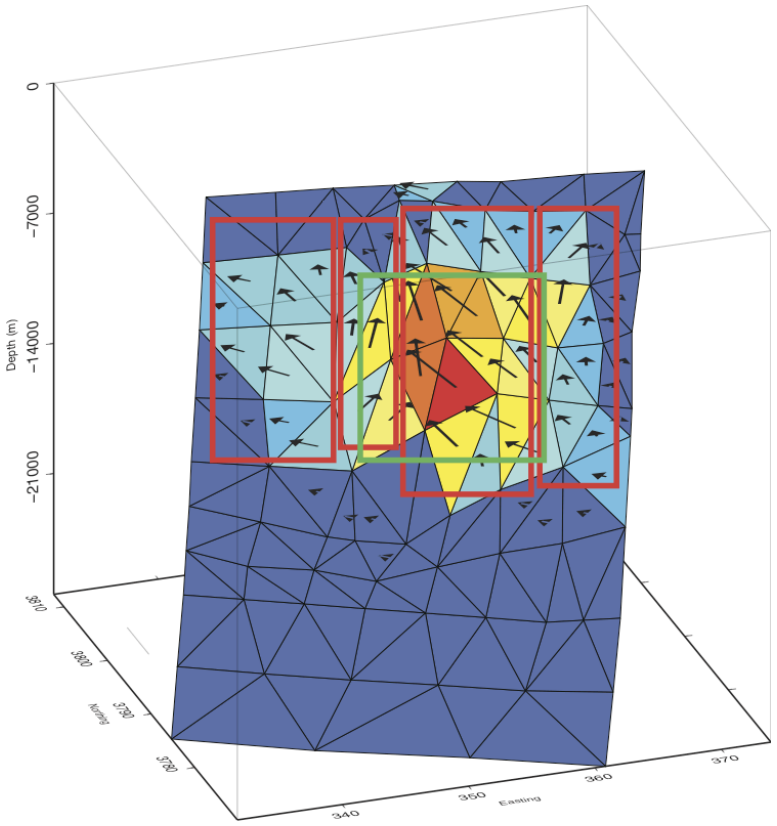

Figure A9 Our preferred fault solution. The green box marks the protuberance on the fault in which peak slip occurs. The red boxes point to the alternating bands of rake indicative of oblique loading on a corrugated/wavy dip-slip fault. The second red box from the left approximately follows the steep decline on the fault.

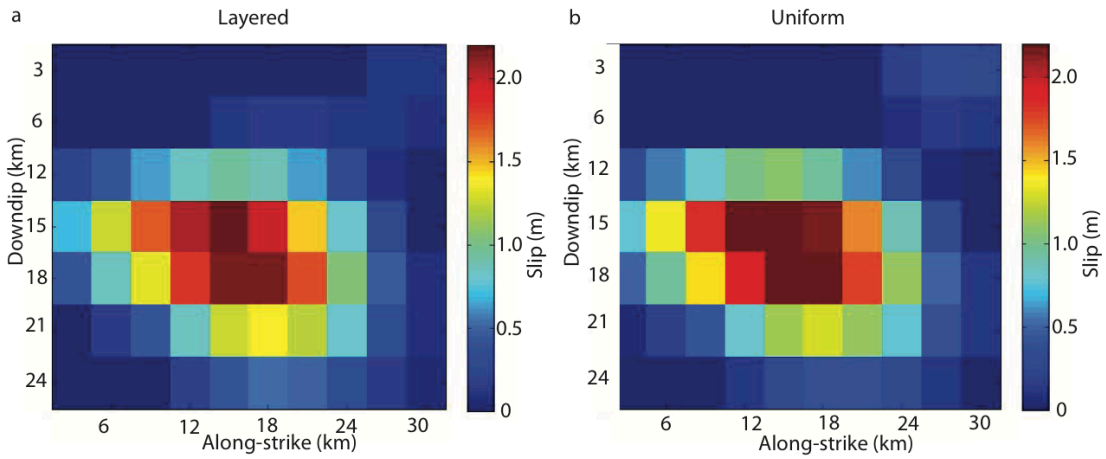

Figure A10 A variable slip inversion of the Northridge earthquake using a two-layered elastic structure determined by the Community Velocity Model (Kohler et al., 2003), versus a uniform elasticity of 30 Gpa. Slip moves downdip using the layered elastic model, however, the change between the two models is small. Each fault patch is ~3 km^2.

Appendix B: Static stress changes on the San Andreas fault due to the Northridge earthquake

Dr. Scott Marshall and Julia Irizarry of Appalachian State University have completed the work below. While these specific contributions are not my own, I have provided the model by which these calculations are made (Chapter 2). This section highlights the usefulness of calculating an accurate coseismic model of an earthquake.

Based on campaign GPS data collected shortly after the Northridge coseismic event, Savage and Svarc (2010) suggest that the Northridge earthquake may have triggered deep aseismic slip on the nearby San Andreas fault. A two-dimensional kinematic dislocation model with 45 mm of slip between 10-30 km depth on the San Andreas fault appears reproduce the dominant deformation signal in the postseismic period of 100 days (Savage and Svarc, 2010); however, it is not known if such an interaction is mechanically viable. Using our CFM-based coseismic slip model, we calculate the static stress changes and test the plausibility of postseismic triggered slip on the San Andreas fault due to the Northridge earthquake.

To calculate the static stress changes on the San Andreas fault, we apply our CFM-based slip model of the Northridge earthquake a priori and calculate the static stress changes on the San Andreas fault using a fully locked boundary condition in poly3d (Thomas 1993). The model-predicted static stress changes suggest that the

Northridge event should have unclamped a portion of the San Andreas fault surface, increasing the likelihood of failure (Figure B1). The shear stress changes in the strike direction suggest that the San Andreas fault received increased right-lateral and left-lateral shear stresses in two neighboring patches (Figure B1). This is a consequence of the fact that the Northridge earthquake ruptured a relatively short fault segment, which according to dislocation theory (e.g. Okada 1985) should produce significant surface motions that are not parallel to the dip direction of the fault. This phenomenon is clearly visible in the coseismic GPS displacement field (Figure 2.4). Therefore, the permanent motions induced by the Northridge event should effectively pull on the San Andreas fault in different directions at different locations. Using the standard Coulomb stress formulation (e.g. King and Stein, 1994) and a low 0.15 friction value indicative of a frictionally weak San Andreas fault (i.e. Lockner et al., 2011), the model predicts two likely zones of failure. The southernmost zone of high Coulomb stress could potentially produce a right-lateral rupture, while the northern zone could produce a left-lateral rupture. While there have been observations of retrograde triggered slip (i.e. slip that is backwards with respect to a fault's long-term slip direction) after some moderately large earthquakes (e.g. Fialko et al., 2002), there is no geodetic or seismologic evidence that the model-predicted patch of left-slip actually ruptured. The postseismic GPS displacements of Savage and Svarc (2010), however, seem to indicate the possibility that there may have been triggered right-lateral slip on the San Andreas. Therefore in all subsequent models we ignore left-lateral shearing (we assume that resolved

left-lateral shear simply counteracts and unloads some of the accumulated right-lateral shear stresses) and only report the potential right-lateral shearing values.

B1. The potential for triggered slip on the San Andreas fault due to the Northridge earthquake

To calculate the potential magnitude of triggered slip on the San Andreas fault, we again use our preferred CFM-based slip model and apply a shear stress free boundary condition in the along strike direction and locked boundary conditions in the opening and down-dip directions on the San Andreas fault using poly3d. Because the model boundary conditions assume a frictionless San Andreas in the along strike direction, we consider this model to represent the maximum mechanically-plausible triggered slip. Furthermore, because there was no evidence of surface rupture along the San Andreas after the Northridge event, we lock the top row of elements simulating a ~10 km locking depth (identical to the locking depth suggested by Savage and Svarc, 2010). The model predicts two patches of triggered slip (one left-lateral and one right-lateral as was expected from the stress change models), however, for reasons described earlier, we only show and describe the model-predicted right-lateral slip patch.

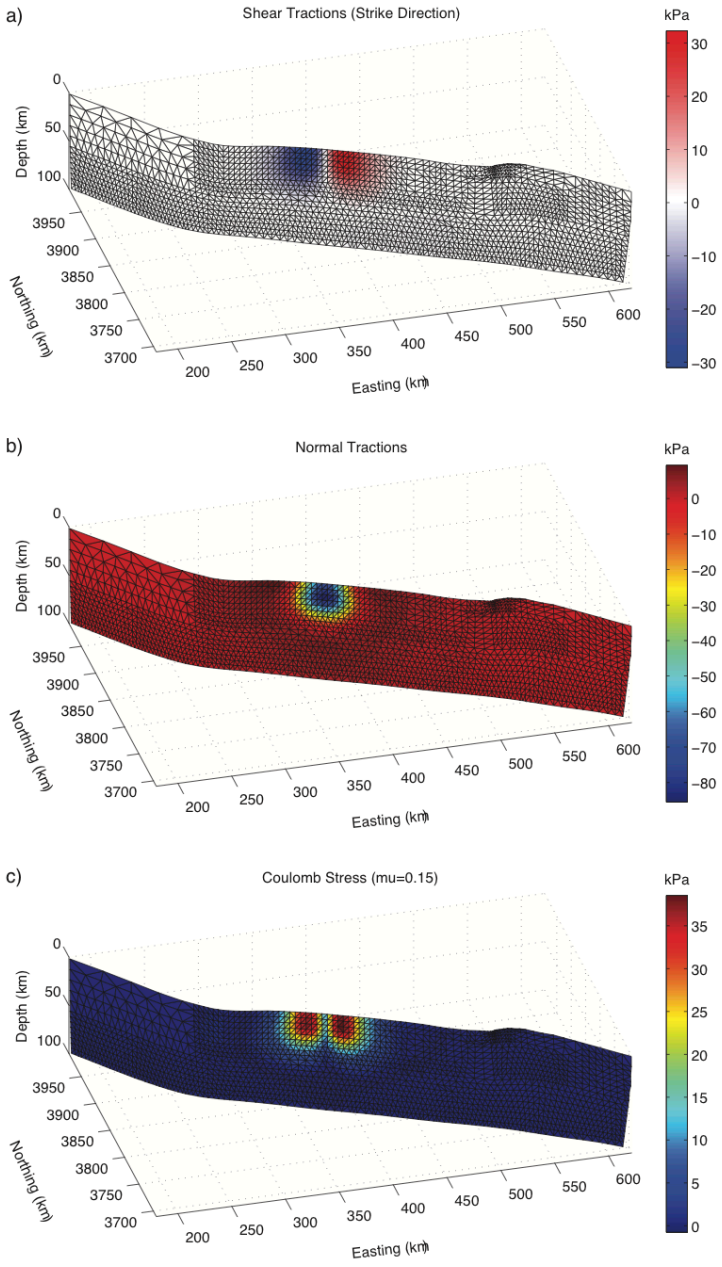

Figure B1 Static stress changes on the San Andreas fault due to our preferred Northridge slip model. Like the Northridge fault, the San Andreas fault mesh is based on the CFM, but has been remeshed to attain approximately uniform element size. Positive shear tractions are right-lateral while positive normal tractions are compressive. a) shows the shear traction change in the strike direction, b) shows the normal traction change, and c) shows the Coulomb stress change given a coefficient of friction of 0.15.

The model-predicted triggered right-lateral slip patch has a maximum slip of 20 mm, and an approximate length of 65 km and width of 50 km (Figure B2). The model of triggered slip presented by Savage and Svarc (2010) requires a constant slip of 45 mm from 10-30 km depth on the San Andreas fault, more than double the prediction of the maximum slip in the mechanical model. Because a two-dimensional model implies infinite length in and out of the plane of reference, the Savage and Svarc (2010) model produces surface displacements that are nearly a factor of 20 times larger than our finite slip patch (Figure B3). Therefore, the postseismic GPS motions presented by Savage and Svarc (2010) are unlikely to have been caused by triggered slip and if there was triggered slip on the San Andreas fault, the surface displacements due to the model predicted triggered slip patch would not likely have been above the noise level in the GPS data.

B2. Is there seismological evidence for triggered slip on the San Andreas fault?

Our mechanical model results suggest that triggered slip on the San Andreas fault due to the Northridge earthquake is mechanically plausible; however, the surface displacements produced by the model-predicted triggered slip on the San Andreas

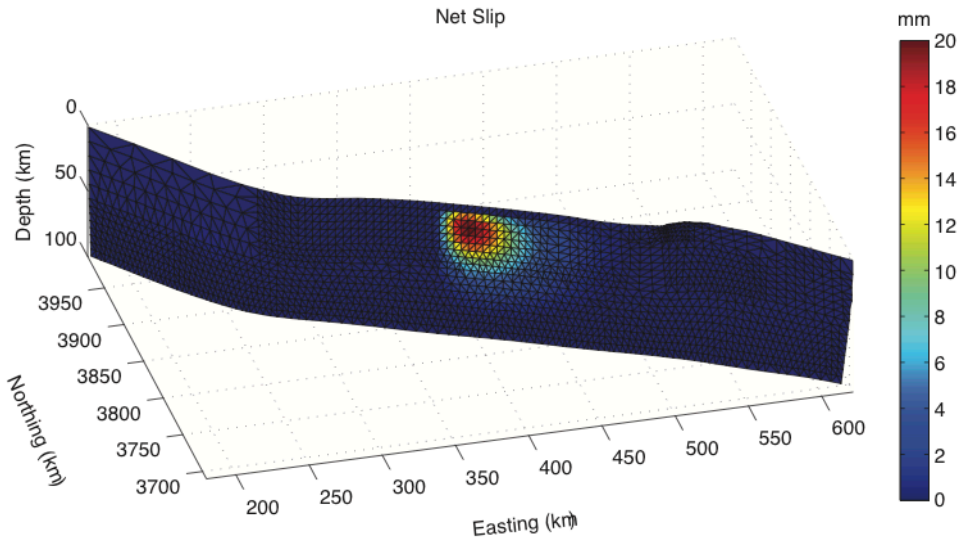

Figure B2. Model-predicted right-lateral slip patch due to coseismic slip on the Northridge fault.

fault are likely too small to have been detected by the campaign GPS data at the time. To determine if there is any seismological evidence that the San Andreas underwent triggered slip, we utilize the relocated earthquake catalog of Lin et al. (2007). The entire model-predicted triggered slip patch has a scalar moment release of 1.19×10^{18} Nm (M_W=6.02); however, if we assume that any slip below 20 km depth is aseismic, then the total scalar moment release is 3.71×10^{17} Nm (M_w=5.68). Either way, this is a non-trivial amount of moment release, which should have generated significant measured seismicity. While no moderate earthquakes of anything approaching a M_w5.7 were detected near the San Andreas during the 100 days after Northridge (i.e. the postseismic period, Savage and Svarc, 2010), it is reasonable to expect that if the San Andreas underwent triggered slip that a significant amount of

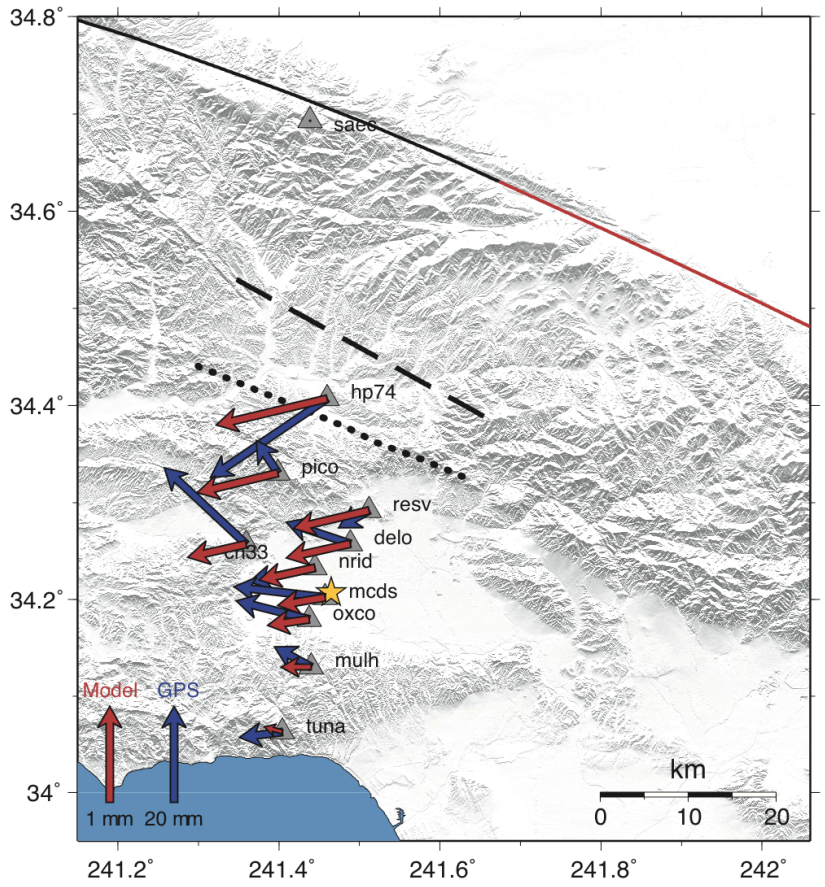

Figure B3. Comparison of the postseismic GPS motions (blue arrows) from Savage and Svarc (2010) and the surface displacements due to the mechanical model-predicted triggered slip on the San Andreas fault (red arrows). The upper tip line of the Northridge fault is shown with a dotted line and the projection of the upper tip line to the surface of the Earth is shown with a dashed line. The solid line shows the San Andreas fault trace with the zone of potential triggered slip shown in red. A gold star shows the Northridge epicenter location. Note that while the model-displacements point in similar directions to the GPS data, the two vectors are plotted scales that differ by a factor of 20.

microseismicity would have been recorded near or on the San Andreas fault. To explore this possibility, we use the relocated earthquake catalog of Lin et al. (2007) and locate events that are near the model-predicted slip patch and within the postseismic period (Figure B4). We find only two events that occurred within 20km of the potential triggered slip patch: A M_w0.96 and a M_w1.59. These two events sum

to a cumulative moment release of only M_w1.62. When compared to the M_w5.68 release of the model-predicted potential triggered slip patch, we can conclude that even if these two events arose due to triggered slip, that the amount of triggered slip would be negligible and certainly far below the geodetic detection threshold.

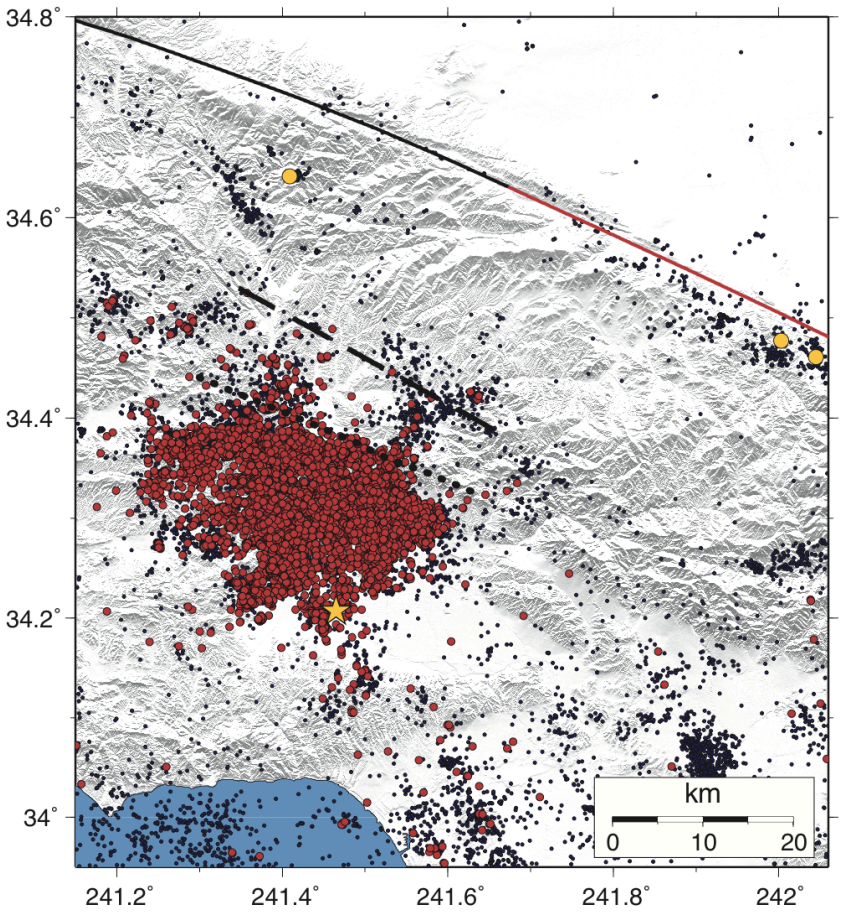

Figure B4. The entire Lin et al. (2007) relocated epicenter catalog is shown with blue dots, while earthquakes within 100 days of the Northridge earthquake are shown with red circles. From these events within 100 days of the Northridge event (the length of the postseismic period suggested by Savage and Svarc, 2010) we find only three earthquakes within 20 km of any point on the San Andreas fault in the mapped region (gold circles), and only two of these events are near the model-predicted triggered slip patch (the two gold circles near the right edge of the map). Fault traces and tip lines are the same as in Figure 2.12.

Appendix C: Education and outreach

With knowledge of how each individual fault parameter may change the surface deformation signal, it is useful to practice using this information in order to model real world solutions where all fault parameters interact and tradeoff with each other. For this purpose, I coded a program within Matlab, in which a user, with no modeling experience, may calculate a forward model the Northridge earthquake using the Okada code assuming a uniform slipping planar rectangular dislocation. This will teach the user many important aspects of earthquakes, modeling and surface deformation. First, by altering the parameters to determine a best-fitting model, the user observes what effects certain fault parameters have on surface deformation, similar to the examples above. For example, the user may observe a narrow deformation pattern with large uplift and realize that this represents large, shallow slip. The program also introduces the user to data misfits and how to reduce them. The root mean square (RMS) of the data and the residual RMS are both shown in the program. It is explained that a better fitting model will reduce the residual RMS. Furthermore, this exercise gives an introduction as how much moment is required to change the magnitude of an earthquake, which can be accomplished by adding more slip or area to the fault plane.

The data used to determine the model in this program are the same ERS-1 data points used in modeling the Northridge earthquake (Figure 2.5). Only the ERS-1

data points are used as they represent the highest quality data in the Northridge study. In addition, the use of a single dataset makes the program simpler for the user as there will be no disagreements between datasets. This modeling program is intended for the use of teaching the interaction between surface and subsurface processes and may prove useful in a classroom where geophysics and tectonics are studied. A screen shot of the user interface is shown in Figure C1.

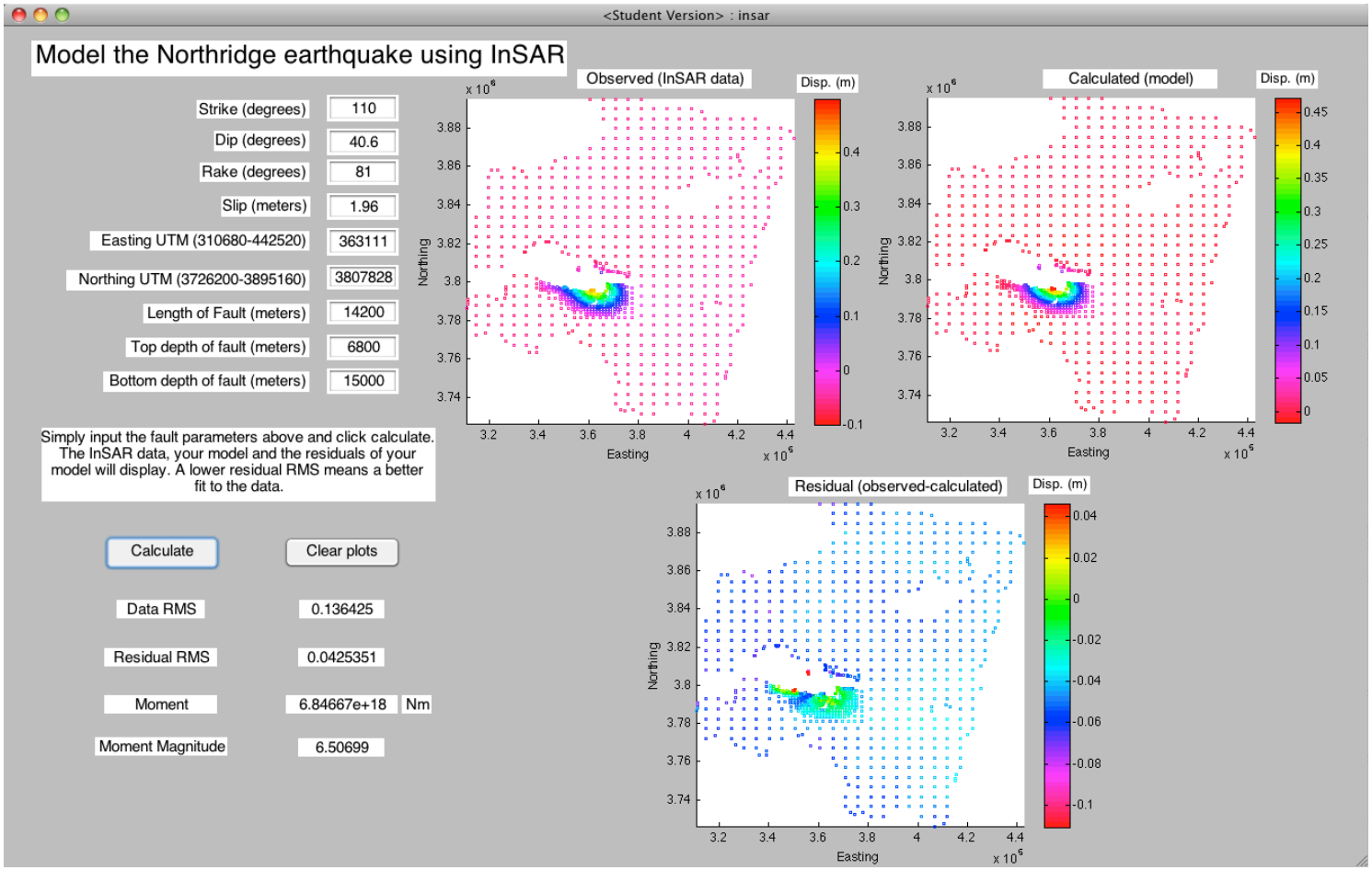

Figure C1 InSAR modeling program. Users input the fault geometry in the boxes near the parameters, click the calculate, button. A visual output of data, model and residual plots is shown, as well as the residual RMS, seismic moment and moment magnitude are displayed